



저작자표시-비영리-변경금지 2.0 대한민국

이용자는 아래의 조건을 따르는 경우에 한하여 자유롭게

- 이 저작물을 복제, 배포, 전송, 전시, 공연 및 방송할 수 있습니다.

다음과 같은 조건을 따라야 합니다:



저작자표시. 귀하는 원저작자를 표시하여야 합니다.



비영리. 귀하는 이 저작물을 영리 목적으로 이용할 수 없습니다.



변경금지. 귀하는 이 저작물을 개작, 변형 또는 가공할 수 없습니다.

- 귀하는, 이 저작물의 재이용이나 배포의 경우, 이 저작물에 적용된 이용허락조건을 명확하게 나타내어야 합니다.
- 저작권자로부터 별도의 허가를 받으면 이러한 조건들은 적용되지 않습니다.

저작권법에 따른 이용자의 권리는 위의 내용에 의하여 영향을 받지 않습니다.

이것은 [이용허락규약\(Legal Code\)](#)을 이해하기 쉽게 요약한 것입니다.

[Disclaimer](#)

공학박사학위논문

**Improvement of Thermal-Hydraulic System  
Code for Multidimensional Mixing Behavior  
in a Downcomer Annulus**

환형 강수부 내에서의 다차원적 혼합 거동 예측을  
위한 열수력 계통코드 개선 연구

2017 년 2 월

서울대학교 대학원  
에너지시스템공학부  
이 거 형

# Improvement of Thermal-Hydraulic System Code for Multidimensional Mixing Behavior in a Downcomer Annulus

환형 강수부 내에서의 다차원적 혼합 거동 예측을 위한  
열수력 계통코드 개선 연구

지도교수 박 군 철

이 논문을 공학박사 학위논문으로 제출함  
2016 년 10 월

서울대학교 대학원  
에너지시스템공학부  
이 거 형

이거형의 박사학위논문을 인준함  
2016 년 12 월

위 원 장	<u>김 응 수</u> (인)
부위원장	<u>박 군 철</u> (인)
위 원	<u>조 형 규</u> (인)
위 원	<u>방 영 석</u> (인)
위 원	<u>어 동 진</u> (인)

# **Abstract**

## **Improvement of Thermal-Hydraulic System Code for Multidimensional Mixing Behavior in a Downcomer Annulus**

Keohyoung Lee

Department of Energy System Engineering

The Graduate School

Seoul National University

The APR1400 (Advanced Power Reactor of 1400 MWe) adopts a DVI (Direct Vessel Injection) system that injects SI (Safety Injection) water directly into the reactor vessel downcomer during accidents. Since the DVI nozzles are directly attached to the reactor vessel downcomer, complex thermal-hydraulic phenomena are expected to occur in the downcomer region. KAERI (Korea Atomic Energy Research Institute) has carried out experiments by utilizing ATLAS (Advanced Thermal-hydraulic Test Loop for Accident Simulation), an integral test facility, for the APR1400. Among the experiments, a 50% DVI line break accident was selected for ISP (International Standard Problem) No. 50 exercise. In this exercise, multidimensional phenomena such as ECC (Emergency Core Cooling) water mixing in the upper downcomer observed were highlighted in terms of the capability of system codes. It was found that the codes' prediction capability of three-dimensional downcomer mixing phenomena was not satisfactory in most

calculations. The cold ECC water was well mixed with the hot inventory according to the test result. However, this vigorous mixing was not predicted appropriately by the system codes. In most calculations, the fluid temperature of the intact loop side annulus was much lower than that of the broken side annulus with the azimuthal temperature stratification in the downcomer region.

Since the difference of aspect ratios between the prototype and the test facilities can influence the mixing behavior in the downcomer, an experimental study was performed with an integral effect test facility, SNUF (Seoul National University Facility), to observe the mixing behavior in the downcomer which has a similar aspect ratio with the prototype. The length to diameter scaling ratio of SNUF is approximately 2.0 while that of ATLAS is 6.0. According to the results of SNUF test, the ECC water was mixed well in the downcomer annulus. However, the azimuthal temperature stratification in the downcomer was predicted by a best-estimated system code, MARS (Multi-dimensional Analysis Reactor Safety). It means that the analysis results for the prototype, APR1400, can be inaccurate in terms of describing the mixing phenomena in the downcomer.

The cause of the limitation to predict the mixing behavior was investigated. In MARS, the momentum flux terms are set to zero for the junction between the one-dimensional volume and the three-dimensional cell of MultiD component because the axial and radial velocities are small in the large three-dimensional region. However, if the nozzles are attached to the downcomer, which has a thin gap size, the axial and radial velocities are not small when the incoming orthogonal flow through the nozzles impinges against the downcomer wall. It was necessary to consider the momentum flux terms induced by the impinging flow, so that an appropriate jet impingement model to apply for the system code, MARS, was

developed in this study.

To develop the jet impingement model, CFD (Computational Fluid Dynamics) calculations were carried out, and the jet impingement model was formulated based on the CFD calculations with various conditions. The momentum flux term by the jet impingement phenomena was correlated with the diameter of the nozzle, the gap size of the downcomer, and the velocity of the incoming flow. This model was applied to MARS by considering the momentum flux term for the junctions connected to the three-dimensional cell. The modified MARS with the jet impingement model was validated with the test results from SNUF, ATLAS, and ROCOM (Rossendorf Coolant Mixing), and the analysis results showed good agreements with each test data.

For plant application, the ECC mixing behavior in the downcomer during the DVI line break accident in the APR1400 was estimated by utilizing MARS. It was found that more vigorous mixing in the downcomer was predicted by the modified MARS code, and the boron bypass ratio through the broken DVI nozzle estimated by the modified MARS code was larger than that estimated by the original MARS code. And the SLB (Steam Line Break) accident in the APR1400 was analyzed with MARS. The reactivity due to the negative MTC (Moderator Temperature Coefficient) was estimated according to the local fluid temperature in the core to identify the mixing effect of the jet impingement model during the SLB accident. According to the analysis results, the reactivity difference was around  $0.2 \sim 0.4\% \Delta\rho$  between the original MARS and modified MARS. When considering the safety margin of the APR1400 for the SLB accident is around  $0.2\% \Delta\rho$ , MARS adopting incorporation of the jet impingement model can influence the safety analysis outcome meaningfully.

**Keywords**

**multidimensional mixing, downcomer annulus, jet impingement model, MultiD, DVI line break, steam line break, SNUF, ATLAS, ROCOM, MARS, momentum flux term**

**Student Number: 2008-30276**

# List of Contents

<b>Abstract.....</b>	<b>i</b>
<b>List of Contents .....</b>	<b>v</b>
<b>List of Tables.....</b>	<b>vii</b>
<b>List of Figures.....</b>	<b>viii</b>
<b>Chapter 1 Introduction.....</b>	<b>1</b>
1.1 Background and Motivation.....	1
1.2 Objective and Scope.....	5
<b>Chapter 2 Integral Effect Test for Mixing Behavior in Downcomer.....</b>	<b>17</b>
2.1 Experimental Apparatus .....	17
2.1.1 Description of the Test Facility .....	17
2.1.2 Instrumentation System of the Test Facility .....	19
2.2 Scaling Analysis of SNUF .....	20
2.2.1 Scaling Methodology.....	20
2.2.2 Determination of the Test Conditions.....	23
2.3 Experimental Results .....	27
2.3.1 System Pressure.....	27
2.3.2 Break Flow .....	28
2.3.3 Collapsed Water Level in the Core and Downcomer .....	29
2.3.4 Fluid Temperature.....	31
2.4 Analytical Study .....	32
2.4.1 Characteristic of MARS .....	33
2.4.2 SNUF Modeling for the Code Assessment.....	35
2.4.3 Analysis Results of SNUF Test by MARS .....	36
<b>Chapter 3 Improvement of Thermal-Hydraulic System Code .....</b>	<b>75</b>
3.1 Investigation of Azimuthal Temperature Stratification.....	75
3.1.1 Jet Impingement Phenomenon onto a Wall .....	75

3.1.2 Momentum Flux Terms for One-Dimensional Connections .....	78
3.2 Development of Jet Impingement Model.....	80
3.2.1 CFD Model Validation with Available Experimental Data .....	81
3.2.2 Modeling of the Jet Impingement.....	85
3.3 Validation of Jet Impingement Model.....	94
3.3.1 Validation with SNUF Test.....	95
3.3.2 Validation with the ATLAS Test.....	96
3.3.3 Validation with the ROCOM Test.....	98
<b>Chapter 4 Plant Applications of Jet Impingement Model.....</b>	<b>141</b>
4.1 APR1400 DVI Line Break Accident .....	141
4.1.1 Simulation Model and Conditions.....	141
4.1.2 Analysis Results and Insight.....	142
4.2 APR1400 Steam Line Break Accident .....	144
4.2.1 Description of the Steam Line Break Accident .....	144
4.2.2 Simulation Model and Conditions.....	145
4.2.3 Analysis Results and Insight.....	146
<b>Chapter 5 Conclusions.....</b>	<b>164</b>
5.1 Summary .....	164
5.2 Recommendations .....	166
<b>Nomenclature .....</b>	<b>169</b>
<b>References.....</b>	<b>172</b>
<b>Appendix A. Modification of MARS Code.....</b>	<b>180</b>
<b>국문 초록.....</b>	<b>184</b>

# List of Tables

Table 1.1 Major conditions regarding the mixing in the downcomer.....	11
Table 2.1 Major information of the discharge storage tank .....	39
Table 2.2 Major information of the broken DVI nozzle .....	40
Table 2.3 Major information of the heat removal system.....	41
Table 2.4 Major design characteristics of SNUF compared to the prototype.....	42
Table 2.5 Major scaling ratio of SNUF.....	43
Table 2.6 Initial conditions of the ATLAS test (OECD/NEA, 2012).....	44
Table 2.7 Sequence of events for the ATLAS test (OECD/NEA, 2012) .....	45
Table 2.8 Target and measured test conditions of SNUF .....	46
Table 3.1 Comparison of Froude number between Eqs. (1.1) and (3.12) for the ROCOM buoyance mixing tests .....	102
Table 3.2 Initial conditions of the ROCOM test 2.2 (Kurki, 2015).....	103
Table 4.1 The sequences of trips in the APR1400 during the DVI line break accident .....	149
Table 4.2 The comparison of the reactivity due to the negative MTC during the SLB accident between the original and modified MARS analysis.....	150
Table A.1 The source code to apply the jet impingement model.....	181

# List of Figures

Figure 1.1 Fluid temperature measurement locations in the downcomer of the ATLAS (OECD/NEA, 2012) .....	12
Figure 1.2 Azimuthal distribution of the downcomer fluid temperature of the test (OECD/NEA, 2012).....	13
Figure 1.3 Azimuthal distribution of the downcomer fluid temperature of the NRC's calculation (OECD/NEA, 2012) .....	14
Figure 1.4 Core radial power distribution for the SLB analysis (Kucukboyaci et al., 2015).....	15
Figure 1.5 Research outline .....	16
Figure 2.1 Schematic diagram of SNUF .....	47
Figure 2.2 Heaters and instrumentation in the core of SNUF .....	48
Figure 2.3 Plan view of SNUF.....	49
Figure 2.4 Cross-sectional view of SNUF .....	50
Figure 2.5 Schematic diagram of the discharge storage tank .....	51
Figure 2.6 Design drawing of the discharge storage tank (plan view) .....	52
Figure 2.7 Design drawing of the discharge storage tank (cross-sectional view) ..	53
Figure 2.8 Design drawing of the discharge storage tank (location of the spray nozzle).....	54
Figure 2.9 Schematic diagram of the broken DVI nozzle .....	55
Figure 2.10 Schematic diagram of the heat removal system .....	56
Figure 2.11 Design drawing of the heat removal system.....	57
Figure 2.12 Instrumentation system of SNUF .....	58
Figure 2.13 Fluid temperature measurement locations in the downcomer of SNUF .....	59
Figure 2.14 Visualization windows of SNUF .....	60
Figure 2.15 SI flow rate from the SITs in the ATLAS test (OECD/NEA, 2012) ..	61
Figure 2.16 Comparison of the thermal power between SNUF and ATLAS tests	61
Figure 2.17 Comparison of the system pressure between SNUF and ATLAS tests in the normalized scale .....	62
Figure 2.18 Steam dome temperature (steam) of SNUF test.....	62

Figure 2.19 Comparison of the accumulated break flow between SNUF and ATLAS tests in the normalized scale .....	63
Figure 2.20 Comparison of the break flow rate between SNUF and ATLAS tests in the normalized scale.....	63
Figure 2.21 Comparison of the downcomer collapsed water level between SNUF and ATLAS tests in the normalized scale .....	64
Figure 2.22 Comparison of the core collapsed water level between SNUF and ATLAS tests in the normalized scale.....	64
Figure 2.23 Loop fluid temperature of SNUF test.....	65
Figure 2.24 Loop fluid temperate of the ATLAS test (OECD/NEA, 2012) .....	65
Figure 2.25 Upper downcomer fluid temperature of SNUF test .....	66
Figure 2.26 Lower downcomer fluid temperature of SNUF test.....	66
Figure 2.27 Comparison of the SI flow rate between SNUF test ATLAS tests in the normalized scale.....	67
Figure 2.28 Momentum control volume for flow in the x direction in the x-y plane of the MultiD component in MARS (KAERI, 2009) .....	68
Figure 2.29 Schematic nodalization of the MARS model for SNUF .....	69
Figure 2.30 Comparison of the system pressure between SNUF test and MARS analysis.....	70
Figure 2.31 Comparison of the hot leg fluid temperature between SNUF test and MARS analysis .....	70
Figure 2.32 Comparison of the cold leg fluid temperature between SNUF test and MARS analysis .....	71
Figure 2.33 Comparison of the SI flow rate between SNUF test and MARS analysis.....	71
Figure 2.34 Comparison of the break flow rate between SNUF test and MARS analysis.....	72
Figure 2.35 Comparison of the accumulated break flow between SNUF test and MARS analysis .....	72
Figure 2.36 Comparison of the downcomer collapsed water level between SNUF test the MARS analysis.....	73
Figure 2.37 Comparison of core collapsed water level between SNUF test and MARS analysis .....	73
Figure 2.38 Comparison of the upper downcomer fluid temperature between SNUF test and the MARS analysis.....	74

Figure 3.1 Geometry of the flow from a jet impinging normal to a wall (Beltaos & Rajaratnam, 1974).....	104
Figure 3.2 Comparison of analytical prediction for the free surface velocity with measurements (Stevens & Webb, 1992) .....	105
Figure 3.3 Example of the inlet nozzle and downcomer nodalization with the features of one-dimensional and three-dimensional .....	106
Figure 3.4 Structured hexagonal grids of the jet impingement phenomena validation model .....	107
Figure 3.5 Flow domain boundaries for the jet impingement phenomena validation model .....	108
Figure 3.6 Profiles of the velocity magnitude normalized by the incoming velocity at a various radial location (Behnia et al., 1998; Cooper et al., 1993).....	109
Figure 3.7 Profiles of the velocity magnitude normalized by the incoming velocity at $r/d=1.0$ (Zuckerman & Lior, 2007; Cooper et al., 1993) .....	110
Figure 3.8 Profiles of the velocity magnitude normalized by the incoming velocity at $r/d=2.5$ (Zuckerman & Lior, 2007; Cooper et al., 1993) .....	111
Figure 3.9 Profiles of the velocity magnitude normalized by the incoming velocity at $r/d=2.5$ by using the jet impingement phenomena validation model (Cooper et al., 1993) .....	112
Figure 3.10 Schematic diagram of the parameters for the jet impingement model .....	112
Figure 3.11 Example of the profile of the velocity magnitude ( $V=0.5$ m/s, $d=0.05$ m, $t = 0.025$ m, $r = 0.01$ m).....	113
Figure 3.12 Results of the sensitivity calculation with various inlet nozzle diameters (non-dimensional thickness) .....	113
Figure 3.13 Results of the sensitivity calculation with various nozzle to wall spacing (non-dimensional thickness).....	114
Figure 3.14 Results of the sensitivity calculation with various nozzle to wall spacing (momentum boundary layer thickness) .....	114
Figure 3.15 Results of the sensitivity calculation with various nozzle inlet velocity (non-dimensional thickness) .....	115
Figure 3.16 Results of the sensitivity calculation with various fluid properties (non-dimensional thickness) .....	115
Figure 3.17 Comparison of the correlation with the computed results.....	116
Figure 3.18 Results of the calculation to confirm the scale-up capability of the correlation equation .....	116

Figure 3.19 Comparison of the correlation with the computed results on the prototype scale .....	117
Figure 3.20 Test matrix of ECC injection experiments, classification of the ROCOM tests, isolines of Froude numbers (Höhne & Kliem, 2007).....	118
Figure 3.21 Positions of wire mesh downcomer sensors in the ROCOM (Rohde et al., 2005) .....	119
Figure 3.22 Test matrix of ECC injection experiments, visualization of the time-dependent tracer distribution at the sensors in the downcomer, isolines of Froude numbers (Höhne et al., 2006).....	120
Figure 3.23 Mixing scalar evolution in the downcomer in ROCOM buoyance driven mixing tests (Höhne & Kliem, 2007; Rohde et al., 2005).....	121
Figure 3.24 Comparison of the upper downcomer fluid temperature between the original and modified MARS analysis for SNUF.....	122
Figure 3.25 Comparison of the primary system pressure between the original and modified MARS analysis for SNUF .....	122
Figure 3.26 Comparison of the break flow rate between the original and modified MARS analysis for SNUF .....	123
Figure 3.27 Comparison of the core collapsed water level between the original and modified MARS analysis for SNUF .....	123
Figure 3.28 Comparison of the downcomer collapsed water level between the original and modified MARS analysis for SNUF.....	124
Figure 3.29 Schematic nodalization of the MARS model for the ATLAS .....	125
Figure 3.30 Downcomer fluid temperature of the original MARS analysis for the ATLAS.....	126
Figure 3.31 Downcomer fluid temperature of the modified MARS analysis for the ATLAS.....	127
Figure 3.32 Contour map of the downcomer fluid temperature of the ATLAS test (OECD/NEA, 2012).....	128
Figure 3.33 Contour map of the downcomer fluid temperature of the original MARS analysis for the ATLAS .....	129
Figure 3.34 Contour map of the downcomer fluid temperature of the modified MARS analysis for the ATLAS .....	130
Figure 3.35 Comparison of the primary system pressure between the original and modified MARS analysis for the ATLAS in the normalized scale.....	131
Figure 3.36 Comparison of the accumulated break flow between the original and modified MARS analysis for the ATLAS in the normalized scale.....	131

Figure 3.37 Comparison of the core collapsed water level between the original and modified MARS analysis for the ATLAS in the normalized scale .....	132
Figure 3.38 Comparison of the downcomer collapsed water level between the original and modified MARS analysis for the ATLAS in the normalized scale..	132
Figure 3.39 Measured loop flow rate in the ROCOM test 2.2 (Kurki, 2015).....	133
Figure 3.40 Schematic nodalization of the MARS model for the ROCOM (Lee & Chung, 2012) .....	134
Figure 3.41 Cold leg flow rate as the input for the MARS analysis.....	135
Figure 3.42 Comparison of the temperature distribution in the unwrapped downcomer at 30 seconds between the ROCOM test 2.2 and the MARS analysis (Kliem & Franz, 2012).....	136
Figure 3.43 Comparison of the temperature distribution in the unwrapped downcomer at 60 seconds between the ROCOM test 2.2 and the MARS analysis (Kliem & Franz, 2012).....	137
Figure 3.44 Comparison of the temperature distribution in the unwrapped downcomer at 90 seconds between the ROCOM test 2.2 and the MARS analysis (Kliem & Franz, 2012).....	138
Figure 3.45 Comparison of the temperature distribution in the unwrapped downcomer at 120 seconds between the ROCOM test 2.2 and the MARS analysis (Kliem & Franz, 2012).....	139
Figure 3.46 Comparison of the temperature distribution in the unwrapped downcomer at 150 seconds between the ROCOM test 2.2 and the MARS analysis (Kliem & Franz, 2012).....	140
Figure 4.1 Schematic nodalization of the MARS model for the APR1400.....	151
Figure 4.2 Pressurizer pressure during the DVI line break accident for the APR1400 (MARS analysis).....	152
Figure 4.3 Break flow rate during the DVI line break accident for the APR1400 (MARS analysis).....	152
Figure 4.4 Core collapsed water level during the DVI line break accident for the APR1400 (MARS analysis).....	153
Figure 4.5 Downcomer collapsed water level during the DVI line break accident for the APR1400 (MARS analysis) .....	153
Figure 4.6 SI flow rate from the SIP during the DVI line break accident for the APR1400 (MARS analysis).....	154

Figure 4.7 Comparison of the upper downcomer fluid temperature during the DVI line break accident between the original and modified MARS analysis .....	155
Figure 4.8 Comparison of the temperature distribution in the downcomer during the DVI line break accident at 150 seconds between the original and modified MARS analysis .....	156
Figure 4.9 Comparison of the boron bypass ratio during the DVI line break accident between the original and modified MARS analysis .....	157
Figure 4.10 Comparison of the boron concentration in the core during the DVI line break accident between the original and modified MARS analysis .....	157
Figure 4.11 Schematic nodalization of the MARS model for the APR1400 (multidimensional core, downcomer, and steam generator model) (KAERI, 2009) .....	158
Figure 4.12 Comparison of the cold leg fluid temperature during the SLB accident between the original and modified MARS analysis .....	159
Figure 4.13 Comparison of the temperature distribution in the downcomer during the SLB accident at 90 seconds between the original and modified MARS analysis .....	160
Figure 4.14 Comparison of the temperature distribution in the core during the SLB accident at 90 seconds between the original and modified MARS analysis .....	161
Figure 4.15 The moderator temperature reactivity vs. the temperature at post trip (KHNP, 2002) .....	162
Figure 4.16 Comparison of the reactivity and fluid temperature distribution at the middle elevation of the core during the SLB accident at 90 seconds between the original and modified MARS analysis.....	163
Figure A.1 Modular structures of transient calculation in MARS (KAERI, 2009) .....	182
Figure A.2 Calculation process of the momentum flux with the jet impingement model in MARS .....	183

# Chapter 1

## Introduction

### 1.1 Background and Motivation

The APR1400 (Advanced Power Reactor of 1400 MWe) is an advanced PWR (Pressurized Water Reactor), which is in operation and under construction in Korea and UAE (United Arab Emirates). This reactor adopts a DVI (Direct Vessel Injection) system that injects SI (Safety Injection) water directly into the reactor vessel downcomer, instead of using a CLI (Cold Leg Injection) system, as a new safety injection feature (KHNP, 2002); the DVI nozzles are located 2.1 m above the cold leg. This new feature of the APR1400 can eliminate complicated piping interconnections and is believed to ensure more safety injection water reaches the reactor core escaping bypass. Thus, it is expected that the improvement will greatly enhance the reliability of ECCS (Emergency Core Cooling System) of the APR1400. Due to these advantages, the DVI model has been adopted in several other advanced plants, such as the AP1000 (Advanced Passive 1000 MWe), APWR (Advanced Pressurized Water Reactor), VVER-1000 (Water-Water Energetic Reactor 1000 MWe), etc. (Choi et al., 2010) However, the DVI nozzles directly attached to the reactor vessel downcomer so that complex thermal-hydraulic phenomena are expected to occur in the downcomer region.

To assess the overall phenomena of the reactor during various accidents, KAERI (Korea Atomic Energy Research Institute) has been operating an integral effect test facility, ATLAS (Advanced Thermal-hydraulic Test Loop for Accident Simulation) for the APR1400 (Baek et al., 2005; Choi et al., 2006). In 2008, sensitivity tests for different DVI line break sizes were carried out (Choi et al., 2010; Choi et al., 2011) to generate test data which could be used for an assessment and improvement of safety analysis codes. Integral effect database for four break sizes were established: 5%, 25%, 50%, and 100%.

Among the DVI line break scenarios, 50% breakage of the cross section of a DVI nozzle would be of interest because this break size is on the edge of the criterion provided by the EPRI (Electric Power Research Institute) requirement where a core uncover should be prevented by a best estimate methodology (EPRI, 1995). Thus, this scenario was selected for OECD (Organization for Economic Cooperation and Development) / NEA (Nuclear Energy Agency) ISP (International Standard Problem) No. 50 (OECD/NEA, 2012). In the ISP-50 exercise, the predictions of a 50% DVI line break accident of the APR1400 with different best-estimate system codes were compared with each other and with the results of the experimental simulation.

According to the final integration report of the ISP-50 (OECD/NEA, 2012), multidimensional phenomena such as ECC (Emergency Core Cooling) water mixing in the upper downcomer observed in the test were highlighted in terms of describing the prediction capability. It was found that the codes' prediction capability of three-dimensional downcomer mixing phenomena was not satisfactory in most calculations. During ATLAS test, cold ECC water was introduced by a SIP (Safety Injection Pump) and three SITs (Safety Injection

Tanks) at a different time. The SIP injected ECC water into the downcomer annulus through the DVI nozzle opposite to the broken DVI nozzle and three SITs injected ECC water through the intact three DVI nozzles. At the time of SIP injection, the downcomer annulus was full of hot water, almost saturation temperature, and it was observed that the cold ECC water was well mixed with the hot inventory as shown in Figs. 1.1 and 1.2. However, this vigorous and instant mixing was not predicted appropriately by the system codes. In most calculations, the fluid temperature of the intact loop side annulus was much lower than that of the broken side annulus. That is, azimuthal temperature stratification was predicted even in lower downcomer region. The final integration report of the ISP-50 (OECD/NEA, 2012) concluded that this inaccurate prediction seems to be due to limitation of the one-dimensional code and suggested that the momentum flux in lateral direction needs to be improved for realistic simulation of the downcomer fluid mixing. Among the calculation results of the ISP-50 exercise, NRC (Nuclear Regulatory Commission) calculation utilizing three-dimensional modeling of the reactor pressure vessel including the downcomer with TRACE version 5.0 with patch 2 applied (U.S. NRC, 2012) showed a better predictability for the ECC mixing in the downcomer than other calculations. However, the NRC's calculation also did not predict the measured data sufficiently, especially after 100 seconds, as shown in Fig. 1.3. That is, there is limitation of the system codes to treat ECC mixing in the downcomer, even if the downcomer is modelled three-dimensionally.

This kind of multidimensional behavior in a downcomer annulus can influence the mixing of inlet coolant with the asymmetric temperature during a transient such as the SLB (Steam Line Break) accident as well as the ECC water mixing

with the DVI mode. A rupture of a steam line in one of the loops causes an increase in steam flow from the broken secondary system. The increased heat removal induces the temperature drop in the primary system for broken side loop. Then, it results in a highly asymmetric coolant temperature of each loop, and the azimuthal temperature profile in the lower downcomer can be stratified. If the coolant in the lower downcomer is not mixed, it can cause a challenging problem with a highly asymmetric power distribution in the core due to a negative MTC (Moderator Temperature Coefficient). In accordance with an analysis through researches to develop an advanced integrated modeling/simulation tool named VERA (Virtual Environment for Reactor Applications) (Montgomery, 2014) in CASL (Consortium of Advanced Simulation of Light water reactors) program, an asymmetric core inlet temperature distribution (high temperature region: 480 K / low temperature region: 458 K) during the SLB accident resulted a highly asymmetric core power distribution as illustrated in Fig. 1.4 (Kucukboyaci et al., 2015). The high power assemblies were clustered in the broken loop section of the core, and the hot assembly factor was around 7.2. Therefore, it is important to estimate the mixing effect of the coolant water in the downcomer which has the different temperatures driven from the broken and intact steam generators.

As described above, the current best-estimate system codes have a limitation to predict the multidimensional liquid phase mixing behavior in a downcomer annulus correctly, even though the mixing phenomena in the downcomer can strongly influence safety analyses. Hence, this research focused on an experimental and analytical study to explain the mixing behavior in the reactor downcomer.

## 1.2 Objective and Scope

The objective of this study was to investigate the multidimensional liquid phase mixing behavior in the downcomer annulus of the reactor. Especially, it was focused to assess the cause of the inaccurate prediction of the azimuthal temperature distribution in the downcomer by the system codes, and to improve the capability of the system code to predict the mixing behavior in the downcomer.

To achieve the objective, an experimental study was performed with an integral effect test facility, SNUF (Seoul National University Facility) (Kim et al., 2003, Kim et al., 2005, Lee et al., 2008). And the test data was predicted by utilizing a best-estimate system code, MARS (Multi-dimensional Analysis Reactor Safety)-KS 1.3 (KINS, 2016). Then, a model for the system code, named the jet impingement model, was developed by utilizing a CFD (Computational Fluid Dynamics) software, STAR-CCM+, to predict the mixing behavior in the downcomer correctly. And the tests of SNUF and ATLAS were used to validate the developed model with the modified MARS by applying the jet impingement model. An experimental data produced at ROCOM (Rossendorf Coolant Mixing) on non-uniform flow in the reactor downcomer (Kliem et al., 2008) was utilized for additional validation of the jet impingement model. And then, analytical studies were carried out to confirm the real plant applicability of the modified MARS. In these analyses, the event of the SLB as well as the DVI line break in the APR1400 was estimated. The outline of this study is described in Fig. 1.5. The research scopes are summarized as follows:

### **Experimental Study with SNUF**

In terms of describing the issue regarding the mixing behavior in the downcomer, it is important to preserve Froude numbers in accordance with the ROCOM buoyance mixing test results (Rohde et al., 2005). Rohde et al. defined the Froude number,  $Fr$ , ratio of inertial to buoyant forces in a fluid stream, as follows:

$$Fr = \frac{V}{[gs(\rho_{in} - \rho_a)/\rho_a]^{1/2}} \quad (1.1)$$

where,  $V$  is the velocity of incoming flow,  $g$  is the gravitational acceleration,  $s$  is the height of the downcomer,  $\rho_{in}$  is the density of the incoming flow, and  $\rho_a$  is the density of the ambient water in the downcomer.

In the event of a DVI line break, the primary system pressure decreases becoming nearly equivalent to the secondary system pressure. Then, it makes a plateau until the start of the loop seal clearing which introduces the vapor generated in the core to the downcomer. During the plateau of the primary system, the ECC water is injected into the downcomer through the DVI nozzle. At this time, the downcomer annulus is full of hot water, and the cold ECC water can be mixed with the hot inventory. Therefore, it is required to preserve the Froude number during the plateau of the primary system to investigate the liquid phase mixing behavior in the downcomer annulus experimentally.

As listed and calculated in Table 1.1, the Froude number of the prototype, APR1400, is 0.18 during the plateau of the primary system pressure before the loop seal clearing. On the other hand, the Froude number of the ATLAS is 0.25. It means that the mixing due to the inertial force in the downcomer of the ATLAS is more vigorous than that of the prototype. In addition, the difference of aspect

ratios between the prototype and the ATLAS can influence the mixing behavior in the downcomer. For ATLAS case, length to diameter scaling ratio ( $l_{0R}/d_{0R}$ ) is 6.0. Thus, it is possible that the vigorous mixing behavior in the downcomer of the ATLAS during the DVI line break accident is not presented in the downcomer annulus of the prototype. Therefore, it is required to carry out additional experimental studies with a test facility which has a similar aspect ratio with the prototype to explain the mixing behavior in the downcomer annulus correctly.

The SNUF is a small-scale integral loop test facility for the APR1400, which has been utilized for various studies (Kim et al., 2003, Kim et al., 2005, Lee et al., 2008). Even though, this facility is a RHRP (Reduced-Height and Reduced-Pressure) facility, it has a more similar aspect ratio with the prototype compared to the ATLAS. The length to diameter scaling ratio ( $l_{0R}/d_{0R}$ ) of SNUF is approximately 2.0. And the Froude number of SNUF before the loop seal clearing is 0.16, and this value is similar with the Froude number of the prototype compared to the ATLAS as presented in Table 1.1. Thus, an experimental study was performed with SNUF to investigate the liquid phase mixing behavior in the downcomer region of the prototype.

### **Development and Validation of the Jet Impingement Model**

As described in Section 1.1, it was found that the calculation utilizing three-dimensional modeling of the downcomer shows a better predictability for the ECC mixing in the downcomer in the ISP-50. However, this kind of three-dimensional model has also a limitation to predict vigorous mixing behaviors in the reactor downcomer.

The MARS also has the capability to model the downcomer three-

dimensionally with a component, named MultiD (KINS, 2016). The MultiD component in MARS has been developed to achieve the flexible three-dimensional capabilities in the system code and to allow the user to model more accurately the multi-dimensional hydrodynamic features of reactor applications. In the case for one-dimensional component connections to three-dimensional components such as the DVI nozzles, or cold leg nozzles attached to the reactor vessel downcomer, the junction between the one-dimensional volume and three-dimensional cell is treated like a one-dimensional junction. And all the appropriate terms such as loss and gravity are considered with the momentum equations. However, the momentum flux term are set to zero because the axial and radial velocities are small in the large three-dimensional region like crossflow junction.

If the nozzles are connected to the cylindrical core vessel which uses several rings, the momentum flux terms of the axial and radial direction can be ignored. However, if the nozzles are attached to the downcomer, which has relatively a thin gap size, the axial and radial velocities are not small when the incoming orthogonal flow through the nozzles impinges against the downcomer wall. Therefore, it is required to consider the momentum flux terms induced by the impinging flow. Thus, an appropriate jet impingement model to apply to the system code, MARS, should be developed.

To develop the jet impingement model, a CFD software, STAR-CCM+, was utilized in this study. And the V2F turbulence model (Durbin, 1995) which is widely known for well prediction of the jet impingement behavior was applied (Behnia et al., 1998; Zuckerman & Lior, 2005). The jet impingement model, formulated based on the CFD calculations with various conditions such as the diameter of the nozzle, the gap size of the downcomer, the velocity of the

incoming flow, and the properties of the working fluid, was applied to MARS.

The modified MARS with the jet impingement model was validated with the test results from SNUF and ATLAS. These validation works sought to confirm the predictive capability of the multidimensional mixing between the hot water in the downcomer and the cold ECC water through the DVI nozzle. Since the jet impingement model could be applied to the inlet coolant with the asymmetric temperature during a transient state such as the SLB accident, the test data of the ROCOM was also used to validate the modified MARS and the jet impingement model.

### **Plant Applications**

In this study, the jet impingement model was developed to predict the multidimensional mixing behavior in the downcomer, and the modified MARS with the jet impingement model was validated with the test data produced by the SNFU, ATLAS, and ROCOM. Since these test facilities are scaled-down, it is required to confirm the influence of the jet impingement model at the prototype.

At first, the ECC mixing behavior in the downcomer during the DVI line break accident in the APR1400 was estimated by utilizing MARS. In this analytical study, the influence of the jet impingement model was identified by comparing the temperature distribution in the downcomer between the results of the original MARS and modified MARS. And the SLB accident that assumed a break at the upstream of MSIV (Main Steam Isolation Valve) in the APR1400 was analyzed with the original and modified MARS code. Since the coolant temperature distributions of not only the downcomer region but also the core region are important in this assessment, a multidimensional core, downcomer, and

lower plenum modeling which was applied to MARS assessment for non-LOCA (Loss of Coolant Accident) analysis (KAERI, 2009) was utilized. And the reactivity due to the negative MTC was estimated according to the local fluid temperature in the core to identify the mixing effect of the jet impingement model during the SLB accident.

Chapter 2 presents the experimental study with SNUF to investigate the liquid phase mixing behavior in the downcomer. In this chapter, the analysis results with MARS in respect of SNUF test are presented. The jet impingement model based on the CFD calculation and the validation results of the model with various test data are covered in Chapter 3. And the plant application results of the jet impingement model are described in Chapter 4.

Table 1.1 Major conditions regarding the mixing in the downcomer

<b>Parameter</b>	<b>APR1400</b>	<b>ATLAS</b>	<b>SNUF</b>
Velocity of the ECC flow, m/s ( $V$ )	1.0 <sup>1)</sup>	1.0	$1.0 \times l_{0R}$ = 0.156 <sup>2)</sup>
System pressure <sup>3)</sup> , bar	78.3	78.3	3.13
Temperature of the ambient water <sup>3)</sup> , K	565.2	565.2	406.7
Density of the ambient water <sup>3)</sup> , kg/m <sup>3</sup> ( $\rho_a$ )	728.3	728.3	931.8
Height of the downcomer, m ( $s$ )	around 9.0	9.0 $\times l_{0R}$ = 4.5 <sup>4)</sup>	9.0 $\times l_{0R}$ = 1.4 <sup>2)</sup>
Density of the ECC water, kg/m <sup>3</sup> ( $\rho_{in}$ )	991.3	991.3	998.8
Froude number ( $Fr$ )	0.18	0.25	0.16

Note 1) assumed value

Note 2) scaling ratios of the SNUF;  $l_{0R} = 1/6.4$

Note 3) conditions during plateau of primary system pressure before loop seal clearing

Note 4) scaling ratios of the ATLAS;  $l_{0R} = 1/2$

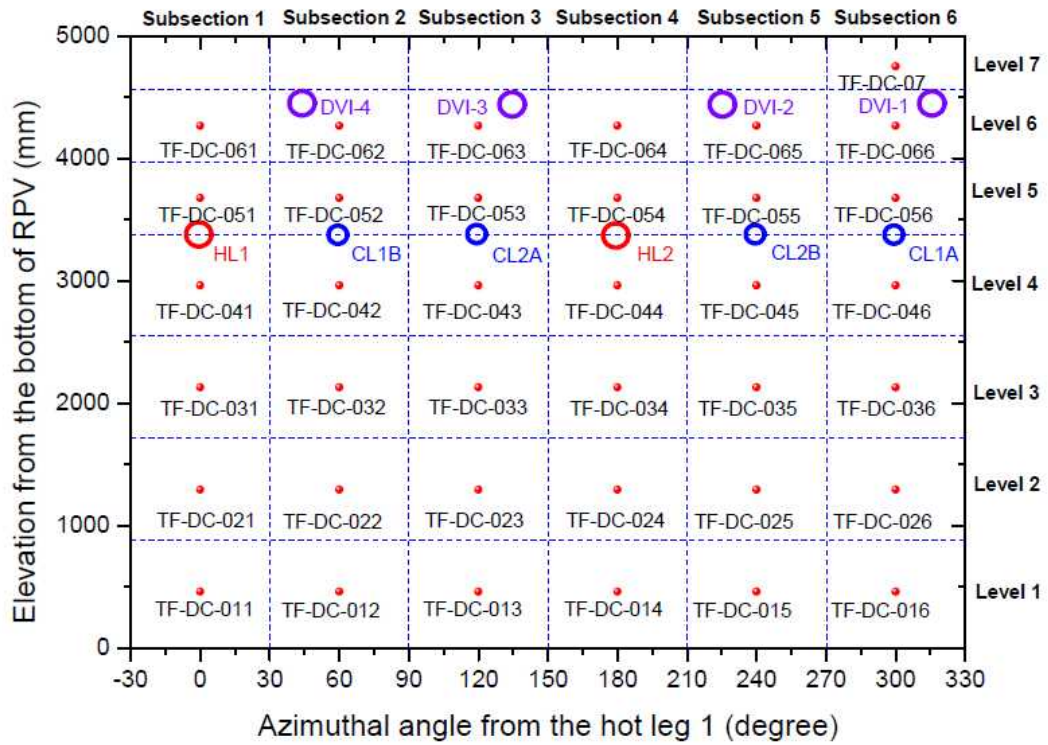


Figure 1.1 Fluid temperature measurement locations in the downcomer of the ATLAS (OECD/NEA, 2012)

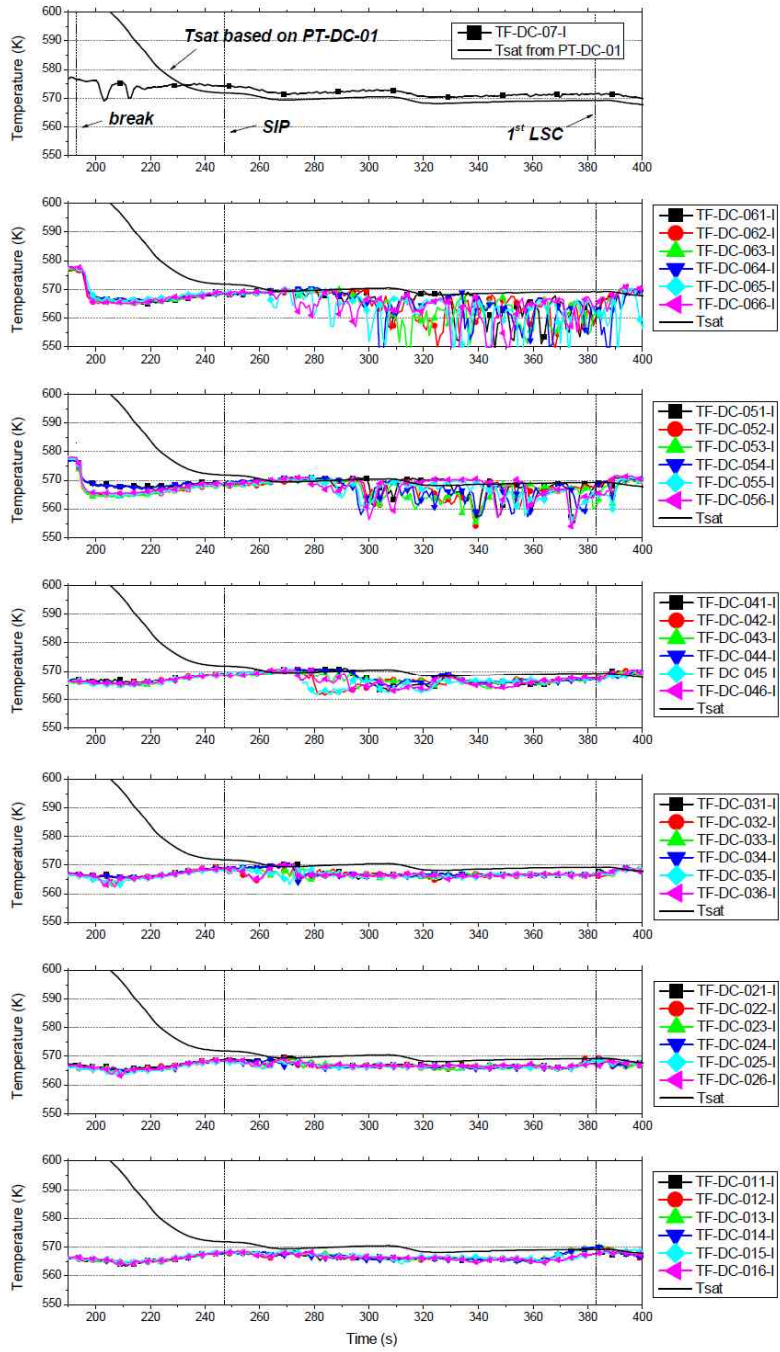


Figure 1.2 Azimuthal distribution of the downcomer fluid temperature of the test (OECD/NEA, 2012)

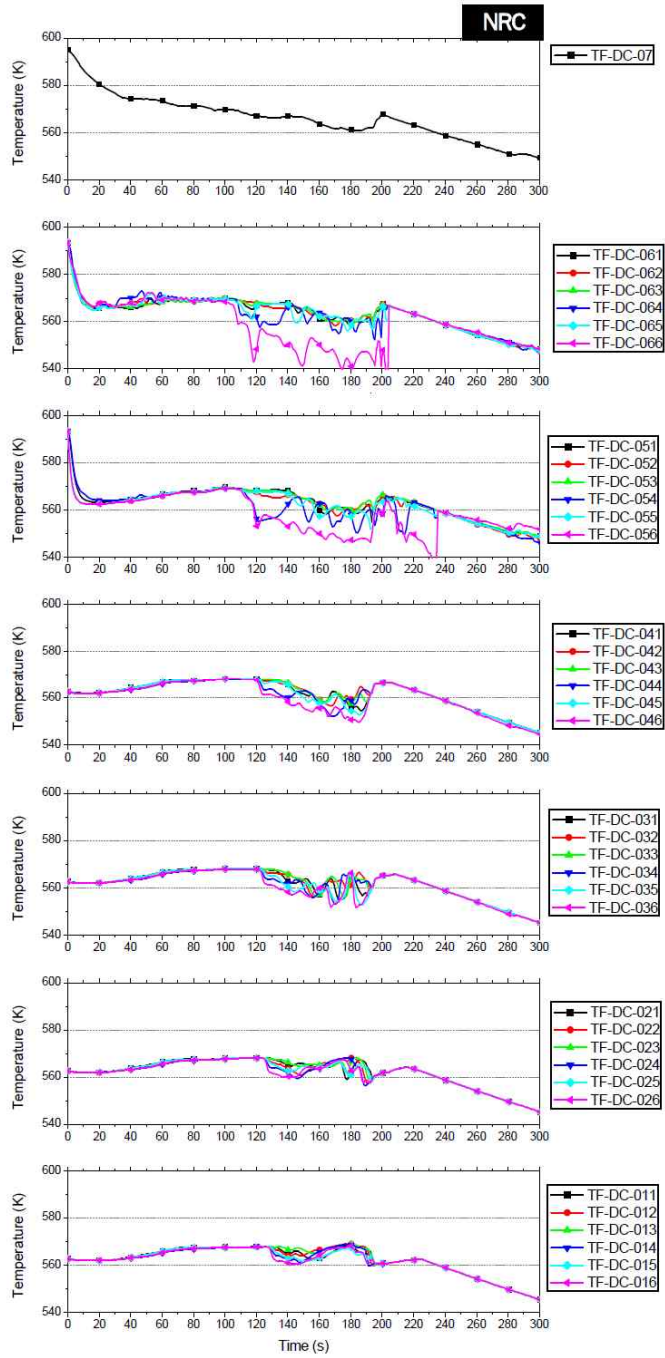


Figure 1.3 Azimuthal distribution of the downcomer fluid temperature of the NRC's calculation (OECD/NEA, 2012)



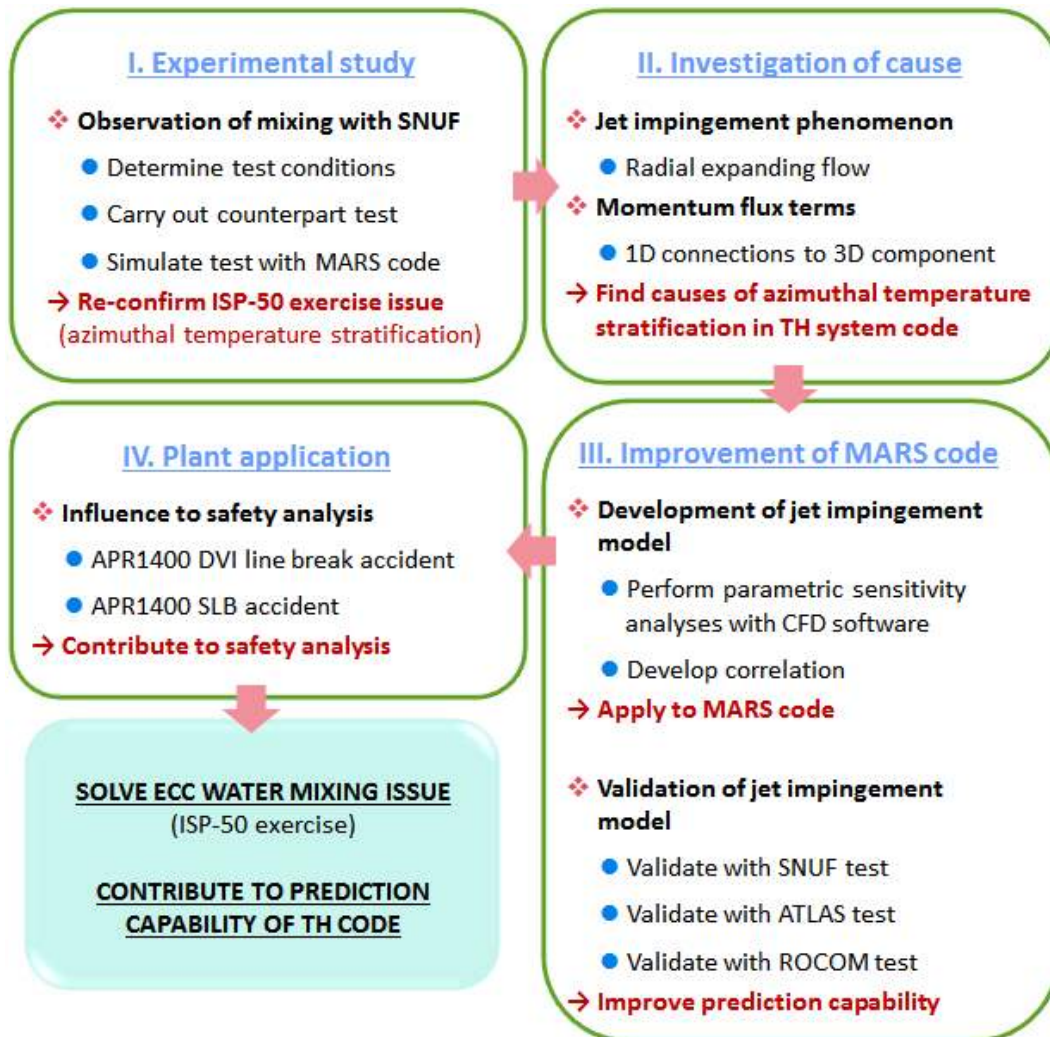


Figure 1.5 Research outline

## **Chapter 2**

# **Integral Effect Test for Mixing Behavior in Downcomer**

### **2.1 Experimental Apparatus**

In terms of describing the issue regarding the ECC mixing behavior in the downcomer, it is important to preserve Froude numbers, ratio of inertial to buoyant forces in a fluid stream, as defined in Eq. (1.1). Table 1.1 shows that the Froude number of the ATLAS is 0.25, even if the Froude number of the prototype, APR1400, is 0.18. Since it can influence to the mixing behavior in the downcomer, an additional experiment with SNUF, which has similar value, 0.16, compared to the prototype, was carried out to investigate the liquid phase mixing behavior in the downcomer region during the DVI line break accident.

#### **2.1.1 Description of the Test Facility**

The SNUF is an integral loop test facility designed to simulate the APR1400 (Kim et al., 2003; Kim et al., 2005; Lee et al., 2008). A schematic of SNUF is shown in Fig. 2.1. The scaling factors of length and area in the primary system are

1/6.4 and 1/178, respectively. The geometrical configuration of the reactor vessel in SNUF is equivalent to that in APR1400, which consists of two hot legs and four cold legs. The test vessel contains 150 heaters to simulate the core decay heat as illustrated in Fig. 2.2. The maximum total operational power of these heaters is around 180 kW. The maximum operation pressure is 0.8 MPa.

The three intact DVI lines can supply the SI water into the upper downcomer as shown in Figs. 2.3 and 2.4. The one broken DVI line is connected to the discharge storage tank. A spray device is installed in a dome of the discharge storage tank to condense the two-phase fluid discharged from the broken DVI nozzle as illustrated in Figs. 2.5, 2.6, 2.7, and 2.8, and the accumulated water mass is measured by the water level of the discharge storage tank. The major design information of the discharge storage tank is listed in Table 2.1. And the various sizes of the broken DVI nozzle are simulated by an orifice with a different inner diameter as illustrated in Fig. 2.9. And major information of the broken DVI nozzle is listed in Table 2.2.

The steam generator for each loop contains sixteen (16) U-tubes. Since the phenomenon in the primary system is more important than the secondary system in this research, the steam generator was used only for heat removal purpose. The secondary side of the steam generators is connected to the heat removal system as shown in Figs. 2.10 and 2.11. This system is installed to maintain the steady-state condition before the transient tests. The fluid in the upper part of the steam generators is transferred to the heat removal system and the feedwater cooled-down by the chillers is supplied to the lower part of the steam generators. The heat removal rate from the secondary side is controlled by adjusting the position of the valve in the feedwater supply line and changing the cooling capacity of the

chillers. Major design information of the heat removal system is listed in Table 2.3.

Major design parameters of SNUF are listed in Table 2.4, compared with those of the APR1400.

### **2.1.2 Instrumentation System of the Test Facility**

In the instrumentation system illustrated in Fig. 2.12, the DP (Differential Pressure) transmitters manufactured by Rosemount Co. (3EA) were used to measure the collapsed water level in the core and downcomer. Also, the water level of the discharge storage tank was measured by same DP transmitter (1EA). The accuracy of these DP transmitters is  $\pm 0.1\%$ . The upper plenum pressure and the discharge storage tank pressure were measured with VPRNP-A3 pressure transmitters manufactured by VALCOM Co. (3EA). These pressure transmitters have  $\pm 1.0\%$  accuracy. The temperature of the coolant was measured using K-type thermocouples (42 EA) in the upper plenum, downcomer, cold leg, hot leg, steam generator primary exit, and steam generator secondary side. An unfolded downcomer map to show two (2) azimuthal sections (intact and broken) and four (4) axial levels can be found in Fig. 2.13. And the temperatures of the safety injection tank and the discharge storage tank were also measured by K-type thermocouples (4EA). The accuracy of these thermocouples to measure the temperature is  $\pm 0.75\%$ . The SI flow rate was measured by a flowmeter manufactured by OVAL Co. (1EA), and the accuracy of this flowmeter is  $\pm 1.0\%$ . In addition, there are four visual windows between the cold leg and DVI line as shown in Figs. 2.4 and 2.14. Also, the hot legs and loop seals are visualized with Pyrex. During the test, photographs and videos were recorded from the visual

windows and Pyrex.

## 2.2 Scaling Analysis of SNUF

### 2.2.1 Scaling Methodology

Considering that SNUF is a RHRP facility, an appropriate scaling methodology should be applied in order to simulate the accident scenario. Thus, a scaling methodology to apply the RHRP facility such as SNUF, named energy scaling methodology (Lee, 2008; Bae et al., 2008), was adopted. It has advantage in determining a simple scaling factor with respect to the mass and enthalpy of the coolant.

The basic concept of the energy scaling methodology is that the system energy including the thermal power in core is scaled down with the ratio of the initial coolant mass and enthalpy. The scaling factors were obtained by simple governing equations. To obtain the scaling parameters for the coolant inventory, the governing equation was formulated with respect to the total mass of the primary system,  $M$ , which is defined as;

$$M \equiv \int \rho dV \quad (2.1)$$

where  $\rho$  is the local density and  $dV$  is the control volume in the primary system. Then, the conservation equation for the coolant mass during a transient is

composed of the inlet mass flow ( $\dot{m}_{in}$ ) and outlet mass flow ( $\dot{m}_{out}$ ) in the system.

$$\frac{dM}{dt} = \dot{m}_{in} - \dot{m}_{out} \quad (2.2)$$

In the DVI line break accident, the safety injection from the intact DVI line is the inlet and discharged flow through the broken DVI line is the outlet flow.

From the view point of the thermal power, the energy balance in the primary system was formulated with respect to a mean enthalpy in the system ( $\bar{h}$ ) as the following;

$$\frac{dM\bar{h}}{dt} = Q_c + \dot{m}_{in} h_{in} - \dot{m}_{out} h_{out} \quad (2.3)$$

$$\bar{h} \equiv \frac{\int \rho h dV}{\int \rho dV} = \frac{1}{M} \int \rho h dV \quad (2.4)$$

where  $Q_c$  is the thermal core power,  $h_{in}$  is the inlet fluid enthalpy,  $h_{out}$  is the outlet fluid enthalpy, and  $h$  is the local enthalpy in the system.

The initial mass inventory ( $M_0$ ), the initial enthalpy difference between the cold leg and hot leg ( $\Delta h_0$ ), and the initial thermal power in the core ( $Q_{c0}$ ) are substituted in non-dimensionalized Eqs. (2.2) and (2.3) as follows:

$$M^* = \frac{M}{M_0}, \bar{h}^* = \frac{\bar{h}}{\Delta h_0}, t^* = \frac{t}{\tau} \quad (2.5)$$

$$\text{where, } \Delta h = h_{HL} - h_{CL}, \tau = \frac{M_0 \Delta h_0}{Q_{c0}}$$

Then, Eqs. (2.2) and (2.3) are reduced as the following;

$$\frac{dM^*}{dt^*} = \frac{\tau \dot{m}_{in}}{M_0} - \frac{\tau \dot{m}_{out}}{M_0} \quad (2.6)$$

$$\frac{dM^* \bar{h}^*}{dt^*} = \frac{\tau Q_c}{M_0 \Delta h_0} + \frac{\tau \dot{m}_{in}}{M_0} \cdot \frac{h_{in}}{\Delta h_0} - \frac{\tau \dot{m}_{out}}{M_0} \cdot \frac{h_{out}}{\Delta h_0} \quad (2.7)$$

In the above equations, there is flexibility in determining a time scale,  $\tau$ . For a real time simulation, the prototype and facility use the same time scale, that is  $\tau_R = 1$ . Therefore, from Eqs. (2.6) and (2.7), the scaling criteria for conserving the non-dimensional mass inventory ( $M^*$ ) and enthalpy ( $h^*$ ) are as follows:

$$\left( \frac{\dot{m}_{in}}{M_0} \right)_R = 1, \left( \frac{\dot{m}_{out}}{M_0} \right)_R = 1 \quad (2.8)$$

$$\left( \frac{Q_c}{M_0 \Delta h_0} \right)_R = 1, \left( \frac{h_{in}}{\Delta h_0} \right)_R = 1, \left( \frac{h_{out}}{\Delta h_0} \right)_R = 1 \quad (2.9)$$

Equation (2.8) requires that the safety injection and break flow should be scaled according to the ratio of the initial mass inventory. And as shown in Eq. (2.9), the thermal power in the core should be scaled by the ratio of the total energy,  $M_0 \Delta h_0$ . The major scaling factors in accordance with the energy scaling methodology are presented in Table 2.5.

## 2.2.2 Determination of the Test Conditions

It was required to determine the test conditions in accordance with the energy scaling methodology to perform the experiment using SNUF. In this study, the test conditions for SNUF were determined by scaling-down from the results of the ISP-50 test (the ATLAS test, SB-DVI-09: 50% (6 inch) break of the DVI line of the APR1400). To determine the test conditions, the steady and transient results of the thermal-hydraulic phenomena in the ATLAS test were investigated. The initial conditions and the sequence of events of the ATLAS test are summarized in Tables 2.6 and 2.7, respectively.

In Section 2.2.1, the criteria for conserving the coolant inventory and energy were obtained as indicated in Eqs. (2.8) and (2.9). To calculate the scaling parameters such as  $M_0$  and  $\Delta h_0$ , initial test conditions of SNUF should be defined in advance.

First of all, the pressure of the primary system ( $P_p$ ) and secondary system ( $P_s$ ) were reduced to 1/25 of that of the ATLAS, by considering the capability of SNUF. That is,

$$(P_p)_R = (P_s)_R = \frac{1}{25} \quad (2.10)$$

The initial cold leg fluid temperature ( $T_{CL}$ ) was determined with consideration of the heat transfer between the primary system and secondary system in the steam generators as follows.

$$(T_{CL} - T_{sat}(P_s))_R = 1 \quad (2.11)$$

The hot leg fluid temperature ( $T_{HL}$ ) was estimated to conserve the ratio of subcooling enthalpy between the hot leg and cold leg, so that the time to be saturated at each part of the primary system was scaled between SNUF and ATLAS.

$$(h_{f,sat} - h_{HL})_R = (h_{f,sat} - h_{CL})_R \quad (2.12)$$

From these results for the hot leg and cold leg conditions, the initial coolant mass inventory and the enthalpy difference could be estimated as follows:

$$M_0 \cong \rho_{avg} V_p = \rho(P_p, T_{avg}) V_p \quad (2.13)$$

$$\text{where, } T_{avg} = \frac{T_{HL} + T_{CL}}{2}$$

$$\Delta h_0 = h_{HL} - h_{CL} \quad (2.14)$$

Consequently, based on the geometry of SNUF, the test conditions such as the SI flow rate ( $\dot{m}_{in}$ ), the discharged flow rate ( $\dot{m}_{out}$ ), the core thermal power ( $Q_c$ ), and the specific enthalpy of the inlet flow ( $h_{in}$ ) could be determined with the similarities listed in Eqs. (2.8) and (2.9). Accordingly, the scaling ratio of mass and energy between SNUF and ATLAS were calculated as 1/5.6 and 1/16.4, respectively.

In detail, the ratio of the SI flow rate is equivalent to that of the initial coolant mass inventory. This is because the total mass inventory of the coolant should be

conserved during the accident according to Eq. (2.8) as follows:

$$(\dot{m}_{SI})_R = (M_0)_R \quad (2.15)$$

The flow rate of SI according to Eq. (2.15) was applied by the integrated value. In the ATLAS test, the SI water was injected in two ways, the SIP and SIT as listed in Table 2.7. As presented in Table. 2.7, the SIP operated at 54 seconds as a result of the reactor trip. The SIT valves were passively opened at 468 seconds when the primary system pressure decreased to less than 4.03 MPa in the ATLAS test. However, there existed some oscillations of the flow rate from the SIT due to actuations of the check valves located between the SIT and primary system depending on the differential pressure existing between the primary system pressure and SIT pressure as shown in Fig. 2.15. Since it was not easy to exactly simulate the oscillation of the flow rate by the pump which injects the SI water in SNUF test facility, the integrated values of the flow rate of the SI water were applied.

The area of the broken DVI nozzle should be scaled to preserve the discharge flow rate ( $\dot{m}_D$ ). In this study, the Henry-Fauske critical flow model (Henry & Fauske, 1971) was adopted to estimate the critical mass flux ( $G_c$ ) through the broken DVI nozzle. Then the ratio of the break area ( $A_R$ ) was calculated as follows:

$$(A)_R = \frac{(\dot{m}_D)_R}{(G_c)_R} = \frac{(M_0)_R}{(G_c)_R} \quad (2.16)$$

The area should be varied when the primary system pressure is reduced according to the adopted critical flow model. However, it was not possible to change the break area during the transient test, so that the area was determined by conditions during the plateau of the primary system before the loop seal clearing, which this study focused on.

The thermal power of the core was determined in the following equation, based on that the ratio of thermal power would be same with the ratio of the energy difference between the cold leg and hot leg according to Eq. (2.9).

$$(Q)_R = (M_0 \Delta h_0)_R \quad (2.17)$$

In the ATLAS test, the core power was continuously controlled to simulate 120% of the ANS73 decay curve (ANS, 1979) throughout the test. However, it was impossible to exactly simulate the power curve in SNUF, so that the integrated power should be supplied. The integrated power was composed of six steps as shown in Fig. 2.16. The criterion to divide the steps was the time when the decreasing rate of the power in the core changed rapidly. Thus, the core power of SNUF test was supplied with same value as like Fig. 2.16 for the DVI line break tests.

The ratio of the specific enthalpy of the SI water was also same with the ratio of the specific enthalpy difference between the cold leg and hot leg according to Eq. (2.9) as the following:

$$(h_{SI})_R = (\Delta h_0)_R \quad (2.18)$$

The final test conditions of SNUF for the DVI line break accident, described above, are summarized in Table 2.8.

## **2.3 Experimental Results**

According to the test conditions which were determined by the energy scaling methodology, the experimental study with SNUF was performed to simulate the DVI line break accident. A comparison of the test conditions between the specified values and measured value is listed in Table 2.8. It can be seen that the measured values for the major parameters are consistent with the target values, which were determined by the scaling methodology.

The transient results of SNUF test are illustrated in Figs. 2.17 through 2.27. To confirm that SNUF simulated well the overall thermal hydraulic phenomena, such as the system pressure, the break flow rate, and the core and downcomer water level, the test results of SNUF were compared to those of the ATLAS test in the normalized scale with an initial value.

### **2.3.1 System Pressure**

Figure 2.17 shows the primary and secondary system pressure. For SNUF, the primary system pressure was measured in the upper plenum and the secondary system pressure was estimated by the saturated pressure of the steam temperature (refer to Fig. 2.18) measured in the steam generator dome. On initiating the break, the primary system pressure decreased rapidly due to an abrupt loss of the

inventory through the broken DVI nozzle. The decreasing rate of the primary system pressure became small at around 30 seconds, then, the plateau region of the primary system pressure was appeared near the secondary system pressure. And after the plateau, the primary system pressure decreased again.

Since SNUF has smaller heat transfer area between the primary system and the secondary system (u-tube area) compared to the ATLAS, the lower temperature of the secondary system was required to maintain the initial condition. Thus, the system pressure of SNUF test was lower than those of the ATLAS test. In spite of this distortion, the overall system pressure showed good agreement between SNUF and ATLAS during the transient. And both test results showed a plateau of the pressure at  $P/P_0 \approx 0.5$  before the occurrence of the loop seal clearing.

### **2.3.2 Break Flow**

Figures 2.19 and 2.20 show the accumulated break flow measured in the discharge storage tank and the break flow rate obtained by differentiating the accumulated break flow. The liquid coolant in the reactor vessel was continuously discharged to the break until the end of the loop seal clearing. Since the upper downcomer was filled with the steam after the loop seal clearing, the discharged flow was changed from the liquid phase to the two-phase (steam-water). Thus, the increasing gradient of the accumulated break flow (refer to Fig. 2.19) and the break flow rate (refer to Fig. 2.20) became smaller after the loop seal was cleared at around 200 seconds.

A trend indicating the break flow rate increased from zero during the initial 50

seconds was observed as shown in Fig. 2.20, even though it was expected that the maximum break flow rate would be measured at zero second. It is due to the delay time caused by the measuring mechanism of the discharge storage tank. The break flow rate was estimated by the increasing rate of the water level in the discharge storage tank measured by the DP transmitter, and the water level could increase after a large amount of the steam (water discharged during initial phase vaporizes into steam in the discharge storage tank) was condensed by the spray. Thus, a delay in measurement time of approximately 20 seconds occurred as shown in Fig. 2.20.

On the other hand, there was a deviation of the accumulated break flow between SNUF and ATLAS tests. It is caused by a distortion of geometry existing in the primary system of SNUF. As listed in Table 2.4, the volume ratio of the reactor vessel (the core and downcomer) is almost the same with the design volume scale, 1/1139.2. However, the volume ratio of the primary loop parts, especially u-tubes, of SNUF is much smaller than the design volume scale. It means that the volumetric ratio between the vessel and loops in the actual one was different from that of the prototype. This distortion influenced the normalized break flow based on the initial mass of the primary system. However, the overall trends, such as the transition of the break flow rate after the loop seal clearing, were reasonably simulated in SNUF.

### **2.3.3 Collapsed Water Level in the Core and Downcomer**

Figures 2.21 and 2.22 show collapsed water levels of the downcomer and core. The upper part of the downcomer water level can be decreased when the liquid

coolant are cleared by steam flow incoming from the cold legs after the loop seal clearing. As shown in Fig. 2.21, the collapsed water level of the downcomer started to decrease after around 200 seconds in both test results. After the occurrence of the phenomenon, the steam, generated in the core, could be effectively discharged to the broken DVI nozzle through the loops of the primary system and the upper downcomer. Thus, the primary system pressure decreased after around 200 seconds as shown in Fig. 2.17. And the downcomer collapsed water level started to increase when the water in the SIT is injected into the primary system at around 480 seconds.

The core collapsed water level decreased rapidly prior to 200 seconds as illustrated in Fig. 2.22. However, the downcomer collapsed water level did not decrease before 200 seconds, even though much of the coolant in the downcomer was discharged. This discharge was originated from the differential pressure between the core and downcomer. The steam generated in the core by the thermal power increased the differential pressure between the core and downcomer. As a result, the core collapsed water level decreased and the downcomer collapsed water level was maintained during the initial period of the accident. The loop seal clearing occurred at around 200 seconds. At this time, the differential pressure between the core and downcomer was reduced. Linking the situations, it was found that the decreasing rate of the collapsed water level of the core became slower after the downcomer water level started to decrease.

However, there was a difference in the downcomer collapsed water level between SNUF and ATLAS tests. The downcomer collapsed water level of SNUF was higher after the loop seal clearing than that of the ATLAS test. As described above, the difference of the water level between the core and downcomer was

caused by the differential pressure (the core to the downcomer). The SNUF is a reduced height facility and the height of the downcomer of SNUF is 1/3.2 times of the ATLAS. Thus, higher water head in the downcomer was required to maintain the differential pressure between the core and downcomer in the normalized scale. Because of this reason, the deviation of the downcomer collapsed water level occurred.

Even though the collapsed water level of the downcomer showed a deviation, the time of events of the loop seal clearing and overall transient were preserved as well. Therefore, it was concluded that the DVI line break accident in the ATLAS test was reasonably simulated in SNUF test.

#### **2.3.4 Fluid Temperature**

Figure 2.23 shows the fluid temperature of the hot legs and cold legs. The trend of the coolant temperature was similar to the saturation temperature of the primary system pressure. Thus, the fluid temperature of each loop decreased after the loop seal clearing at around 200 seconds as described in Section 2.3.1. Even though the fluid temperature of SNUF test could not be compared with that of the ATLAS test in the normalized scale, the overall trends of the hot legs and cold legs temperature are similar as illustrated in Fig. 2.24.

Eight (8) thermocouples are installed to measure the downcomer fluid temperatures at four (4) different axial levels as illustrated in Fig. 2.13. At each level, two thermocouples are installed in the broken side and intact side. Among the thermocouples, two (2) thermocouples are located above the cold leg nozzle (the upper downcomer) and other six (6) thermocouples are located below the

cold leg nozzle (the lower downcomer). Figures 2.25 and 2.26 show the fluid temperature of the upper and lower downcomer of SNUF test, respectively. When cold water was injected to the downcomer region from SIP as shown in Fig. 2.27, the fluid temperature of the upper downcomer started to oscillate. This oscillation was due to complex mixing of the cold ECC water with the hot inventory in the downcomer region. In fact, the cold ECC water was introduced from the DVI nozzle located opposite to the broken DVI nozzle. However, significant temperature difference in the azimuthal direction (between the broken side and intact side) was not observed in the upper downcomer region as well as the lower downcomer region. These trends of the fluid temperature in the upper downcomer before loop seal clearing are similar with those of the ATLAS test as illustrated in Fig. 1.2. It means that vigorous mixing behaviors in the reactor downcomer were observed not only in the ATLAS test but also in the SNUF test. Since SNUF has similar Froude number compared to the prototype, the APR1400, it can be expected that the mixing behaviors observed in SNUF and the ATLAS tests are appeared in the prototype similarly.

## **2.4 Analytical Study**

The results of SNUF test showed that vigorous mixing behaviors in the reactor downcomer appeared in the test facility, which has a similar aspect ratio and Froude number compared to the prototype. Although it was known in the ISP-50 that the prediction capability of the thermal hydraulic system codes to simulate the multidimensional liquid phase mixing behavior was not appropriate, SNUF test

was also simulated with the system code for an additional conformation of the limitation of the prediction capability regarding the mixing behaviors. In this study, MARS-KS 1.3 was utilized for simulation of SNUF test to validate the calculation capability of the code.

#### **2.4.1 Characteristic of MARS**

The MARS, a best-estimated system analysis code, was developed by KAERI, adopting RELAP5 (U.S. NRC, 1999) and COBRA-TF (Thurgood et al., 1983) as the one-dimensional module and the three-dimensional module, respectively (KAERI, 2009). Although COBRA-TF module can handle the multi-channel flow, there were limitations for the application of shear terms and cylindrical coordinate system. Thus, KAERI developed a new multidimensional component, named MultiD, in MARS to overcome these limitations, to get the more flexible three-dimensional capabilities in the system code, and to allow users to model more accurately the multidimensional hydrodynamic features of reactor application such as the reactor downcomer. The MultiD component defines a one, two, or three dimensional array of volumes and the internal junctions connecting these volumes. The geometry can be either cartesian ( $x, y, z$ ) or cylindrical ( $r, \theta, z$ ). And the full three-dimensional convection and diffusion terms are implemented in the momentum equation.

In MARS, the momentum flux terms are implemented for the three-dimensional momentum equations. As an example, the momentum control volume for flow in the  $x$  direction in the  $x$ - $y$  plane is shown in Fig. 2.28. For MultiD component in MARS, the momentum flux term in the  $x$  direction is given by:

$$u \frac{\partial u}{\partial x} + v \frac{\partial u}{\partial y} + w \frac{\partial u}{\partial z} \quad (2.19)$$

where  $u$ ,  $v$ , and  $w$  are the  $x$ ,  $y$ , and  $z$  velocities respectively. By expanding each of the terms in Eq. (2.19) in finite difference form using a donor formulation, the following equation can be obtained:

$$\begin{aligned} & \frac{(\alpha_g \rho_g)_j (\bar{u}_g u_g)_L - (\alpha_g \rho_g)_j (\bar{u}_g u_g)_K}{2\Delta x_{j,k,l}} \\ & + \frac{(\alpha_g \rho_g)_j (u_g)_j \bar{v}_{g,k+1} - (\alpha_g \rho_g)_j (u_g)_j \bar{v}_{g,k}}{\Delta y_{j,k,l}} \\ & + \frac{(\alpha_g \rho_g)_j (u_g)_j \bar{w}_{g,l+1} - (\alpha_g \rho_g)_j (u_g)_j \bar{w}_{g,l}}{\Delta z_{j,k,l}} \end{aligned} \quad (2.20)$$

where  $\alpha_g$  is the void fraction and  $\rho_g$  are the vapor density. In Eq. (2.20), the average velocity  $\bar{v}$  and  $\bar{w}$  are the average of the four (4) surrounding junction velocity. That is,

$$\bar{v}_{g,k+1} = \frac{1}{2} (v_{g,j,k+1,l} + v_{g,j-1,k+1,l}) \quad (2.21)$$

$$\bar{v}_{g,k} = \frac{1}{2} (v_{g,j,k,l} + v_{g,j-1,k,l}) \quad (2.22)$$

$$\bar{w}_{g,l+1} = \frac{1}{2} (w_{g,j,k,l+1} + w_{g,j-1,k,l+1}) \quad (2.23)$$

$$\bar{w}_{g,l} = \frac{1}{2}(w_{g,j,k,l} + w_{g,j-1,k,l}) \quad (2.24)$$

The momentum flux terms in the y and z directions can be also given by similar method as described above. According to the above equations, the velocity of all adjacent internal junctions should be considered to calculate the momentum flux term of an internal junction in the MultiD component. Due to these characteristics of the MultiD component in MARS, it has been expected that the multidimensional thermal-hydraulic phenomenon could be predicted more appropriately if the MultiD Component is applied.

#### **2.4.2 SNUF Modeling for the Code Assessment**

For estimating the multidimensional prediction capability of MARS, SNUF test was analyzed with MARS. Nodalization was made as illustrated in Fig. 2.29. The SNUF model consisted of a test vessel, two (2) hot legs, two (2) steam generators, and four (4) cold legs. The test vessel consisted of the lower plenum (C160 and C190), core (C190), upper plenum (C210 and C220), and downcomer (C170).

To simulate the multidimensional phenomenon in the downcomer, the downcomer was modelled by the MultiD component, and was divided into six (6) regions in the azimuthal direction. Along the vertical direction, the downcomer had twelve (12) nodes.

The RCPs (Reactor Coolant Pumps) were stopped to act as a resistance to increasing differential pressure between the upper plenum and downcomer during the accident in the prototype. In order to simulate the RCP in SNUF, an orifice

plate was installed in each cold leg. The pressure loss coefficients were modelled to consider pressure drops through the RCPs (C370, C390, C470, and C490).

As a flow boundary, the intact DVI nozzles (J911, J912, and J914) were connected to the upper downcomer to supply the SI water from the tank (C910, C920, and C940). The break valve (V913) simulated the DVI line break, and the time dependent volume (C954) was utilized to simulate the discharge storage tank.

The core barrel was modelled as a heat structure to transfer the heat between the core and downcomer. The test vessel and pipes were modelled by adding a heat structure to simulate the heat loss to the surroundings.

The primary side component of the steam generator included the inlet plenum (C340 and C440), tube region (C350 and C450), and outlet plenum (C360 and C460). The secondary side consisted of the downcomer (C602 and C702), riser (C610 and C710), separator (C620 and C720), and dome region (C630 and C730).

### **2.4.3 Analysis Results of SNUF Test by MARS**

The SNUF test was simulated with MARS code based on the measured test conditions listed in Table 2.8 as the boundary conditions. As shown in Fig. 2.30, the decreasing rate of the primary system pressure of the test was well consistent with MARS. Especially, the time to decrease the primary system pressure after the plateau region showed good agreement between the experiment and analysis. Since the primary system pressure was simulated well by the code, the fluid temperature of the loop (such as the hot legs and cold legs) was also well consistent with the calculation results as illustrated in Figs. 2.31 and 2.32.

Figures 2.33 and 2.34 show the comparison of the injection flow rate and the

break flow rate respectively between the test and analysis. Since the injection flow rate is a boundary conditions for the analysis, the time-dependent SI flow rate based on the measured flow rate was simulated in the MARS calculation. There was a deviation of the break flow rate between the test and analysis during the initial period. It is due to the delay time caused by the measuring mechanism of the discharge storage tank as described in Section 2.3.2. For the accumulated break flow, the results of the analysis showed good agreement as illustrated in Fig. 2.35.

The collapsed water level in the downcomer and core was similarly simulated with MARS as shown in Figs. 2.36 and 2.37, respectively. The decrease of the downcomer collapsed level at around 200 seconds means that the loop seal clearing occurred. Thus, it was concluded that the loop seal clearing was predicted reasonably with MARS. The core collapsed water level also was calculated relatively well by MARS.

On the other hand, the fluid temperature in the downcomer before the loop seal clearing focused in this study regarding the multidimensional liquid phase mixing behavior, is illustrated in Fig. 2.38. This figure shows the water temperature of the downcomer between the cold leg nozzle and DVI nozzle. One temperature value was measured or calculated in the broken side and the other was for the intact side located opposite to the broken side. As described in Section 2.3.4 and shown in Fig. 2.38, even though there was an oscillation of the fluid temperature of the downcomer, the temperature difference in the azimuthal direction (between the broken side and intact side) of the downcomer was not observed in the experiment. However, the fluid temperature of the intact side was lower around 10 K than that of the broken side according to the analysis result. It

means that the azimuthal temperature stratification was predicted by MARS.

The comparison result of SNUF test and its analysis was consistent with the conclusion of ISP-50. From the results of the independent test with SNUF and the analysis with MARS, the limitation of the prediction capability of the thermal hydraulic system code to simulate the multidimensional liquid phase mixing behavior was reconfirmed with the experimental and analytical method. Based on the results of this study and ISP-50, the need to improve the capability of the system code to predict the mixing behavior in the downcomer increased so that the study to investigate the mixing behavior in the downcomer annulus and improve the system code was carried out as described in Chapter 3.

Table 2.1 Major information of the discharge storage tank

<b>Parameter</b>	<b>Value</b>	<b>Unit</b>
Outer diameter of the tank	1.0	m
Thickness of the tank wall	3.0	mm
Height of main part of the tank	1.5	m
Total flow rate of spray water	1.0	kg/s
Number of spray nozzle	12	EA
Inner diameter of spray nozzle	1/4	inch
Diameter of droplet	< 1.0	mm

Table 2.2 Major information of the broken DVI nozzle

<b>Parameter</b>	<b>Value</b>	<b>Unit</b>
Inner diameter of the nozzle between the downcomer wall and orifice	15.8	mm
Inner diameter of the nozzle between the orifice and discharge storage tank	62.7	mm
Length of the nozzle between the downcomer wall and orifice	40.0	mm
Length of the nozzle between the orifice and discharge storage tank	1250	mm

Table 2.3 Major information of the heat removal system

<b>Parameter</b>	<b>Value</b>	<b>Unit</b>
Minimum flow area (per each steam generator)	344	mm <sup>2</sup>
Feedwater flow rate (per each steam generator)	0.39	kg/s
Number of the cooling coils	6	EA
Inner diameter of the cooling coils	9.5	mm
Length of the cooling coils	4	m
Number of the chillers	2	EA
Heat removal capability of the chillers	140	kW

Table 2.4 Major design characteristics of SNUF compared to the prototype

<b>Parameter</b>	<b>SNUF</b>	<b>APR1400</b>	<b>Remark</b>
Number of loops	2	2	
Volume scale	1/1139.2	-	
Area scale	1/178	-	
Height scale	1/6.4	-	
Active core height, m	0.6	3.81	
Primary side volume, m <sup>3</sup>	0.224	353.72	volume ratio
Core volume	0.117	122.24	1/1045
Downcomer volume	0.034	36.64	1/1078
Hot leg volume	0.007	11.09	1/1584
Cold leg volume	0.017	28.17	1/1657
U-tube volume	0.049	155.58	1/3175
Downcomer gap size, m	0.020	0.255	
Hot leg inner diameter, m	0.064	1.067	
Cold leg inner diameter, m	0.051	0.762	
DVI nozzle diameter, m	0.016	0.216	
Fuel rod diameter, m	0.011	0.0095	
Number of fuel load	150	56876	

Table 2.5 Major scaling ratio of SNUF

Parameter	Scaling law	SNUF design (scale down the APR1400)	SNUF design (scale down the ATLAS)
Length	$l_{OR}$	1/6.4	1/3.2
Diameter	$d_{OR}$	$1/178^{1/2}$	1/1.11
Flow area	$d_{OR}^2$	1/178	1/1.24
Volume	$l_{OR} d_{OR}^2$	1/1139.2	1/3.96
Time scale	1	1	1
Mass inventory	$\rho_R l_{OR} d_{OR}^2$	1/872	1/5.6
Thermal power	$\rho_R l_{OR} d_{OR}^2 \Delta h_{OR}$	1/2560	1/16.4
Flow rate	$\rho_R l_{OR} d_{OR}^2$	1/872	1/5.6
Velocity	$l_{OR}$	1/6.4	1/3.2
Break area	$\rho_R l_{OR} d_{OR}^2 / G_{CR}$	1/159	1/1.02

Table 2.6 Initial conditions of the ATLAS test (OECD/NEA, 2012)

<b>Parameter</b>	<b>Value</b>	<b>Remarks</b>
<b>Primary system</b>		
Core power, MW	1.636	including heat loss
PZR pressure, MPa	15.596	
Core inlet temperature, K	563.2	
Core exit temperature, K	598.2	averaged value
Hot leg temperature, K	597.6/598.5	hot leg 1/2
Cold leg temperature, K	565.4/565.3/565.0/565.2	cold leg 1A/1B/2A/2B
<b>Secondary System</b>		
Steam dome pressure, MPa	7.83/7.83	SG 1/2
Steam temperature, K	566.3/566.1	SG 1/2
<b>ECCS</b>		
RWT temperature, K	323.3	
SIT temperature, K	323.3~323.7	
SIP flow rate, kg/s	0.2016	Note 1)
SIP + SIT flow rate, kg/s	0.5857	Note 2)
<b>Broken DVI nozzle</b>		
Break size, mm	10.8	Inner diameter of nozzle

Note 1) averaged SI flow rate between start time of SIP injection and start time of SIT injection

Note 2) averaged SI flow rate between start time of SIT injection and 600 seconds

Table 2.7 Sequence of events for the ATLAS test (OECD/NEA, 2012)

<b>Events</b>	<b>Time, sec</b>	<b>Description</b>
Break open	0	
Low pressurizer pressure (LPP) trip	26	If pressurizer pressure < 10.72 MPa
Reactor scram & RCP trip	LPP + 0.35	
Turbine isolation	LPP + 0.07	
Main feedwater isolation	LPP + 7.07	
SIP pump start	LPP + 28.28	
	54	
SIT start	468	If downcomer pressure < 4.03 MPa

Table 2.8 Target and measured test conditions of SNUF

Parameter	Target value	Measured value	Remarks
Core power, kW			
0 ~ 25 sec		100	
25 ~ 60 sec		80	
60 ~ 120 sec		60	averaged values
120 ~ 200 sec		50	(6 steps)
200 ~ 500 sec		40	
500 ~ sec		35	
Primary system			
System pressure, bar	6.24	6.22	1/25 (pressure ratio)
Hot leg temperature, K	421.7	422.2/422.8	hot leg 1/2
Cold leg temperature, K	406.7	405.0/405.4/405.8/405.4	cold leg 1A/1B/2A/2B
Secondary System			
Steam temperature ,K	408.1	404.3/404.1	SG 1/2
ECCS			
SI water temperature, K	290.7	301.5~302.1	
SIP flow rate, kg/s	0.036	0.041	averaged value
SIP + SIT flow rate, kg/s	0.105	0.120	averaged value
SIP injection time, sec	54	50	
SIT injection time, sec	468	480	
Broken DVI nozzle			
Break size, mm		11.1	inner diameter of orifice

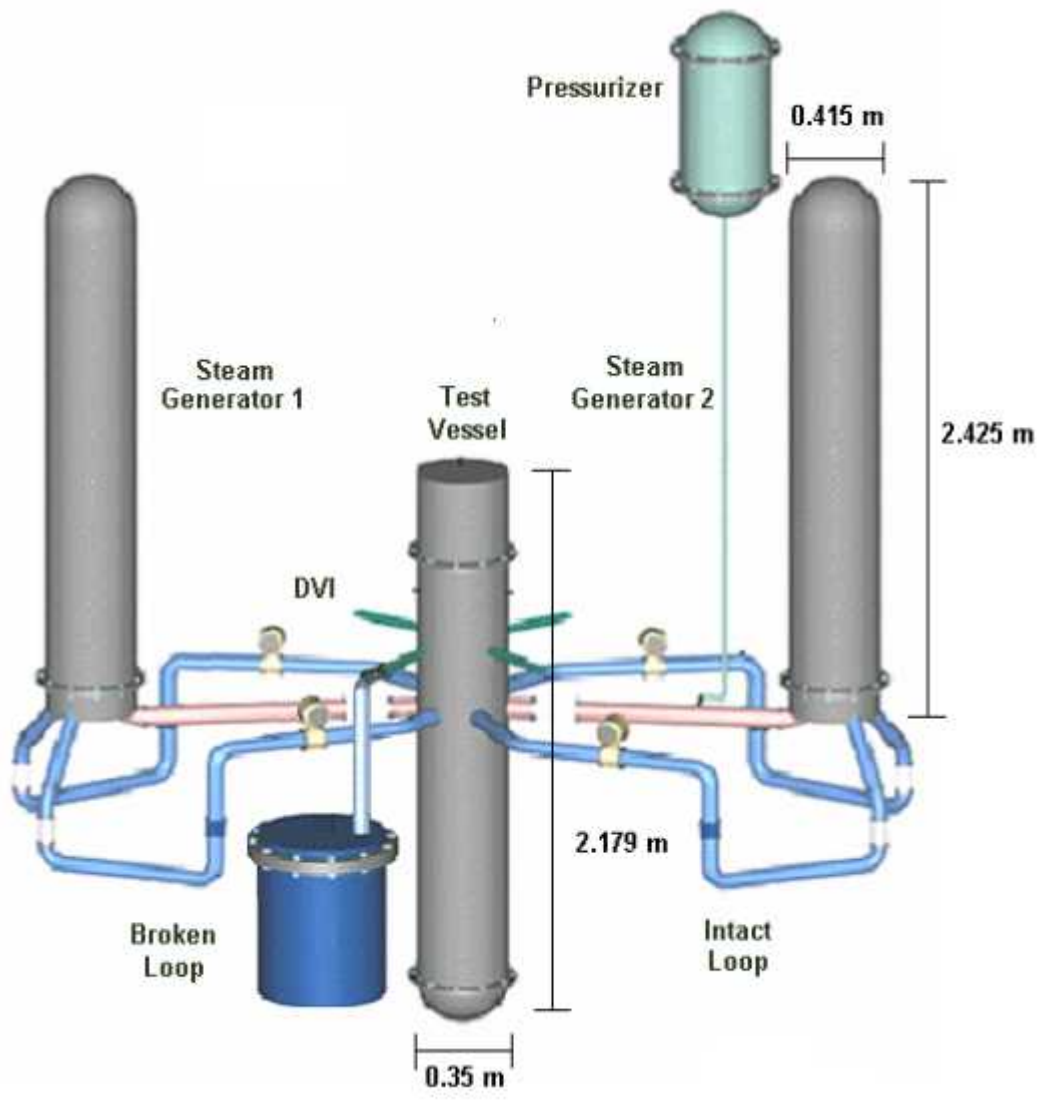


Figure 2.1 Schematic diagram of SNUF

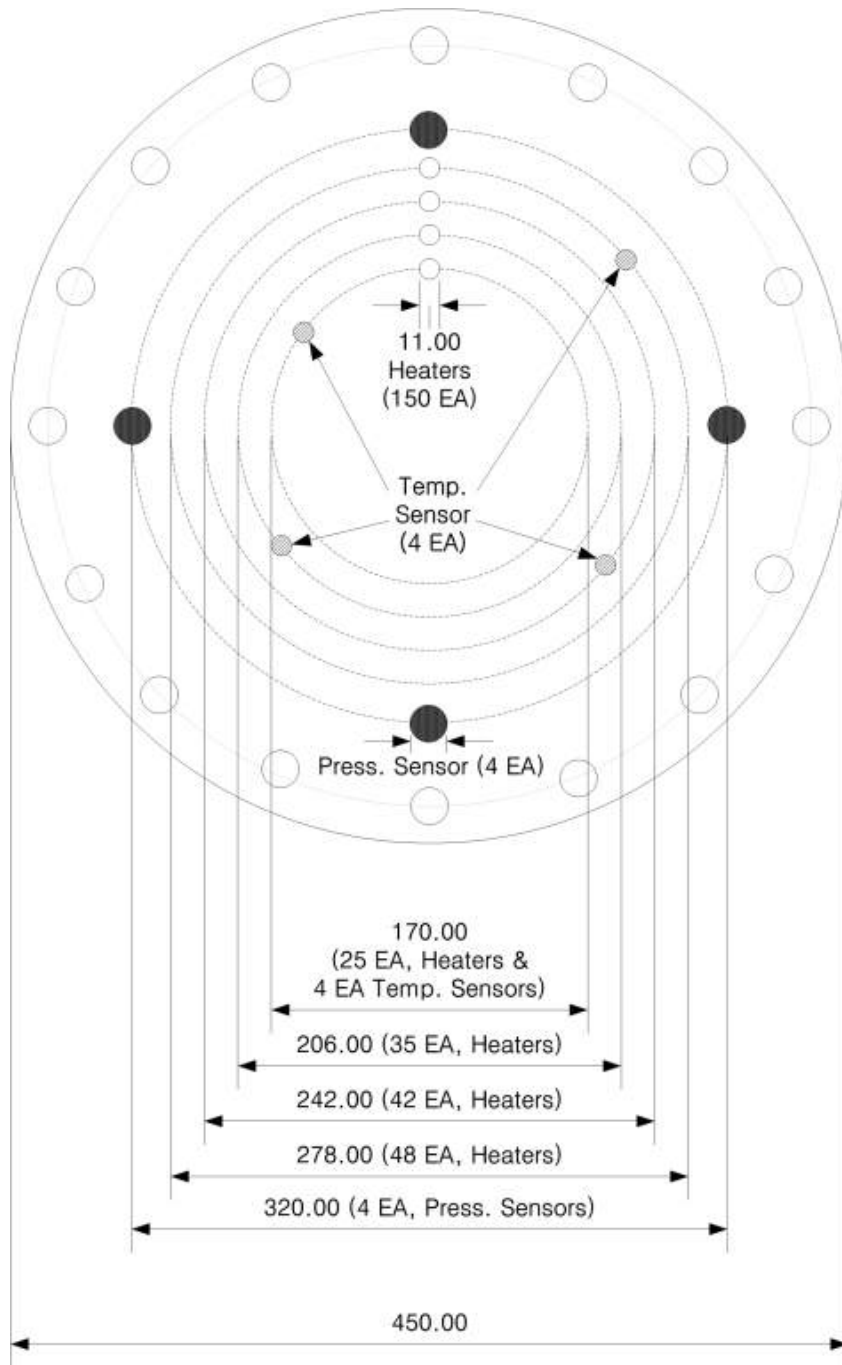


Figure 2.2 Heaters and instrumentation in the core of SNUF

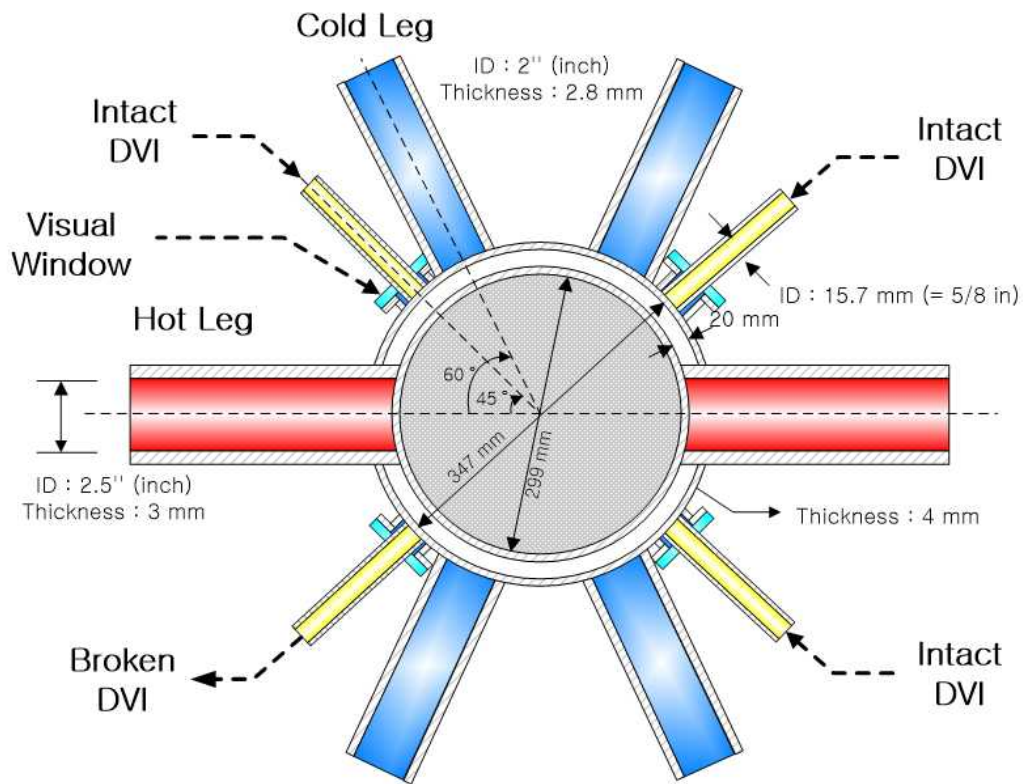


Figure 2.3 Plan view of SNUF

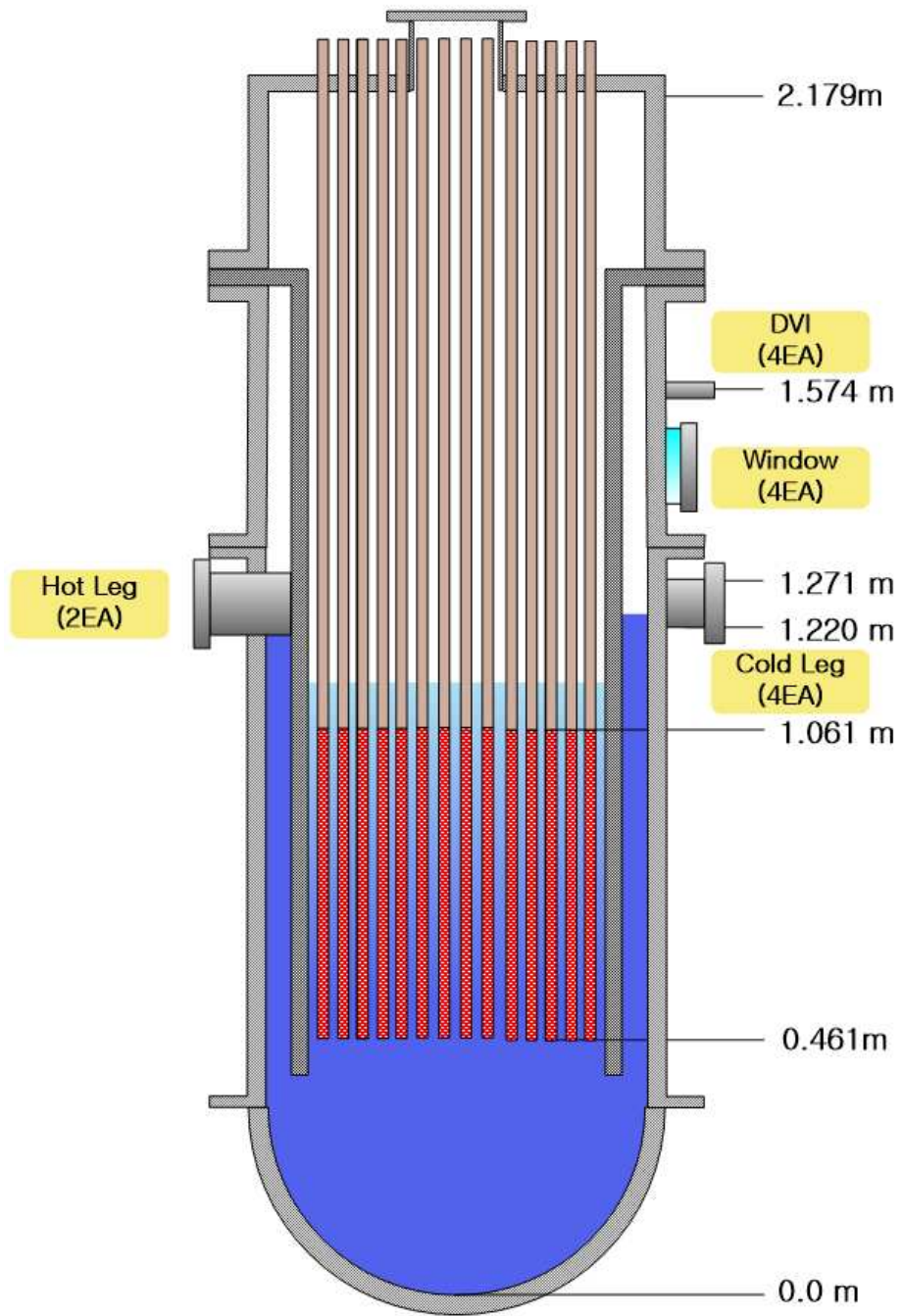


Figure 2.4 Cross-sectional view of SNUF

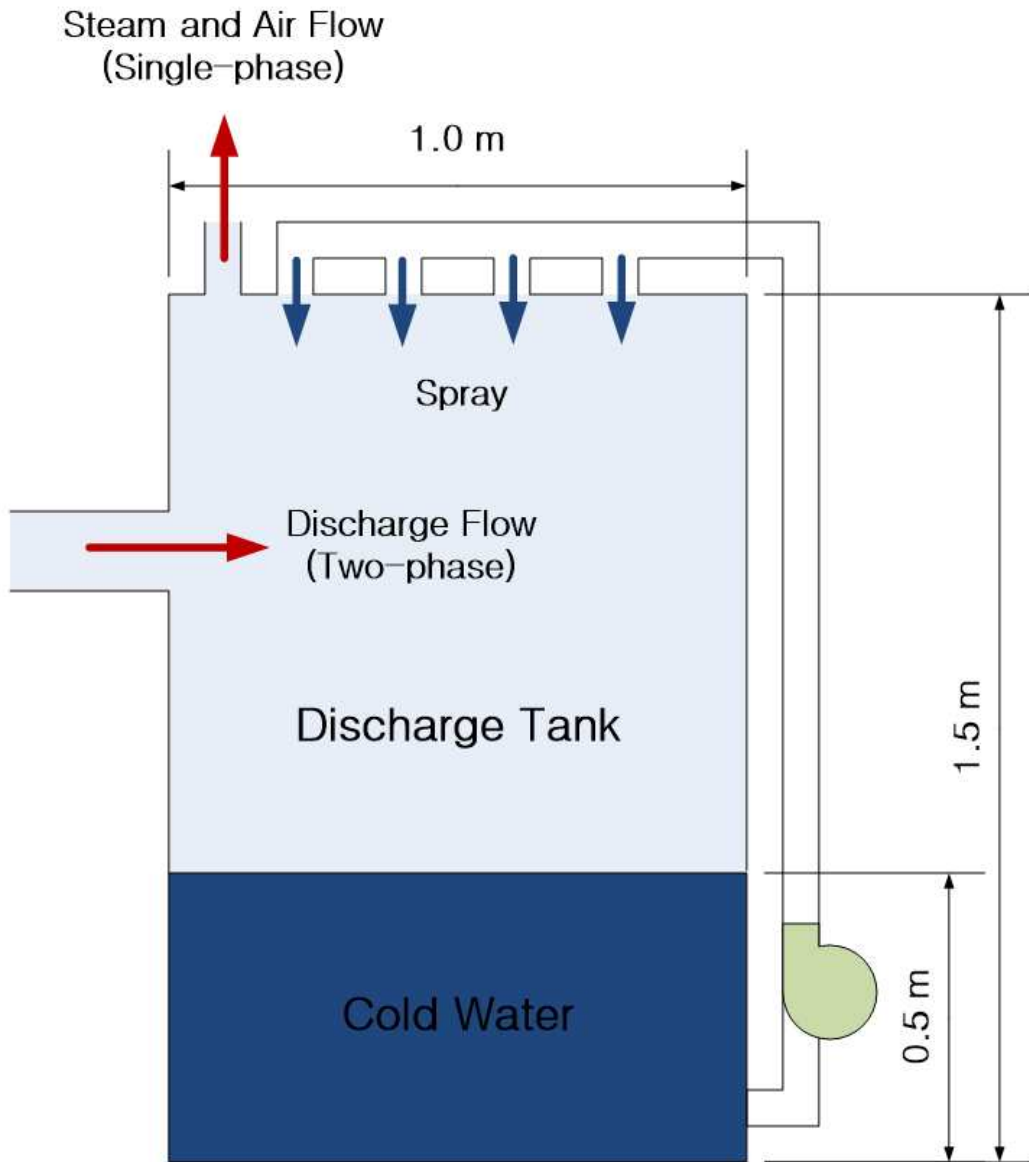
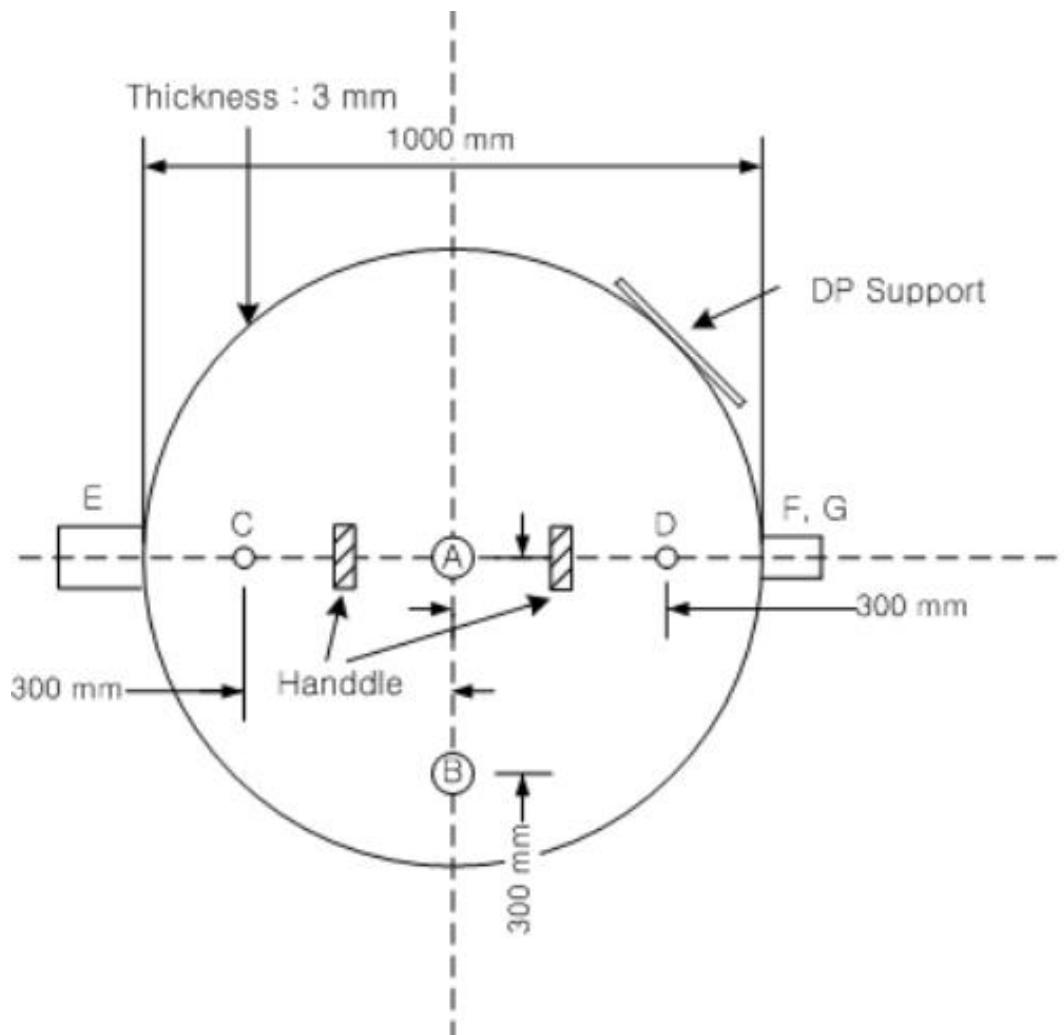


Figure 2.5 Schematic diagram of the discharge storage tank



- A: inlet of the spray water
- B: drain line
- C: pressure measuring line
- D: temperature measuring line
- E: inlet of the break water
- F: outlet of steam and air flow
- G: outlet of the spray water

Figure 2.6 Design drawing of the discharge storage tank (plan view)

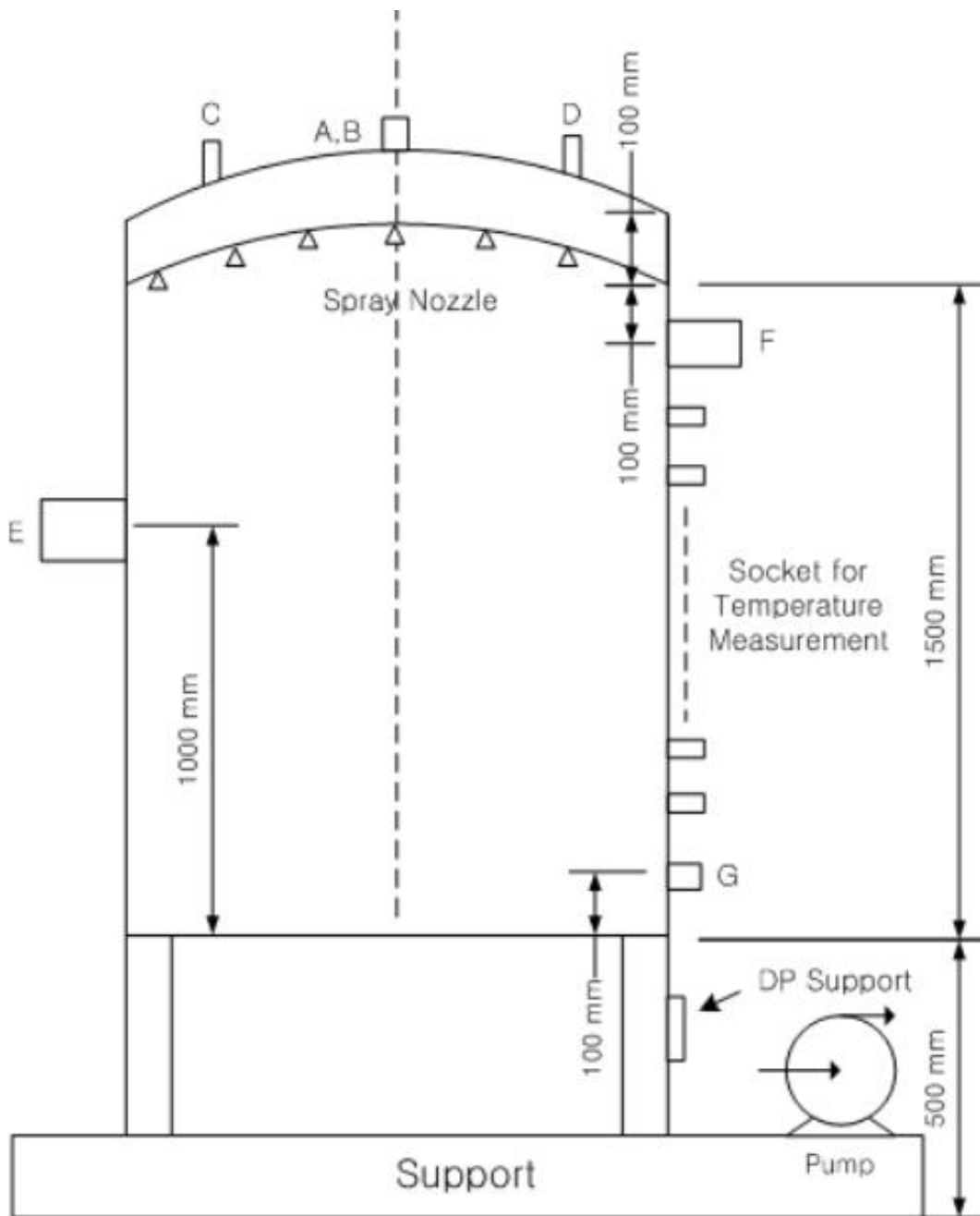


Figure 2.7 Design drawing of the discharge storage tank (cross-sectional view)

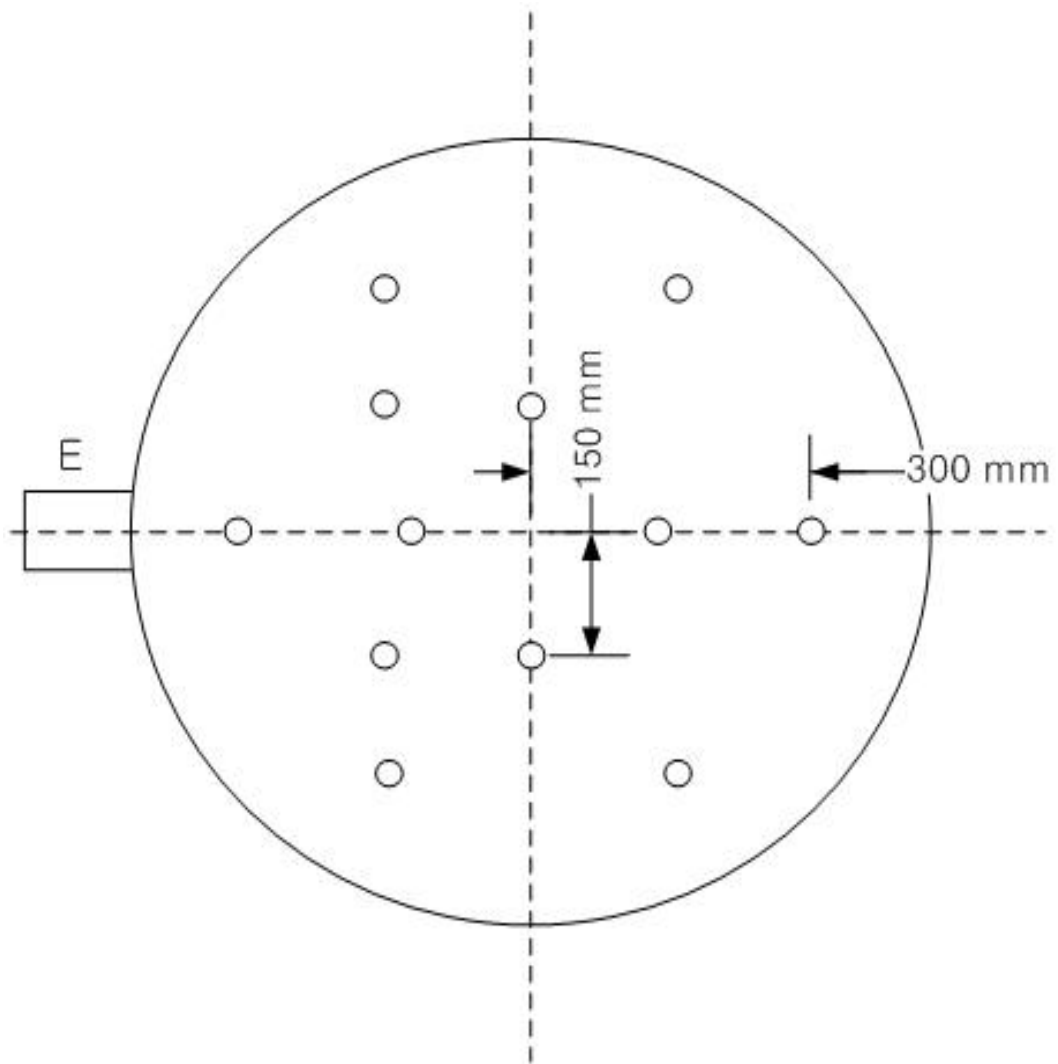


Figure 2.8 Design drawing of the discharge storage tank (location of the spray nozzle)

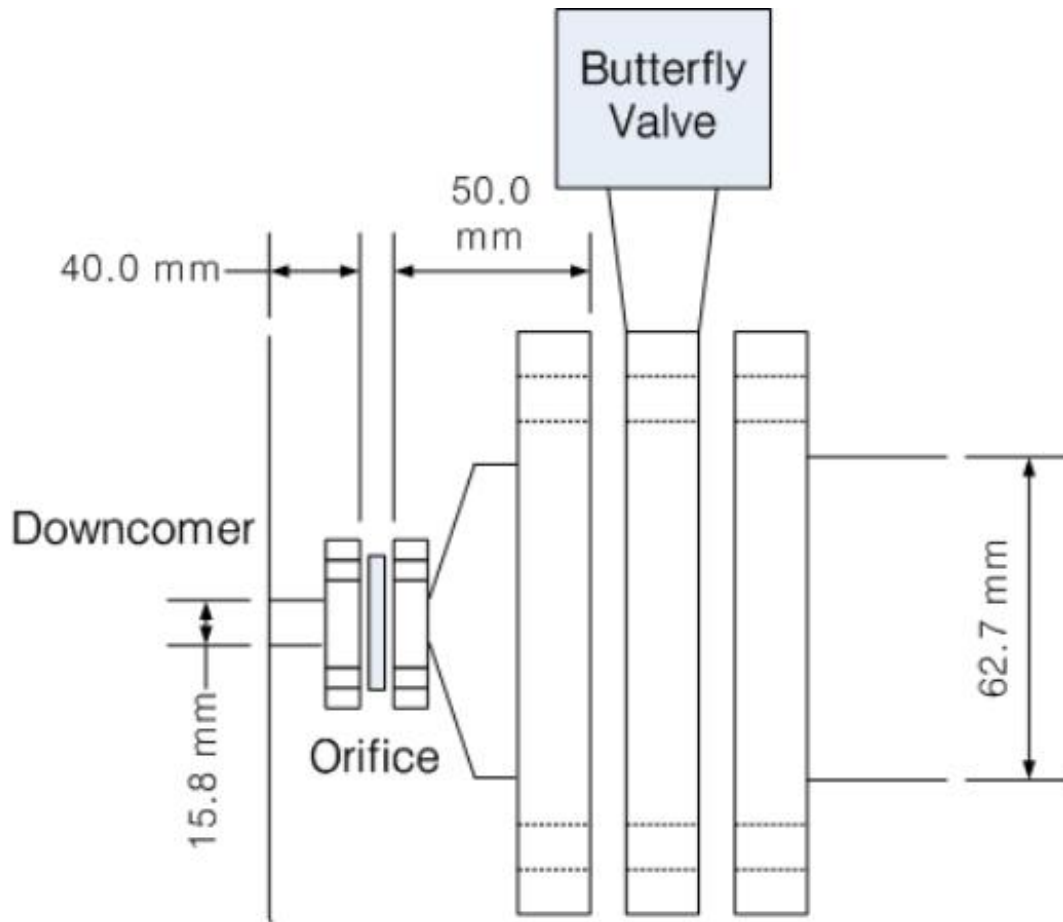


Figure 2.9 Schematic diagram of the broken DVI nozzle

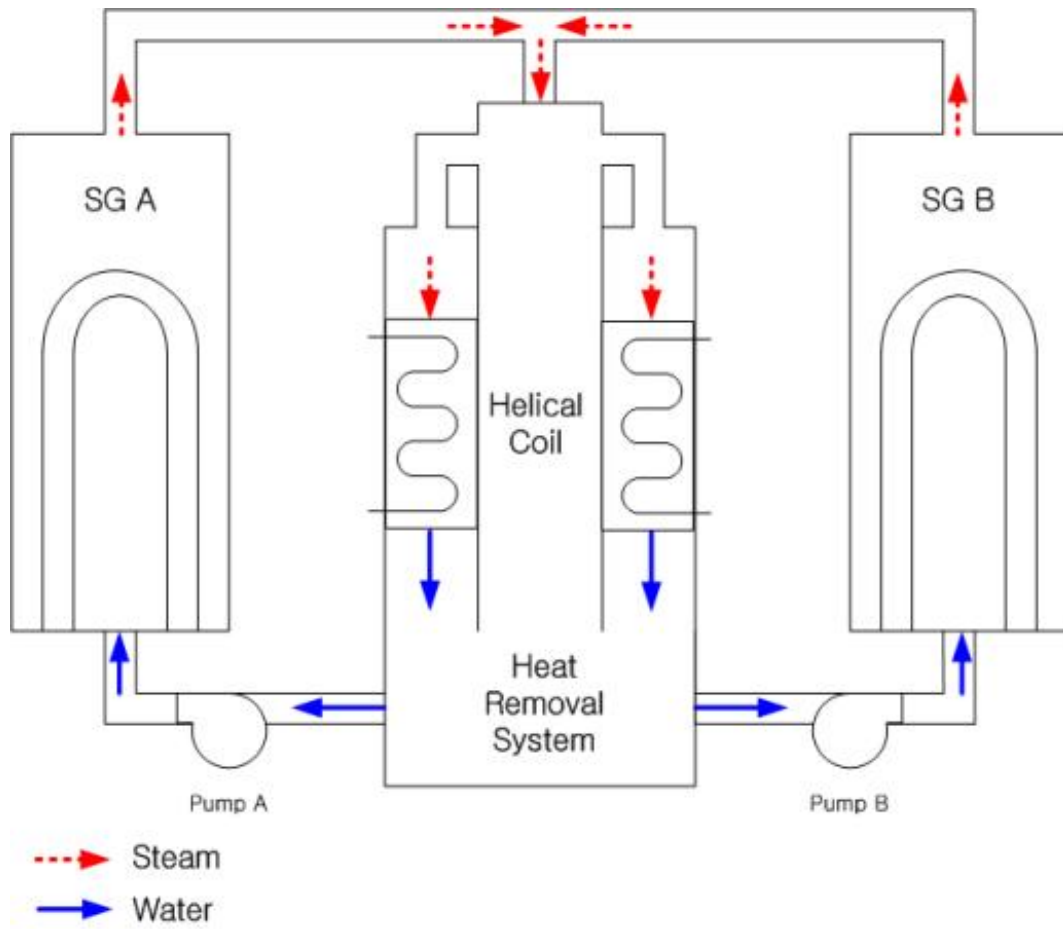


Figure 2.10 Schematic diagram of the heat removal system

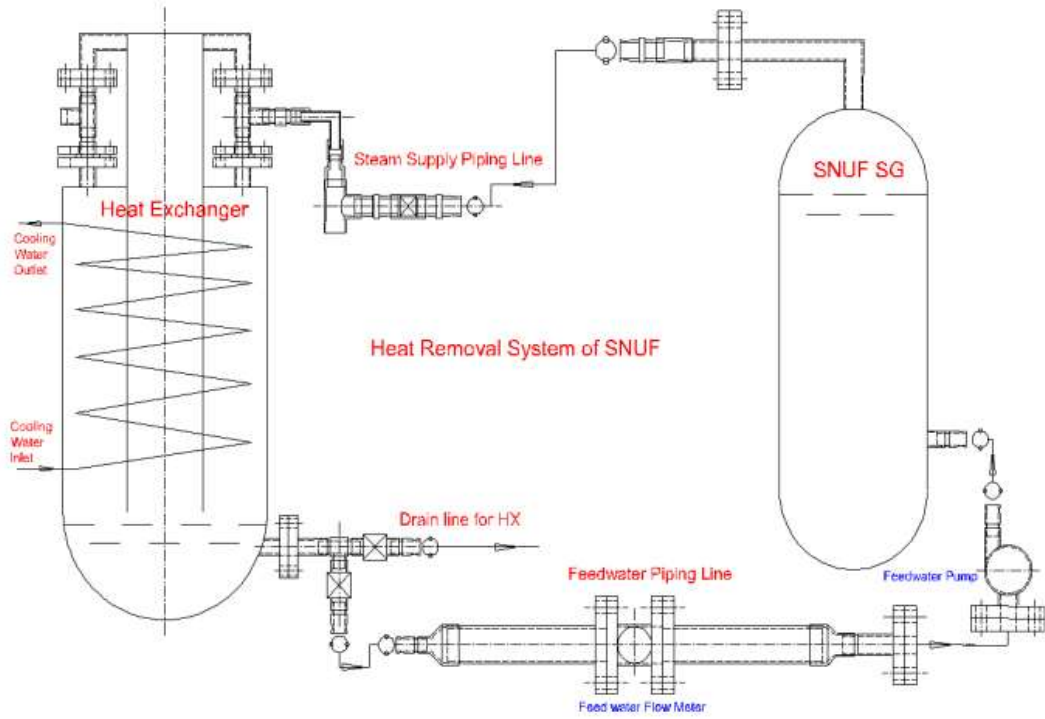


Figure 2.11 Design drawing of the heat removal system

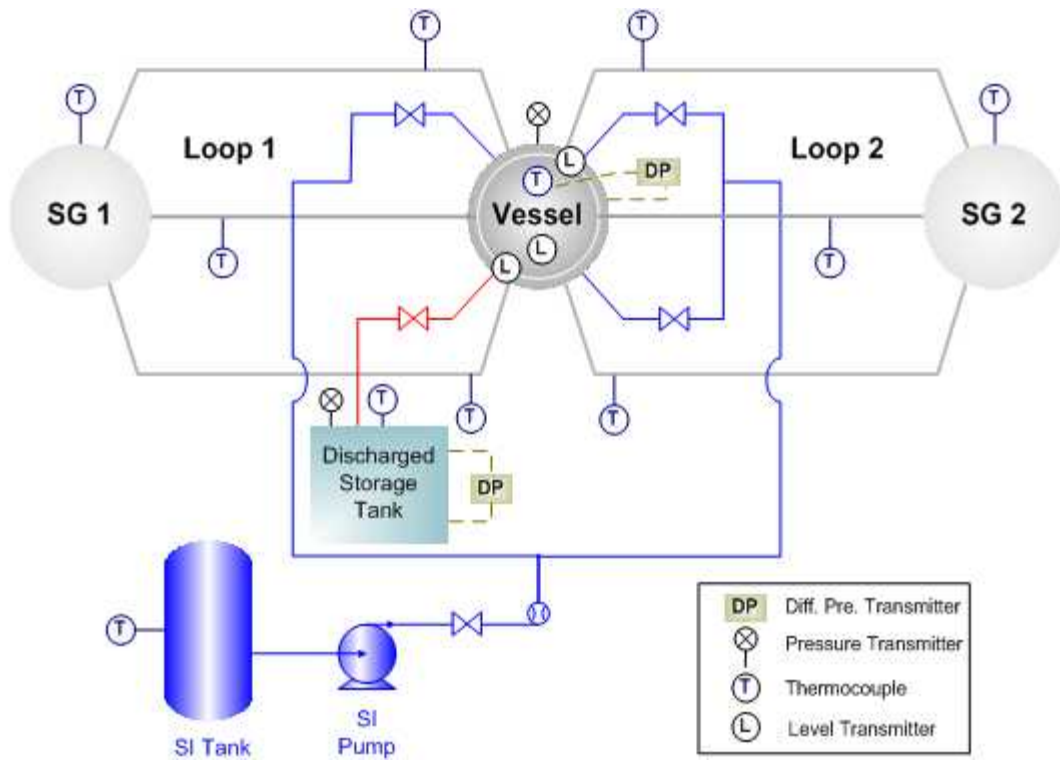


Figure 2.12 Instrumentation system of SNUF

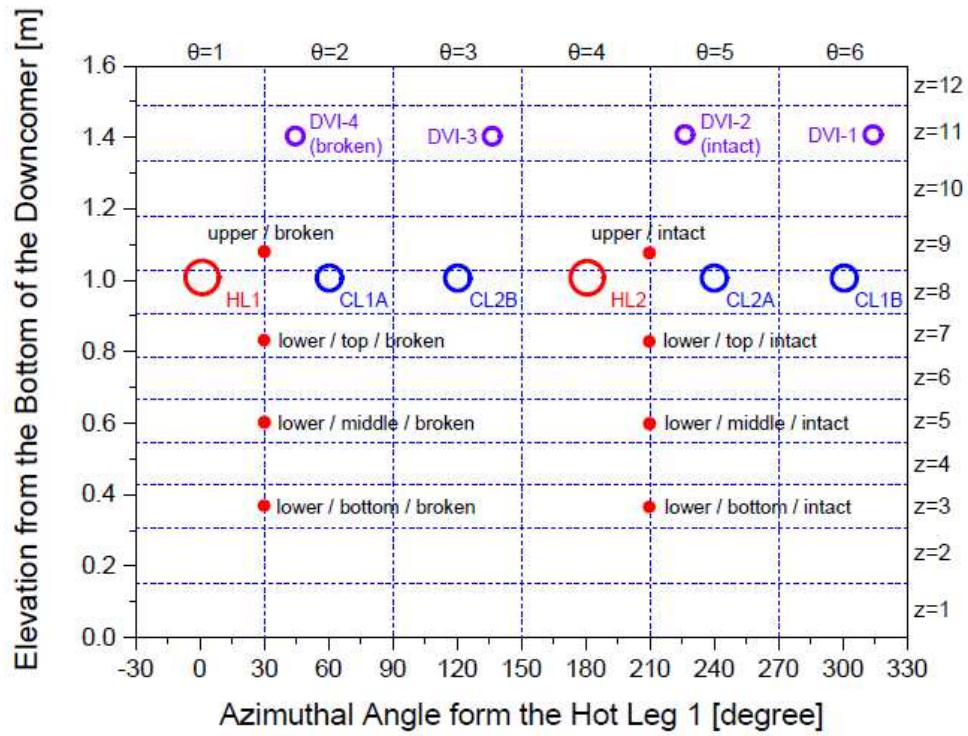


Figure 2.13 Fluid temperature measurement locations in the downcomer of SNUF



(a) inside view



(b) outside view

Figure 2.14 Visualization windows of SNUF

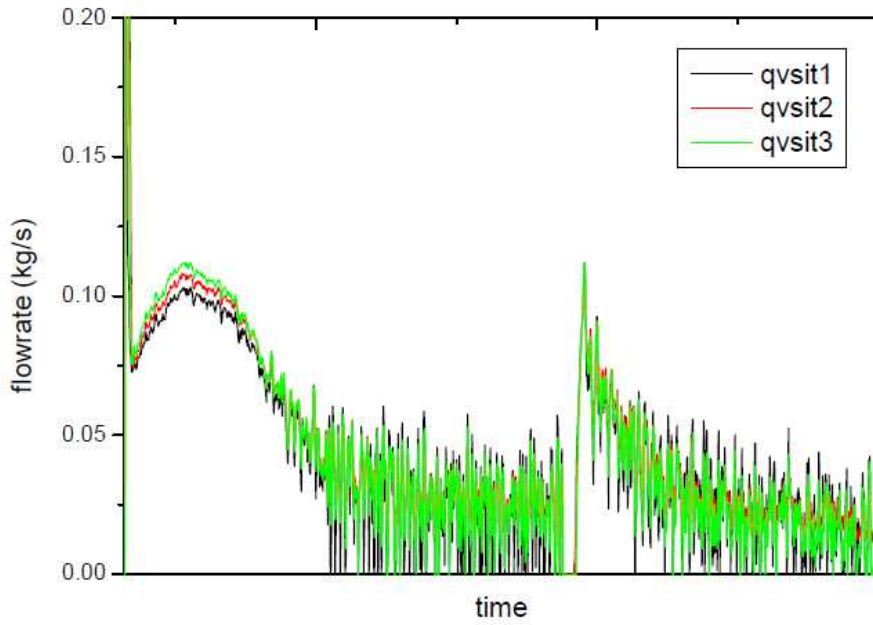


Figure 2.15 SI flow rate from the SITs in the ATLAS test (OECD/NEA, 2012)

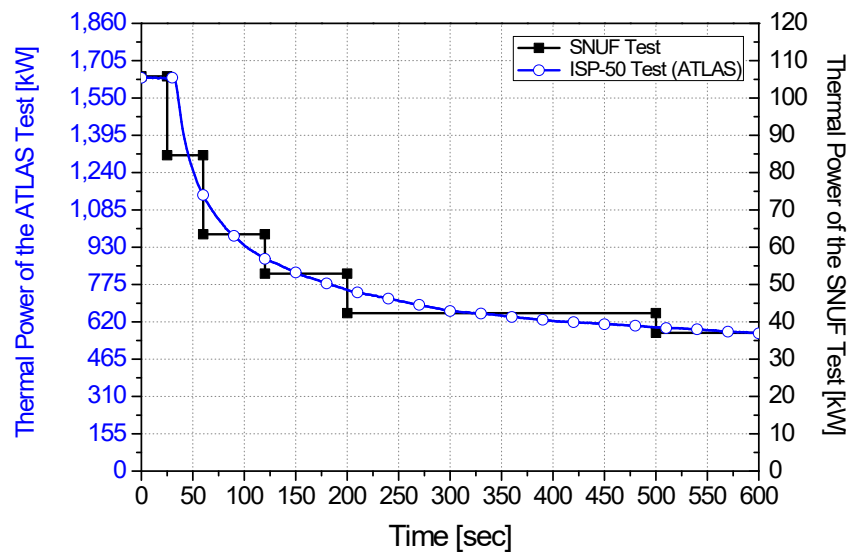


Figure 2.16 Comparison of the thermal power between SNUF and ATLAS tests

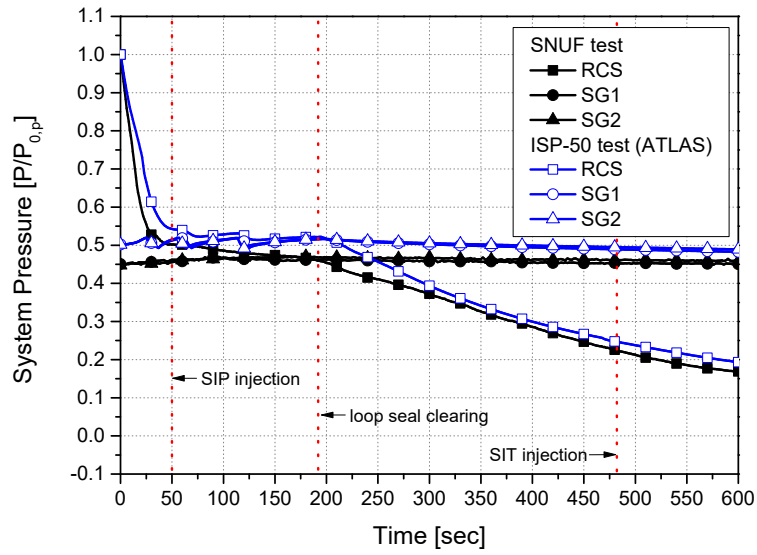


Figure 2.17 Comparison of the system pressure between SNUF and ATLAS tests in the normalized scale

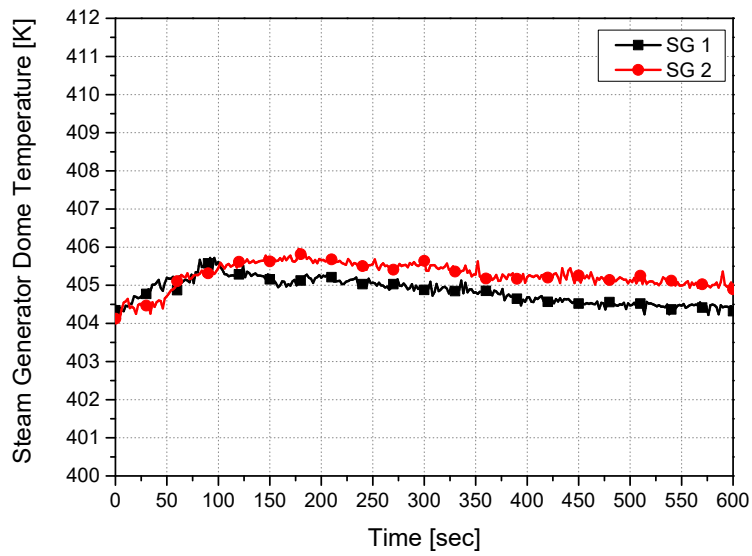


Figure 2.18 Steam dome temperature (steam) of SNUF test

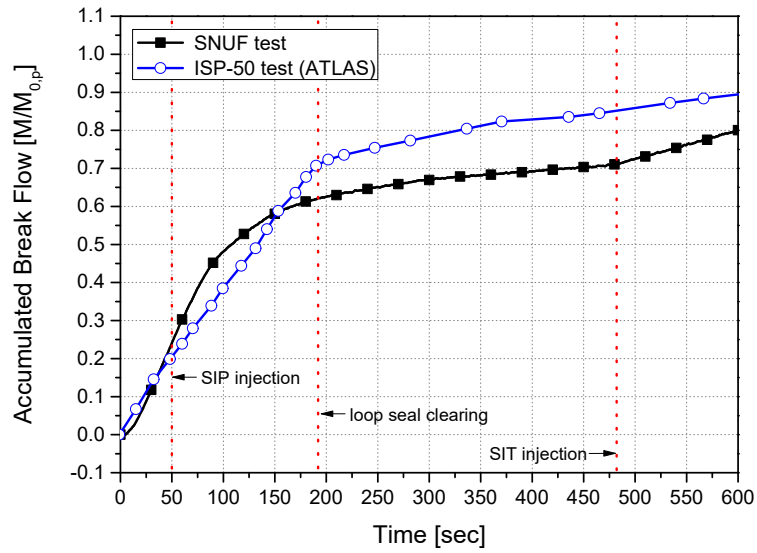


Figure 2.19 Comparison of the accumulated break flow between SNUF and ATLAS tests in the normalized scale

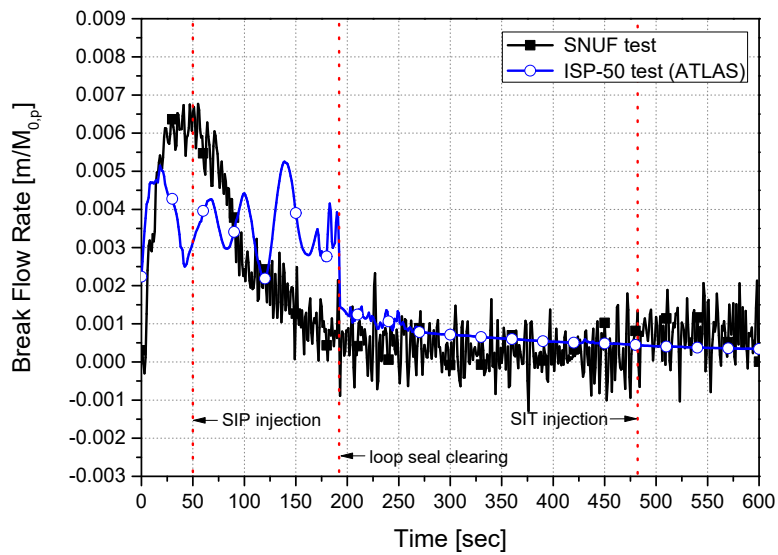


Figure 2.20 Comparison of the break flow rate between SNUF and ATLAS tests in the normalized scale

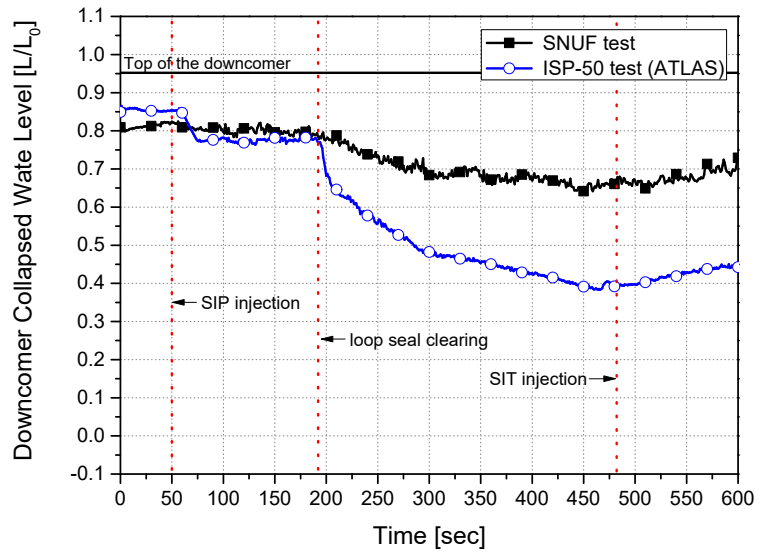


Figure 2.21 Comparison of the downcomer collapsed water level between SNUF and ATLAS tests in the normalized scale

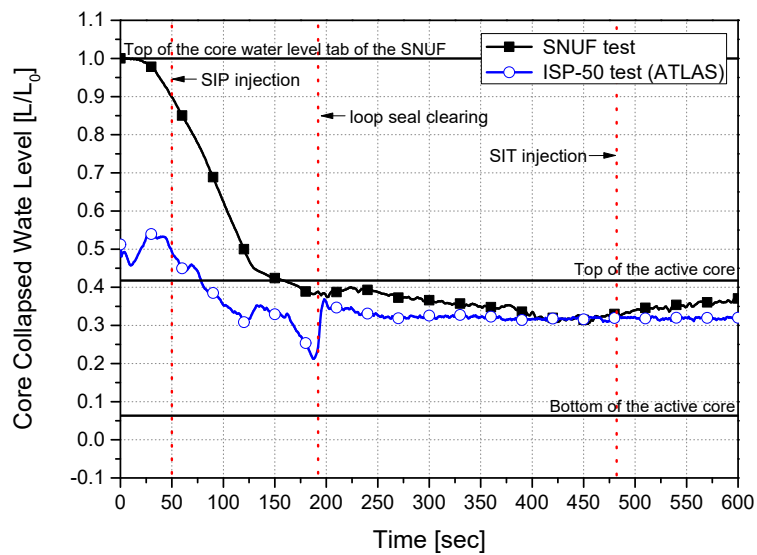


Figure 2.22 Comparison of the core collapsed water level between SNUF and ATLAS tests in the normalized scale

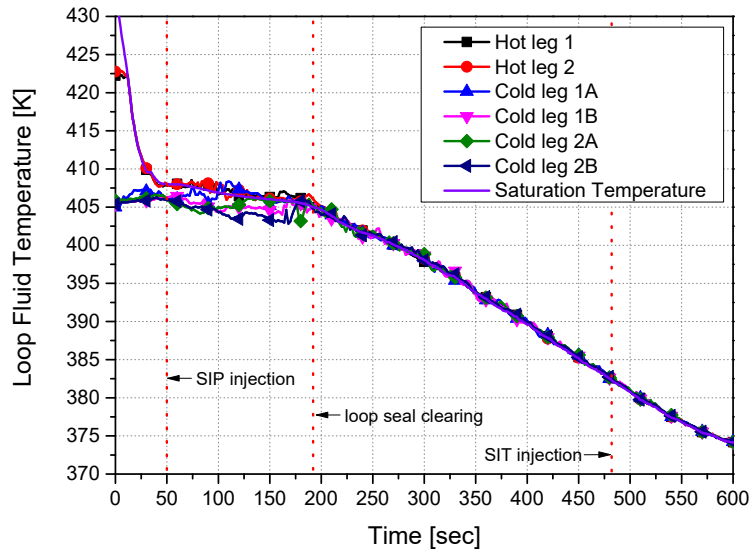


Figure 2.23 Loop fluid temperature of SNUF test

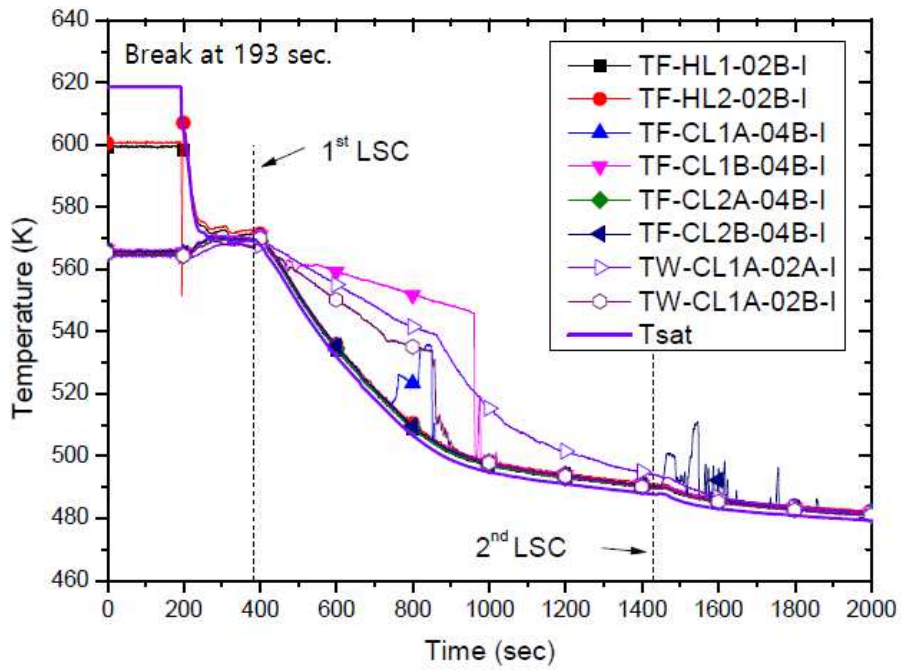


Figure 2.24 Loop fluid temperature of the ATLAS test (OECD/NEA, 2012)

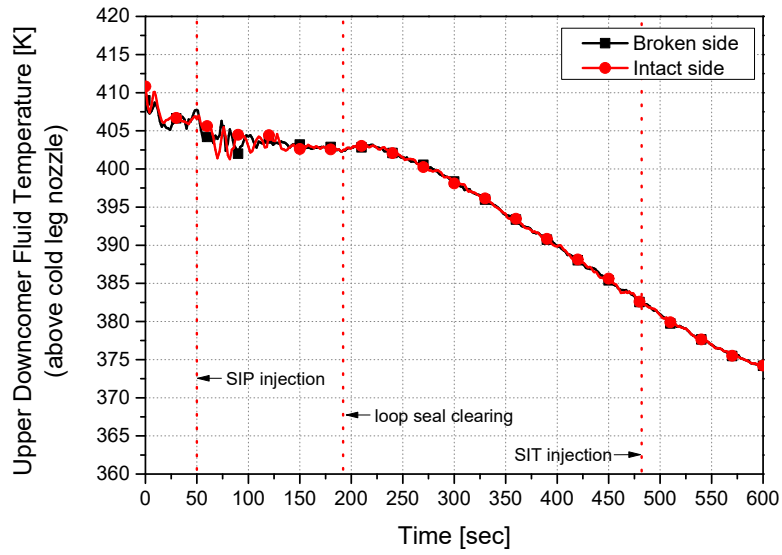


Figure 2.25 Upper downcomer fluid temperature of SNUF test

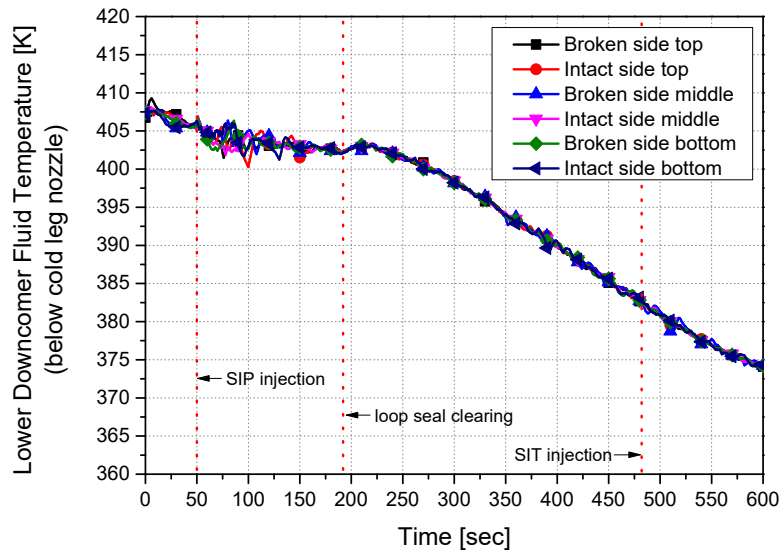


Figure 2.26 Lower downcomer fluid temperature of SNUF test

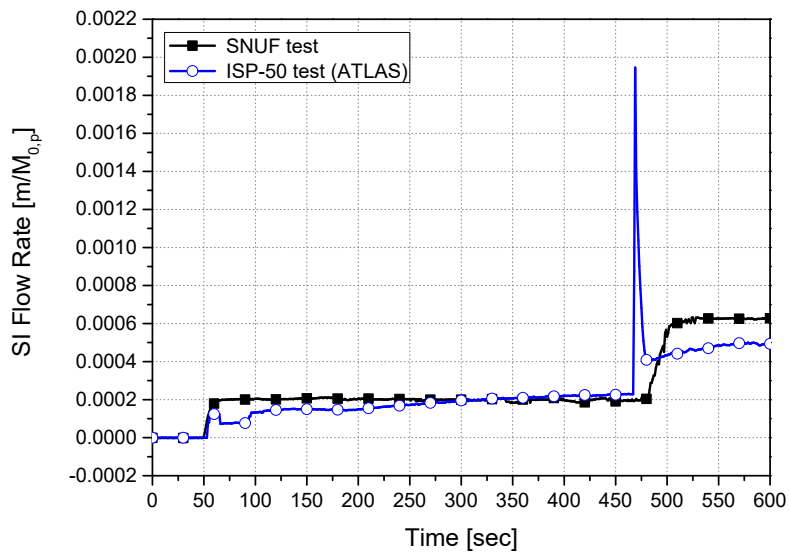


Figure 2.27 Comparison of the SI flow rate between SNUF test ATLAS tests in the normalized scale

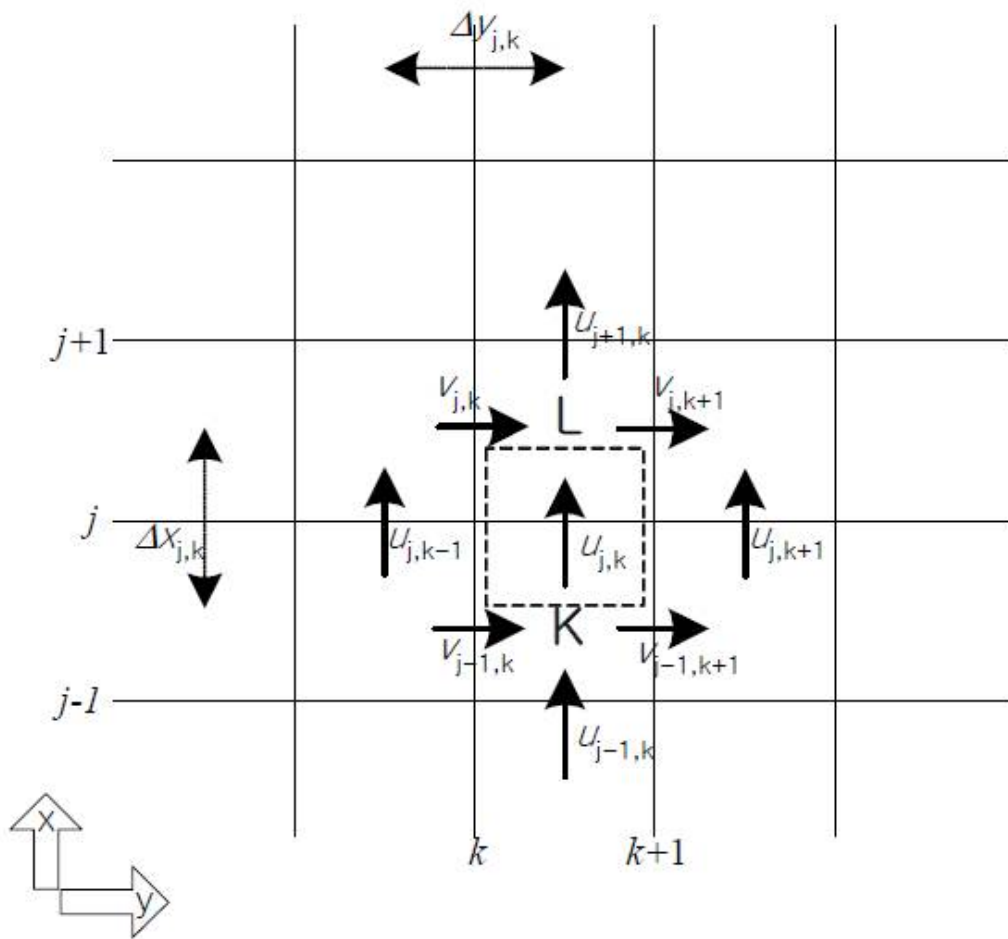


Figure 2.28 Momentum control volume for flow in the x direction in the x-y plane of the MultiD component in MARS (KAERI, 2009)



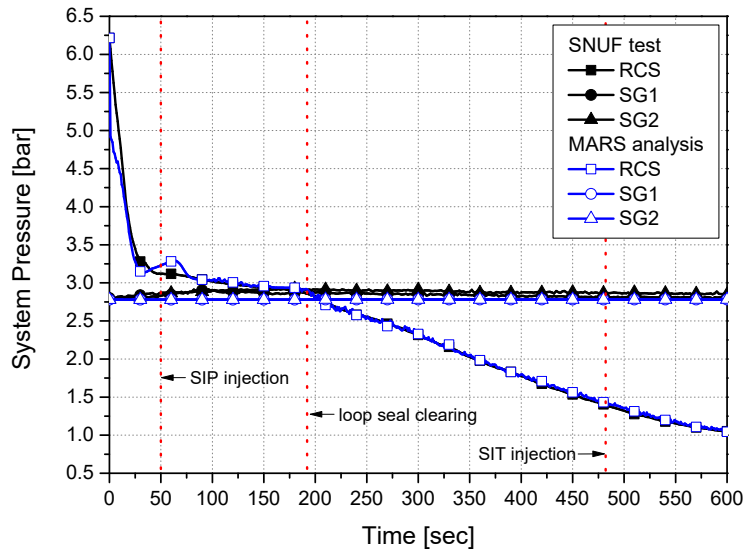


Figure 2.30 Comparison of the system pressure between SNUF test and MARS analysis

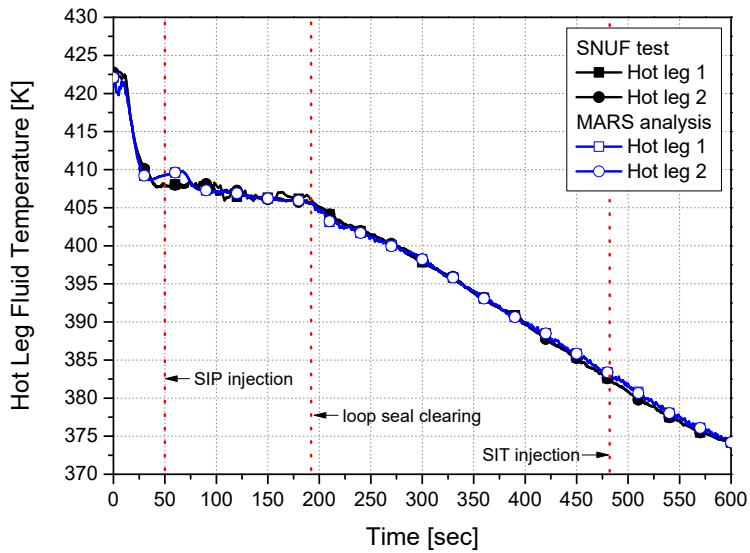


Figure 2.31 Comparison of the hot leg fluid temperature between SNUF test and MARS analysis

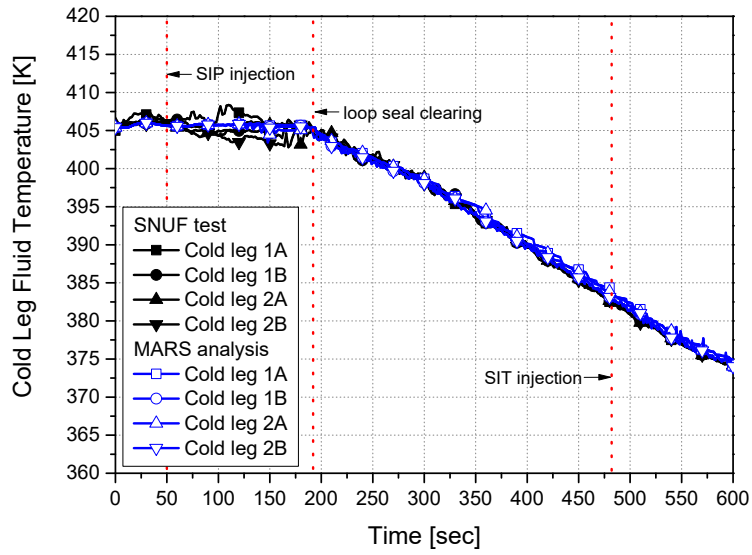


Figure 2.32 Comparison of the cold leg fluid temperature between SNUF test and MARS analysis

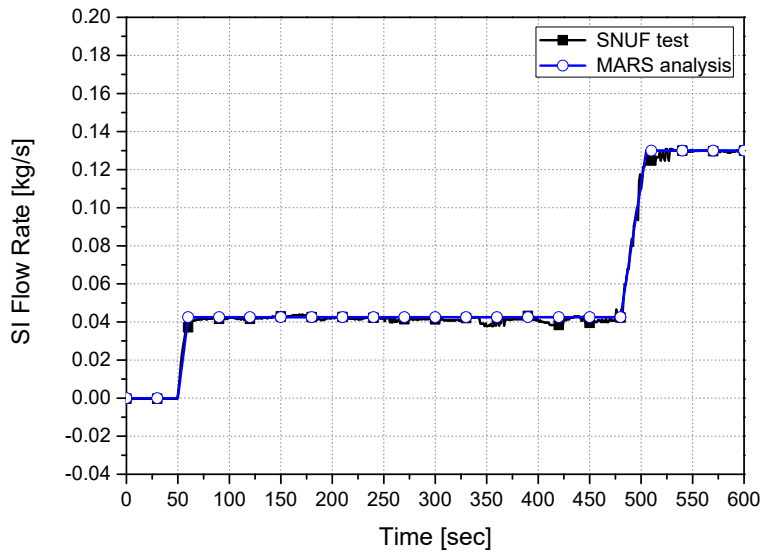


Figure 2.33 Comparison of the SI flow rate between SNUF test and MARS analysis

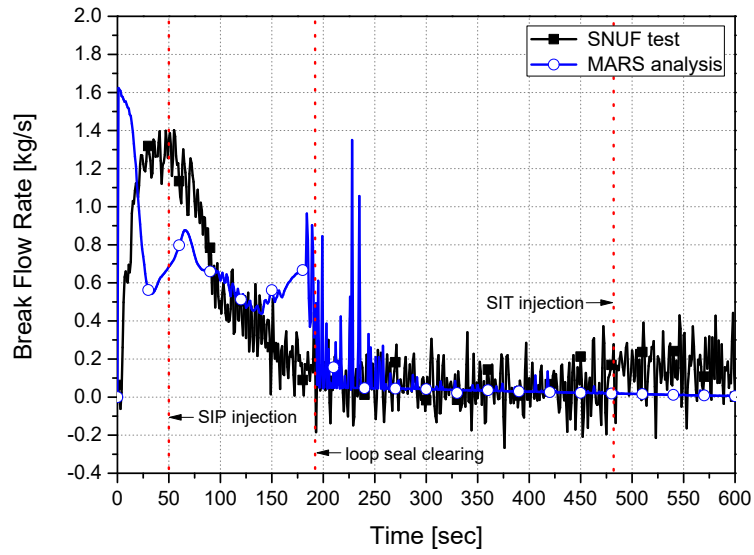


Figure 2.34 Comparison of the break flow rate between SNUF test and MARS analysis

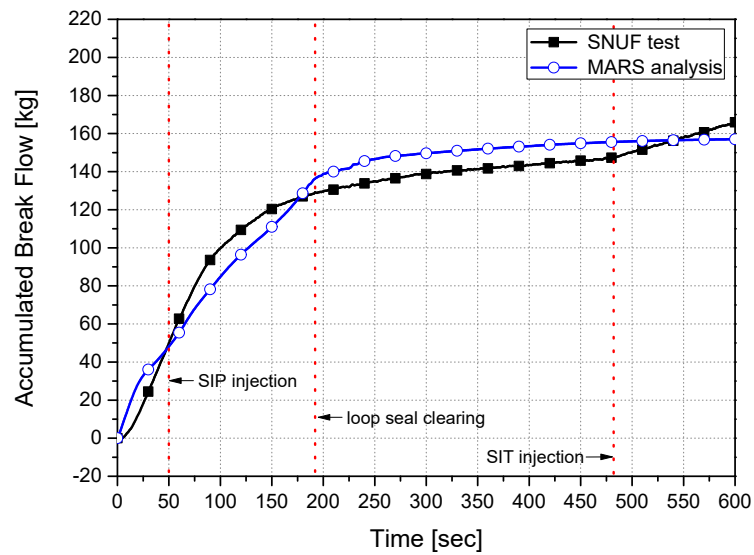


Figure 2.35 Comparison of the accumulated break flow between SNUF test and MARS analysis

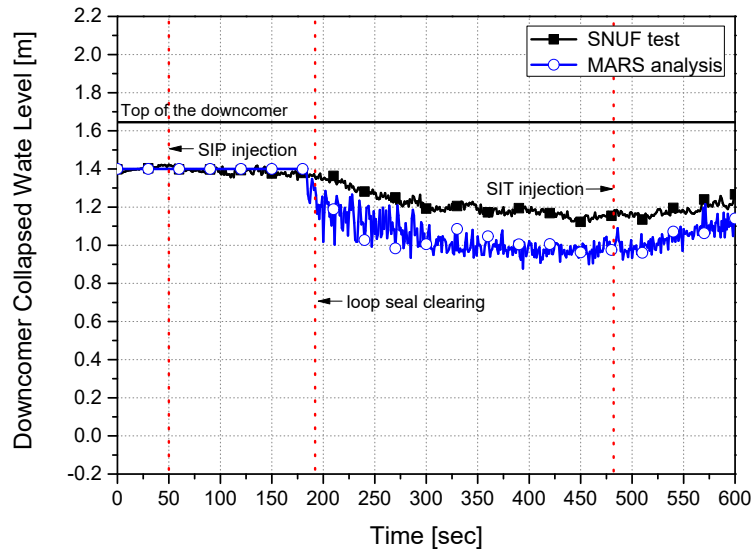


Figure 2.36 Comparison of the downcomer collapsed water level between SNUF test the MARS analysis

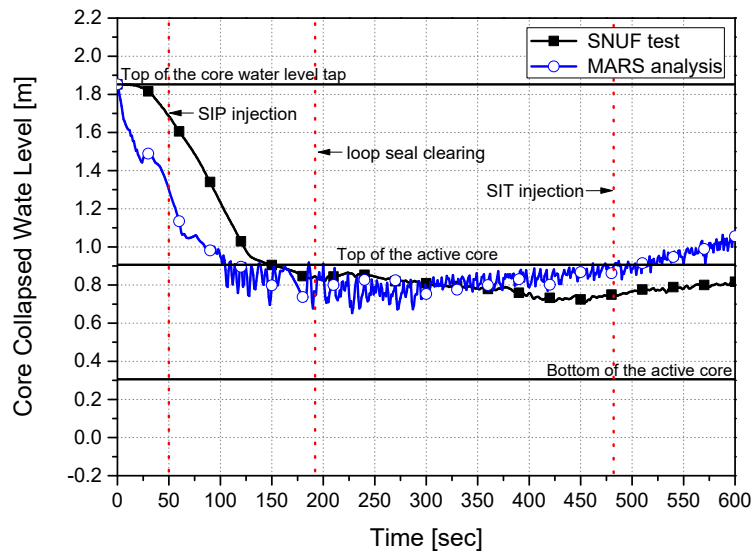


Figure 2.37 Comparison of core collapsed water level between SNUF test and MARS analysis

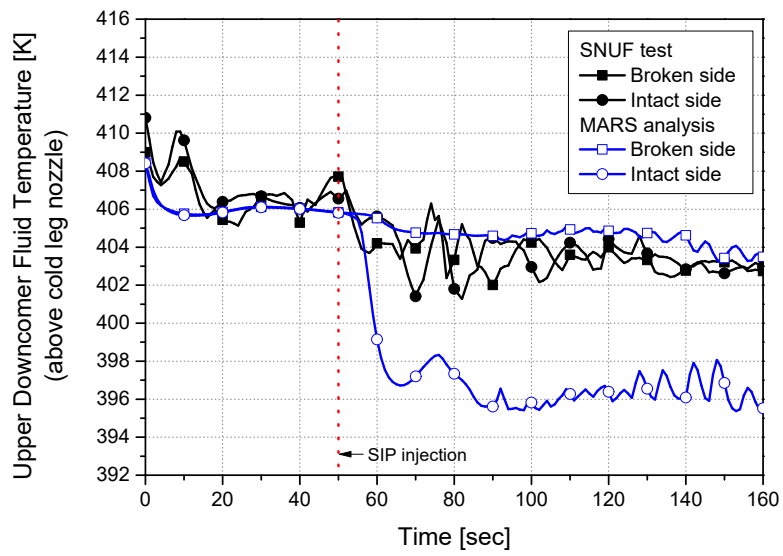


Figure 2.38 Comparison of the upper downcomer fluid temperature between SNUF test and the MARS analysis

## **Chapter 3**

# **Improvement of Thermal-Hydraulic System**

## **Code**

### **3.1 Investigation of Azimuthal Temperature Stratification**

The MARS has the capability to model the downcomer three-dimensionally with MultiD component. And it is expected that the multidimensional thermal-hydraulic phenomenon such as the ECC mixing behavior can be predicted appropriately when the three-dimensional model is utilized as described in Section 2.4.1. However, the azimuthal temperature stratification in the downcomer was also predicted according to the analysis results, even though the three-dimensional model was utilized. Therefore, it was required to investigate the cause of the limitation to predict the mixing behaviors. In this study, the cause was figured out by investigating the jet impingement phenomena and the momentum flux terms for one-dimensional connections.

#### **3.1.1 Jet Impingement Phenomenon onto a Wall**

Various studies have been carried out regarding the jet impingement

phenomenon onto wall. Among these studies, Beltaos & Rajaratnam (1974) expounded the jet impingement phenomenon by identifying regions. In geometry of the flow from a jet impinging normal to a wall as illustrated in Fig. 3.1, three main regions were identified as follows:

Region I: the free jet region, which extends from the nozzle up to certain distance from the surface and can, in turn, be divided into a potential core, a developing and a fully developed zone;

Region II: the impingement region, where the flow on the wall is accelerated by a streamwise stabilizing pressure gradient;

Region III: the wall jet region, where the pressure gradient effect no longer holds and a radially expanding flow is predominately parallel.

After incoming from the nozzle, the jet widens linearly with its length due to the exchange of momentum with the ambient fluid over the free boundaries. It means that the momentum flux of the vertical direction flow in Region I transfer to the momentum flux of parallel direction in Region III by the impingement.

The manufacturing process for the material in the industries includes a controlled quench to produce the desired grain size, so that it is required to ensure uniform properties and minimal distortion during the process. Because of this reason, it is becoming increasingly desirable to use gases, instead of liquids, as quenchants (Martin, 1977). Thus, relatively recent experimental studies to measure the flow velocity in the wall jet region developed by the impingement were carried out by using the gases as the working fluid (Baughn & Shimizu, 1989; Baughn et al., 1991; Yan et al., 1992; Yan, 1993; Cooper et al., 1993; Craft

et al., 1993; Lytle & Webb, 1994).

Even though the ambient fluid is air, the experimental studies to use liquid jet were also performed. Watson (1964) appears to have been the first to examine analytically the laminar and turbulent radial spread of a liquid jet over a flat impingement surface. A similarity solution was developed of the form;

$$u = Vf(\eta) \tag{3.1}$$

where,  $\eta = z/h(r)$

In Eq. (3.1),  $u$  is the local mean velocity in the radial direction,  $V$  is the average jet exit velocity, and  $f(\eta)$  is Watson's similarity function. In the Watson's similarity function,  $z$  is the axial coordinate measured from the impingement wall, and  $h$  is the local layer thickness in a radial coordinate measured from the stagnation point,  $r$ . According to the Watson's similarity profile, in the region  $0 < r < r_0$  (where the boundary layer reaches the free surface of the liquid jet), the velocity at the edge of the boundary layer is  $V$ , that is,  $f(\eta) = 1$ . And in the region  $r > r_0$ , the thickness of the local momentum boundary layer and the local radial flow layer is same, and the velocity decreases by following the Watson's similarity profile.

After Watson's study, various experimental studies regarding the radial layer flow field of an impinging liquid jet was carried out (Olsson & Turkdogan, 1966; Nakoryakov et al., 1978; Azuma & Hoshino, 1983; Liu & Lienhard, 1989; Thomas et al., 1990; Stevens & Webb, 1992). Among the studies, Stevens and Webb (1992) measured free surface velocity distributions from an impinging liquid jet with LDV (Laser Doppler Velocimetry), and they found that the free surface velocities of the radial layer flow would collapsed to a single band

independent of nozzle diameter and flow velocity when plotted in dimensionless coordinate:  $u/V$  vs.  $r/d$ . This band was correlated to  $\pm 20\%$  by a parabola matched with a straight line as follows:

$$\begin{aligned} \frac{u}{V} &= -0.125 \left(\frac{r}{d}\right)^2 + 0.625 \left(\frac{r}{d}\right) + 0.303 \quad \text{for } 0.5 \leq \frac{r}{d} \leq 2.86 \\ \frac{u}{V} &= -0.0936 \frac{r}{d} + 1.33 \quad \text{for } 2.86 \leq \frac{r}{d} \leq 14 \end{aligned} \quad (3.2)$$

Figure 3.2 shows the relation of  $u/V$  and  $r/d$  for Eqs. (3.1) and (3.2). As shown in this figure, the free surface velocities according to both equations decrease with increasing distance from the stagnation point. Even though the velocities decrease linearly due to the radially expanding flow, the value of the velocity is higher than half of the jet exit velocity from the nozzle until  $r/d$  is 7. That is, the fluid velocity of parallel direction on the wall developed by the vertical direction flow from the nozzle is not negligible when the impingement occurs onto a wall. Since the momentum flux terms are expressed by the square of the velocity in the system code, the magnitude of the velocity is more influential in the momentum equation. Therefore, if the jet impingement phenomenon is expected to occur in an analysis using system codes, the momentum flux terms by the radial expanding flow should be considered carefully.

### 3.1.2 Momentum Flux Terms for One-Dimensional Connections

The characteristics of three-dimensional modeling with MultiD component in MARS are described in Section 2.4.1. As described, the momentum flux terms are

implemented for the three-dimensional momentum equations in MARS. Thus, a momentum flux term of an internal junction in the MultiD component is influenced by all adjacent junctions. However, there is an exception with the junction to connect one-dimensional component to three-dimensional component.

In the case for one-dimensional component connections to three-dimensional components such as the DVI nozzles or the cold leg nozzles attached to the reactor vessel downcomer, the junction between the one-dimensional volume and the three-dimensional cell is treated like a one-dimensional junction. An example for this case is illustrated in Fig. 3.3. In this figure, the volume K is one-dimensional node and the other volumes are cells included in MultiD. Junctions 7, 8, 9, and 12 are treated as interior junctions of MultiD using free slip extrapolations at the boundary wall. And Junction 1 is treated as a normal one-dimensional junction. Junction 2 can be treated as a one-dimensional junction from node center K to cell center L. Thus, all appropriate terms such as loss and gravity are considered with the momentum equation. However, the momentum flux term from cell L is set to zero. In addition, even though all adjacent junctions (e.g. adjacent junctions of junction 3 is junctions 2, 4, 5, 6, and 7) should be considered to calculate the momentum flux of each junction, the velocity of the Junction 2 is not considered to calculate the momentum flux terms of the junctions 3, 4, 5, and 6. It is due to MARS' assumption that the axial and radial velocities influenced by Junction 2 are small in the large three-dimensional region like crossflow junction.

If the nozzles are connected to the cylindrical core vessel, which uses several rings, the momentum flux terms of the axial and radial direction can be ignored. However, if the nozzles are attached to the downcomer which has a relatively a

thin gap size, the axial and radial velocities are not small when the incoming orthogonal flow through the nozzles impinges against the downcomer wall as identified in Section 3.1.1.

Because of this assumption in MARS, the momentum equations for the interior junctions connected the cell L considers the buoyant forces dominantly when the jet impingement phenomenon occurs. Thus, the cold water injected into the downcomer annulus flows in the direction of gravity so that the azimuthal temperature stratification was predicted in the code analysis unlike the test results. Because of this reason, it is required to consider the momentum flux terms induced by the impinging flow, and for that, an appropriate jet impingement model to apply to the system code, MARS, should be developed.

## **3.2 Development of Jet Impingement Model**

The need to develop a jet impingement model to employ the thermal hydraulic system code was highlighted by investigating the jet impingement phenomenon onto a wall, and the treatment of the momentum flux terms for one-dimensional connection in Section 3.1. As in Eq. (3.2), a correlation based on the experimental data regarding the free surface velocity distributions was suggested by Stevens and Webb (1992). However, in accordance with their additional study (Stevens & Webb, 1993), the measurements from the interior of the radial flow layer showed that the maximum velocity in the layer was not at the free surface. It means that the mean velocity of the radial flow layer is not correlated by Eq. (3.2). And these experimental studies were carried out in conditions to maintain sufficient nozzle-

to-wall spacing, which is at least one nozzle diameter. Thus, the results of these studies cannot be applicable to the geometry of the reactor downcomer to have a small gap size between inside and outside wall of the downcomer compared to the diameter of the cold leg nozzle. Because of these limitations shown in the available studies, an analytical method to use CFD calculations in various conditions was selected to develop the jet impingement model for the system code, MARS.

### **3.2.1 CFD Model Validation with Available Experimental Data**

#### **CFD Models for Validation**

Initial investigation was carried out to select an appropriate numerical model based on the prediction capability to published represent experimental data of a round jet impinging on a wall. This would provide a basis for numerical model selection and CFD model validation. To develop a jet impingement model for the system code, the wall-parallel velocity profiles at various radial positions should be calculated by the CFD software correctly. Thus, a published experimental data produced by Cooper et al. (1993) was selected to correspond to this particular case as the representative test. The results of this test were utilized in several studies (Behnia et al., 1998; Esch et al., 2003; Zuckerman & Lior, 2005) to validate their numerical models.

The CFD model to predict the representative test data was constructed using structured hexagonal grids and used the three-dimensional solver as shown in Fig. 3.4. The generalized cylinder mesher was utilized for the downcomer and the nozzle parts. And the prism layer mesher with 20 layers was applied to a half of

the downcomer part where the radially expanding flow was expected. The impingement wall and fluid domain were modelled out to a radius of twenty (20) injection nozzle diameter ( $r=20d$ ). The domain extended upwards to the height of the nozzle, as shown in Fig. 3.5, which also shows the various boundaries as well as the boundary type used at each surface.

In the experiment, working fluid was taken to be air, and was assumed to be at a constant density,  $\rho$ , and thermal conductivity,  $k_c$ . Ambient pressure was set at 1 bar and fluid temperature was set at 293 K. The inflow at the start of the injection nozzle was set at a constant velocity and temperature of 293 K and allowed to develop. With a very long injection nozzle ( $L_{nozzle}=100d$ ), the solution was found to be insensitive to the nozzle inlet turbulence boundary conditions. The impinging wall and nozzle wall were modelled as nonslip surfaces.

Steady solution was performed using a segregated solver. The number of cells was set at 234000. Using four (4) hosts, each having twenty (20) 2.20 GHz Pentium Xeon processor running in parallel with Linux 2.6 and 64 GB of RAM, typical computation time was approximately one (1) hour. The CFD software used was STAR-CCM+. Grid generation was performed using the interior generator of the STAR-CCM+.

### **Selection of Turbulence Model**

An investigation of the prediction capability according to turbulence models was carried out to select a modeling approach for the jet impingement phenomenon. Behnia et al. (1998) carried out a numerical study to predict heat transfer in an axisymmetric turbulent jet impinging on a flat plate. In this study they used the experimental data generated by Cooper et al. (1993) which made

velocity measurements at various radial locations. A comparison of the measured velocity magnitude and their computation using the  $k-\varepsilon$  turbulence model and V2F turbulence model (Durbin, 1995) at four (4) different radial locations are presented as shown in Fig. 3.6. According to the prediction results, near the stagnation streamline ( $r/d=0.0$  and  $r/d=0.5$ ) there exists little difference between the two predictions and quite a good agreement with the experimental data. However, in the wall jet region ( $r/d=1.0$ ) and the radial location ( $r/d=2.5$ ), the V2F model correctly predicts the flow acceleration; there is an excellent agreement with the data. At this location, which is of interest in this study, the  $k-\varepsilon$  model predicts low velocities in the wall region and high velocities in the outer region. That is, the  $k-\varepsilon$  model does not correctly resolve the development of the boundary layer, leading to under-prediction of the velocity in the wall region and over-prediction in the outer region.

The similar approach with Behnia et al. (1998) was performed by Zuckerman and Lior (2005) utilizing the CFD software, Fluent 6. They investigated various turbulence models to select an appropriate model for the jet impingement phenomenon. Excluding the models requiring very lengthy computation times such as LES (Large Eddy Simulation), DNS (Direct Numerical Simulation), and other unsteady models, the following eight turbulence models based on RANS (Reynolds Averaged Navier-Stokes) were evaluated and the results were compared with the test data set:

- 1) Realizable  $k-\varepsilon$  with standard wall functions,
- 2) Realizable  $k-\varepsilon$  with nonequilibrium wall functions,
- 3) Realizable  $k-\varepsilon$  with enhanced wall functions,

- 4) RSM (Reynolds Stress Model) with wall reflection effect and standard wall functions,
- 5) RSM with wall reflection effect and enhanced wall functions,
- 6) SST (Shear Stress Transport)
- 7) Standard  $k-\varepsilon$
- 8) V2F.

The evaluation results carried out by Zuckerman and Lior (2005) showed a similar conclusion with the study of Behnia et al. (1998). At  $r/d=1$ , the V2F model provides the best prediction of velocity as presented in Fig. 3.7. At  $r/d=2.5$ , the SST and V2F models provided velocity profiles with similar levels of fidelity as shown in Fig. 3.8.

As described above, it was expected that the V2F turbulence model predicted the jet impingement phenomena better in accordance with the previous studies. Thus, the base turbulence model to develop the jet impingement model for the system code was determined as the V2F model.

### **Validation Results**

To validate the prediction capability of the CFD model, the wall-parallel velocity profile at the radial location ( $r/d=2.5$ ) was analyzed by utilizing the CFD software, STAR-CCM+. Even though the V2F turbulence model is widely known for well-behaved prediction of the jet impingement behavior, the calculation to use the realizable  $k-\varepsilon$  model was also carried out for the comparison of the prediction capability of the turbulence models. Figure 3.9 shows the analysis results with the V2F and realizable  $k-\varepsilon$  model. As shown in this figure, the V2F

model correctly predicted the experimental data (Cooper et al., 1993), and there was an excellent agreement with the data near the wall as well as in the outer region. At this radial location, the realizable  $k$ - $\varepsilon$  model predicted low velocities in the wall region and high velocities in the outer region. This validation result is consistent with the previous studies.

The validation results provided the suitability of the CFD model and the turbulence model to be utilized for the calculations with various conditions to develop the jet impingement model for the system code.

### **3.2.2 Modeling of the Jet Impingement**

#### **Parametric Sensitivity Analyses**

The wall-parallel velocity profiles at various radial positions were analyzed by utilizing the CFD model described in Section 3.2.1. To consider the various conditions in the reactor downcomer, the geometry of the CFD model and the boundary conditions such as the injection fluid velocity and properties should be varied. In this study, the conditions were varied for sensitivity calculations as follows:

- 1) inlet nozzle diameter,  $d$ , is from 0.03 m to 0.10 m by 0.01 m,
- 2) nozzle to wall spacing,  $t$ , is from 0.015 m to 0.050 m by 0.005 m,
- 3) nozzle inlet velocity,  $V$ , is from 0.3 m/s to 0.7 m/s by 0.1 m/s,
- 4) inlet and ambient fluid pressure,  $P$ , is 3 bar and 80 bar,
- 5) inlet and ambient fluid temperature,  $T$ , is 325 K (at  $P=3$  and 80 bar) and 550 K (at  $P=80$  bar).

By using the wall-parallel velocity profiles at a radial position, which were analyzed by the CFD model, the local momentum boundary layer thickness,  $h$  (refer to Fig. 3.10), was calculated. The local momentum boundary layer thickness was defined by integrating the calculated wall-parallel velocities in the  $z$ -direction until the integral continuity for the axisymmetric configuration was satisfied for the given  $r$ -location:

$$\frac{V\pi d^2}{4} = 2\pi r \int_0^h u(z) dz \quad (3.3)$$

As illustrated in Fig. 3.11, if  $h$  satisfying Eq. (3.3) was to be found, then  $u_h$  could be defined as follows:

$$\frac{V\pi d^2}{4} = 2\pi r \int_0^h u(z) dz = 2\pi r h u_h \quad (3.4)$$

Equation (3.4) means that the integrated value of the velocity,  $u(z)$ , from  $z = 0$  to  $z = h$  is the same in the area of box ( $h \times u_h$ ) in Fig. 3.11. To simplify the problem, it was assumed that the wall-parallel velocity between  $z = 0$  and  $z = h$  was  $u_h$  and the velocity between  $z = h$  to  $z = t$  was zero. From this assumption, the integral means of the square of the wall-parallel velocity can be defined as follows:

$$\frac{\int_0^h (u_h)^2 dz + \int_h^t 0^2 dt}{t} = \frac{h(u_h)^2}{t} \equiv u_m^2 \quad (3.5)$$

By combining Eqs. (3.4) and (3.5),  $u_m^2$  can be expressed as:

$$u_m^2 = \frac{h(u_h)^2}{t} = \frac{h}{t} \left( \frac{V\pi d^2}{4 \cdot 2\pi r h} \right)^2 = \frac{h}{t} \left( \frac{Vd^2}{8rh} \right)^2 = \frac{V^2 d^4}{64r^2 t h} \quad (3.6)$$

Therefore, if the local momentum boundary layer thickness,  $h$ , for a given location  $r$  was correlated, then  $u_m^2$  could be determined with Eq. (3.6).

Figure 3.12 shows the results of the sensitivity calculation with various inlet nozzle diameters. The non-dimensional thickness,  $h/t$ , is illustrated according to the radial positions. At first, it could be found that the momentum boundary layer thickness had the second order polynomial shape. It means that a minimum value of the momentum boundary layer thickness may exist at a specific radial position. And the minimum momentum boundary layer thickness increased with the increase of the inlet nozzle diameter,  $d$ . Additionally, the radial position, which had the minimum momentum boundary layer thickness, became far from the stagnation point with the increase of the inlet nozzle diameter.

The relations between the non-dimensional thickness,  $h/t$ , and the radial position are illustrated in Fig. 3.13. From this figure, it could be found that the non-dimensional thickness regarding the momentum boundary layer thickness decreased with the nozzle to wall spacing,  $t$ . However, the dimensional value of the minimum momentum boundary layer thickness increased slightly as increasing the nozzle to wall spacing as shown in Fig. 3.14. And the radial position which had the minimum momentum boundary layer thickness became far from the stagnation point with the increase of the nozzle to wall spacing. In addition, the increasing or decreasing rate of the momentum boundary layer

thickness was influenced by the nozzle to wall spacing.

And the parametric sensitivity calculations of the fluid boundary conditions were carried out as illustrated in Figs. 3.15 and 3.16. At first, the nozzle inlet velocity,  $V$ , did not strongly influence to the momentum boundary layer thickness compared to the inlet nozzle diameter and the nozzle to wall spacing as shown in Fig. 3.15. Also, from Fig. 3.16, it could be found that there was no effect caused by the difference of the fluid properties. These results means that Reynolds number,  $Re$ , the ratio of inertial forces to viscous forces, does not influence significantly the flow pattern caused by the jet impingement phenomena when the geometric information is same. This results has a consistency with Eq. (3.2) suggested by Stevens and Webb (1992).

### **Formularization of Momentum Boundary Layer Thickness**

As described in previous part of this section, the local momentum boundary layer thickness,  $h$ , at a radial position,  $r$ , was related to the inlet nozzle diameter,  $d$ , and the nozzle to wall spacing,  $t$ . And the relation between the momentum boundary layer thickness and the radial position could be formulated with the second order polynomial shape as follows:

$$\frac{h}{t} = A(r - B)^2 + C \quad (3.7)$$

where,  $A$  is the increasing or decreasing rate of the momentum boundary layer thickness,  $B$  is the radial position which has the minimum momentum boundary layer thickness,  $C$  is the minimum momentum boundary layer thickness. In accordance with the relation of each parameter,  $A$  was inversely proportional to  $t$ ,

$B$  was in proportion to  $d$  and  $t$ , and  $C$  was in proportion to  $d$  and in inverse proportion to  $t$ . Thus, Eq. (3.7) could be re-written non-dimensionally with the various constants ( $\alpha$ ,  $\beta$ ,  $\gamma$ ,  $\delta$ , and  $\varepsilon$ ) as the following:

$$\frac{h}{t} = \frac{\alpha}{t^2} (r - \beta d^\gamma t^{(1-\gamma)})^2 + \delta \left(\frac{d}{t}\right)^\varepsilon \quad (3.8)$$

Each constant in Eq. (3.8) was determined by using the second order polynomial fitting of the CFD calculation:

$$\frac{h}{t} = 0.027 \left\{ \frac{r}{t} - 3.5 \left(\frac{d}{t}\right)^{0.34} \right\}^2 + 0.095 \left(\frac{d}{t}\right)^{0.82} \quad (3.9)$$

Then, the local momentum boundary layer thickness,  $h$ , could be correlated by following equation:

$$h = \frac{0.027}{t} (r - 3.5d^{0.34}t^{0.66})^2 + 0.095d^{0.82}t^{0.18} \quad (3.10)$$

A comparison of the local momentum boundary layer thickness between the correlation Eq. (3.10) and the data set of the CFD calculation is shown in Fig. 3.17, in which the diagonal line represents a perfect fit between the data points and the correlation equation. The error band was correlated to  $\pm 25\%$  by a parabola matched with straight lines.

Since the geometry of the CFD model for CFD calculations was determined based on the test facility, SNUF and ATLAS, it was required to check the scale-up

capability of Eq. (3.10) for the jet impingement model. Thus, additional CFD calculations were carried out with the conditions for the prototype, APR1400. In these calculation, the nozzle to wall spacing,  $t$ , was determined as the gap size of the downcomer of the APR1400, 0.25 m. And the inlet nozzle diameter was determined as 0.2 m and 1.0 m based on the inner diameter of the DVI nozzle and the cold leg nozzle. The velocity of the incoming flow was determined as 3.0 m/s, 5.0 m/s, and 10.0 m/s based on the cold leg flow rate of the DVI line break accident and the SLB accident in the APR1400. The additional CFD calculation results were compared to the correlation as illustrated in Figs. 3.18 and 3.19. From these figures, it could be found that Eq. (3.10) was appropriately applicable to the prototype as well as the test facility.

By combining Eqs. (3.6) and (3.10),  $u_m^2$  could be expressed as:

$$u_m^2 = \frac{V^2 d^4}{64r^2 [0.027(r - 3.5d^{0.34}t^{0.66})^2 + 0.095d^{0.82}t^{1.18}]} \quad (3.11)$$

Then, this equation could be applied to the momentum flux terms induced by the impinging flow due to the incoming orthogonal flow through the nozzles. That is, the momentum flux terms of junctions 3, 4, 5, and 6 in Fig. 3.3 are calculated based on Eq. (3.11) in the system code, MARS.

### **Application Criteria of Jet Impingement Model**

The correlation presented in previous part of this section could be applied to the system code in order to consider the momentum flux terms induced by the impinging flow. However, if the velocity of incoming flow is too small, then the

wall-parallel velocity at the radial location also has a small value. Thus, the influence of the jet impingement phenomenon is a negligible quantity in this case. In addition, the inlet nozzle diameter and the gap size of the downcomer could also influence the impinging flow. According to Eq. (3.10), if the inlet nozzle diameter,  $d$ , or the nozzle to wall spacing,  $t$ , becomes large, then the minimum momentum boundary layer thickness could reach to a similar value with the nozzle to wall spacing (the gap size of the downcomer in the reactor). In this situation, the fluid velocity in the radial location should be determined by the mass conservation between the incoming flow and the radial outlet flow not by the characteristic of the impinging flow. Therefore, it was required to define the criteria whether to apply the jet impingement model or not.

In this study, the application criteria of jet impingement model were determined based on the ROCOM buoyance mixing tests (Rohde et al., 2005). These tests were carried out to investigate the influence of density effects. It was expected that the density difference could be neglected, if the flow rates were sufficiently high, meaning if mixing was momentum controlled. The objective of these tests was to find the conditions for transition from momentum controlled mixing to buoyance drive mixing. To separate the density effects from the influence of other parameters, a constant flow in the loop with the ECC injection nozzle was assumed in the ROCOM tests. The mass flow rate was varied in the different experiments between 0 and 15% of the nominal flow rate. The density difference between ECC and loop water was varied between 0 and 10%. Twenty (20) test cases with various flow rate and density difference conditions were carried out at ROCOM.

Based on observations, the test cases were divided into three groups as shown

in Fig. 3.20: density dominated flow ( $\diamond$ ), momentum dominated flow ( $\Delta$ ) and the transition region ( $*$ ). The conditions at the inlet into the downcomer were used to calculate Froude number of each test according to Eq. (1.1). Lines of constant Froude numbers are presented in Fig. 3.20. All experiments, identified as density dominated were located in the region left of the isoline  $Fr = 0.85$  and all momentum dominated points were found right of the isoline  $Fr = 1.50$ .

The criterion of the flow distribution for the ROCOM tests could be identified by the visualization of the time-dependent tracer distribution at the sensors in the downcomer (refer to Fig. 3.21) as presented in Fig. 3.22. In the tests located in the region right of the isoline  $Fr = 1.50$ , the flow entering the downcomer was divided into two streams flowing right and left in a downwards directed helix around the core barrel. Such a flow distribution was defined as the momentum dominated flow in the ROCOM tests. In the tests located in the region left of the isoline  $Fr = 0.85$ , the ECC water covered a smaller azimuthal sector. The density difference partly suppressed the propagation of the ECC water in horizontal direction. This flow distribution was defined as the density dominated flow in the ROCOM tests. In terms of describing the mixing behavior in the downcomer, the above criterion of the flow distribution was reasonable. However, when dividing the ROCOM test cases whether the jet impingement phenomenon occurs or not, it is required to consider other criteria.

Figure 3.23 presents two (2) tests among the all ROCOM tests. The first one is 5% of the nominal mass flow rate and 10% of the nominal density difference (refer to Fig. 3.23 (a)). The second one is 10% mass flow rate and 10% density difference (refer to Fig. 3.23 (b)). In the case of the first one, the ECC water covered a much smaller azimuthal sector. And the ECC water fell down to gravity

direction in an almost straight stream-line and reached the lower downcomer sensor directly below the affected inlet nozzle. This case appeared that the jet impingement phenomenon did not occur. On the other hand, in the second case, the propagation of the ECC water in horizontal direction was observed. This case indicated that the jet impingement phenomenon occurs. Therefore, in terms of describing the jet impingement phenomenon, these two (2) tests could be used to determine the application criteria of the jet impingement model.

The Froude number calculated by Eq. (1.1) for above two (2) tests was 0.336 and 0.772, respectively. One of the parameter of Eq. (1.1) is the height of the downcomer,  $s$ . For identification of the overall mixing behavior in the downcomer, this parameter could be used to calculate the Froude number. However, the jet impingement is a local phenomenon in the downcomer. Therefore, the definition of the Froude number to include the height of the downcomer was not appropriate to identify the jet impingement phenomenon. Thus, in this study, a new formula to define the Froude number was suggested as follows:

$$Fr_{impingement} = \frac{V}{[gh_n(\rho_n - \rho_a)/\rho_a]^{1/2}} \quad (3.12)$$

where,  $h_n = d^{0.82} t^{0.18}$

In Eq. (3.12),  $h_n$  is the normalized minimum local momentum boundary layer thickness. And this formula means that the jet impingement phenomenon occurs well when the velocity of the incoming flow is high, the local momentum boundary layer is small, and the density difference is small. Table 3.1 presents the Froude number of two (2) ROCOM tests to be used to determine the application criteria of jet impingement model. The Froude number of the test showing the

gravity direction flow was 1.220 and the Froude number of the test showing the jet impinging flow was 2.573. Thus, the application criteria of the jet impingement model were determined with the adjacent Froude numbers for impinging, which are 1.3 and 2.5. That is, in MARS, the momentum flux terms induced by the imping flow due to the incoming orthogonal flow through the nozzles are calculated by Eq. (3.11) when the Froude number for impinging is larger than 2.5. If the Froude number for impinging is less than 1.3, then the jet impingement model is not applied in MARS. When the Froude number for impinging is between 1.3 and 2.5, the momentum flux terms calculated by Eq. (3.11) is applied with linear interpolation.

The detailed description to apply the jet impingement model into MARS is presented in Appendix A.

### **3.3 Validation of Jet Impingement Model**

The jet impingement model was developed to predict mixing behavior in the downcomer well, and applied to MARS. To validate of the jet impingement model, the test results from SNUF and ATLAS were used. These validation works sought to confirm the predictive capability of the multidimensional mixing between the hot water in the downcomer and the cold ECC water through the DVI nozzle. Since the jet impingement model could be applied to the inlet coolant with the asymmetric temperature during a transient such as the SLB accident, the test data of the ROCOM was also used to validate the modified MARS and the jet impingement model.

### 3.3.1 Validation with SNUF Test

The SNUF test was analyzed with the modified MARS and SNUF MARS modelling described in Section 2.4.2. Figure 3.24 shows the upper downcomer fluid temperature of the test result and the analyses results with the original MARS and the modified MARS. As described in Section 2.4.3, the temperature difference in the azimuthal direction (between the broken side and intact side) of the downcomer was not observed in the test. However, the fluid temperature of the intact side was lower around 10 K than that of the broken side according to the analysis result with the original MARS. It means that the azimuthal temperature stratification was predicted by the original MARS. However, when calculating the upper downcomer fluid temperature with the modified MARS, the difference of the fluid temperature between the broken side and intact side was around 4 K. Since the intact side fluid temperature analyzed with MARS was the average temperature of the node to inject cold water, the intact side fluid temperature of the analysis was not perfectly same with that of the test. However, it was revealed that the tendency of the azimuthal temperature stratification decreased by applying the jet impingement model.

As shown in Figs. 3.25, 3.26, 3.27, and 3.28, the overall behavior, such as the system pressure, the break flow rate, and the core and downcomer collapsed water level during the DVI line break accident was similar in the analysis results between the original MARS and modified MARS. It means that the jet impingement model strongly influenced in the mixing behavior in the downcomer, but did not affect to the overall phenomenon in the reactor.

### **3.3.2 Validation with the ATLAS Test**

The ATLAS test was analyzed with the original and modified MARS to estimate the influence of the jet impingement model. The MARS modeling for the ATLAS system was revised based on the one-dimensional modeling, which was used in First ATLAS Domestic Standard Problem (DSP-01) (Kim et al., 2011). In this modeling, the downcomer was modelled by the MultiD component, and was divided into six (6) regions in the azimuthal direction. Along the vertical direction, the downcomer had ten (10) nodes as shown in Fig. 3.29. The test results are presented in Fig. 1.2 and the analyses results with the original and modified MARS are presented in Figs. 3.30 and 3.31, respectively.

In the ATLAS test, the downcomer annulus was full of hot water, almost saturation temperature, at the time of SIP injection, and it was observed that the cold ECC water was well mixed with the hot inventory as shown in Fig. 1.2. However, this vigorous mixing was not predicted appropriately by the original MARS code as illustrated in Fig. 3.30. The fluid temperature of the injection DVI side annulus was much lower than that of the broken side annulus without applying the jet impingement model. However, when calculating the downcomer fluid temperature with the modified MARS code, the difference of the fluid temperature between the broken DVI side and injection DVI side decreased as shown in Fig. 3.31. And the temperature distribution in the azimuthal direction became to gradual tendency. Since the injection DVI side fluid temperature analyzed with MARS was the average temperature of the node to inject cold water, the injection DVI side fluid temperature of the analysis was not perfectly same

with that of the test. However, it was revealed that the tendency of the azimuthal temperature stratification decreased by applying the jet impingement model.

The influence of the jet impingement model could be also found by comparing the contour map of the downcomer fluid temperature. As shown in Fig. 3.32, the fluid temperature in the lower downcomer in the test was around 566 K (yellow). On the other hand, the lower downcomer fluid temperature estimated by the original MARS was lower than that of the test, is round 563 K (green) as illustrated in Fig. 3.33. This difference of the fluid temperature in the downcomer was caused by the difference of the ECC water bypass ratio to the broken DVI nozzle. In the test, the ECC water injected into the DVI nozzle was well mixed in the upper downcomer region without the azimuthal temperature stratification, so that the ECC water bypass ratio to the broken DVI nozzle was relatively high. However, in the analysis with the original MARS code, the main flow direction of the injected ECC water was downwards. Thus, the bypass ratio to the broken DVI nozzle was small compared to the test so that the overall downcomer fluid temperature was low. That is, the mixing phenomenon in the downcomer was not predicted well with the original MARS code. When calculating the downcomer fluid temperature with the modified MARS code, the overall fluid temperature showed similar value with the test, around 566 K (yellow), as shown in Fig. 3.34. Therefore, it was revealed that the jet impingement model was required to predict the mixing behavior in the downcomer during the DVI line break accident reasonably.

As shown in Figs. 3.35, 3.36, 3.37, and 3.38, the overall behavior, such as the system pressure, the break flow rate, and the core and downcomer collapsed water level during the DVI line break accident was similar in the analysis results

between the original MARS and modified MARS. It means that the jet impingement model strongly influenced in the mixing behavior in the downcomer, but did not affect to the overall phenomenon in the reactor.

### **3.3.3 Validation with the ROCOM Test**

Experimental data on non-uniform flows in the downcomer such as the flow that might occur in an SLB accident has been produced at the ROCOM test facility. Among the ROCOM tests, the ROCOM test 2.2 (Kliem & Franz, 2012) was utilized to validate the jet impingement model in this study. The ROCOM test 2.2 was performed under transient conditions. The initial conditions of the test are summarized in Table 3.2. The experiment was carried out so that the equal flow rates were first established in loop 2 through 4, and then, at time instant zero, injection was started in loop 1 and at the same time the decrease of flow rates in the other loops was commenced. The measured loop flow rates during the experiment are presented in Figure 3.39.

The MARS model of the ROCOM test facility used in this study prepared by Lee and Chung (2012) consists of the reactor pressure vessel starting from the cold legs up until the beginning of the hot legs. The pressure vessel was modelled using MultiD component. The schematic nodalization of the MARS model for the ROCOM test facility is illustrated in Figure 3.40. In this modeling, the vessel was divided into six (6) regions in the radial direction and eight (8) regions in the azimuthal direction. Along the vertical direction, the vessel had twelve (12) nodes.

Sugar and salt were used to alter the density and electric conductivity of fluid injected to a specified cold leg, so that the mixing in the ROCOM test facility

could be measured by means of electric conductivity sensors. The measurements obtained from the test facility were described by a dimensionless mixing scalar, which characterizes the local instantaneous share of fluid originating from the specified cold leg. The mixing scalar  $\Theta_{x,y,z}(t)$  is calculated by relating the local instantaneous conductivity  $\sigma_{x,y,z}(t)$  to the amplitude of the conductivity change at a reference point ( $\sigma_l$ ) according the following formula:

$$\Theta_{x,y,z}(t) = \frac{\sigma_{x,y,z}(t) - \sigma_0}{\sigma_1 - \sigma_0} \quad (3.13)$$

The corresponding temperature distribution could be reproduced from mixing scalar using weighted interpolation between the average temperature of the intact coolant loops  $T_{2-4}$  and the temperature of the broken loop  $T_1$ :

$$T_{x,y,z} = \Theta_{x,y,z}(T_1 - T_{2-4}) + T_{2-4} \quad (3.14)$$

Because MARS does not contain fluid material properties for the sugar/water solution used in the real test, the simulation was carried out in thermodynamic conditions rather than the atmospheric conditions of the ROCOM test. This means that the geometry and flow rates were taken from the actual ROCOM test, but the pressure was considerably higher than the pressure at the ROCOM facility. In this study, the pressure for the analyses was assumed to be 3.8 MPa. And the density differences were achieved through heating of the fluid rather than through altering its chemical composition. Based on above method, the temperature of each loop was determined as shown in Table 3.2. And the time dependent inflow velocities

which were used as inflow boundary conditions for the analyses were determined based on the measured flow rates as presented in Fig. 3.41.

Snapshots of the temperature distributions in the downcomer at time instances of 30, 60, 90, 120, and 150 seconds are presented in Figs. 3.42, 3.43, 3.44, 3.45, and 3.46, respectively. First temperature distribution in each figure is the ROCOM test result, and second and third temperature distributions are the analyses results with the original MARS and the modified MARS. Since the density difference between the incoming fluid through the broken loop and the ambient fluid in the downcomer was large before 90 seconds, the Froude number defined by Eq. (3.12) is a small value, around 1.0. As described in Section 3.2.2, the jet impingement model was not applied with the Froude number which is smaller than 1.3. Thus, the analyses results with the original MARS and the modified MARS showed similar tendency as presented in Figs. 3.42, 3.43, and 3.44. And it could be found that the both MARS codes were able to predict reasonably the temperature distribution before 90 seconds.

By filling of the downcomer with cold water, the density difference between the incoming fluid through the broken loop and the ambient fluid in the downcomer decreased so that the Froude number started to increase after 100 seconds and became around 2.5 at 150 seconds. And the jet impingement model was applied in the analysis with the modified MARS code after the Froude number became larger value than 1.3. Thus, the temperature distributions analyzed by the modified MARS showed a different tendency with that by the original MARS as presented in Figs. 3.45 and 3.46. When analyzing with the original MARS, the ECC water fell down to the direction of gravity in an almost straight stream-line and reached the lower downcomer and the intact side fluid in

the downcomer was hotter than the broken side fluid. That is, the azimuthal temperature stratification was predicted in the original MARS code. However, the degree of stratification has decreased by applying the jet impingement model with the modified MARS, and this tendency was similar with the test results as shown in Figs. 3.45 and 3.46.

By validating with the ROCOM test, it was revealed that the jet impingement model could be applied to simulate the mixing phenomenon during a transient such as the SLB accident as well as the DVI line break accident.

Table 3.1 Comparison of Froude number between Eqs. (1.1) and (3.12) for the ROCOM buoyance mixing tests

<b>Flow type</b>	$Fr_{ROCOM}^{1)}$	$Fr_{impingement}^{2)}$	<b>Application criteria of jet impingement model</b>
Gravity direction flow	< 0.336	< 1.220	$Fr_{impingement} < 1.3$ : no application
Transition region			$1.3 < Fr_{impingement} < 2.5$ : linear interpolation
Jet impinging flow	> 0.772	> 2.573	$Fr_{impingement} < 2.5$ : full application

Note 1) Froude number defined by Eq. (1.1)

Note 2) Froude number defined by Eq. (3.12)

Table 3.2 Initial conditions of the ROCOM test 2.2 (Kurki, 2015)

<b>Parameter</b>	<b>Loop 1</b>	<b>Loop 2</b>	<b>Loop 3</b>	<b>Loop 4</b>
Normalized volume flow rate	0.0	12.2	12.2	12.2
Volume flow rate, l/s	0.0	6.27	6.27	6.27
Relative density	1.12	1.00	1.00	1.00
Temperature, °C	153	236.1	236.1	236.1

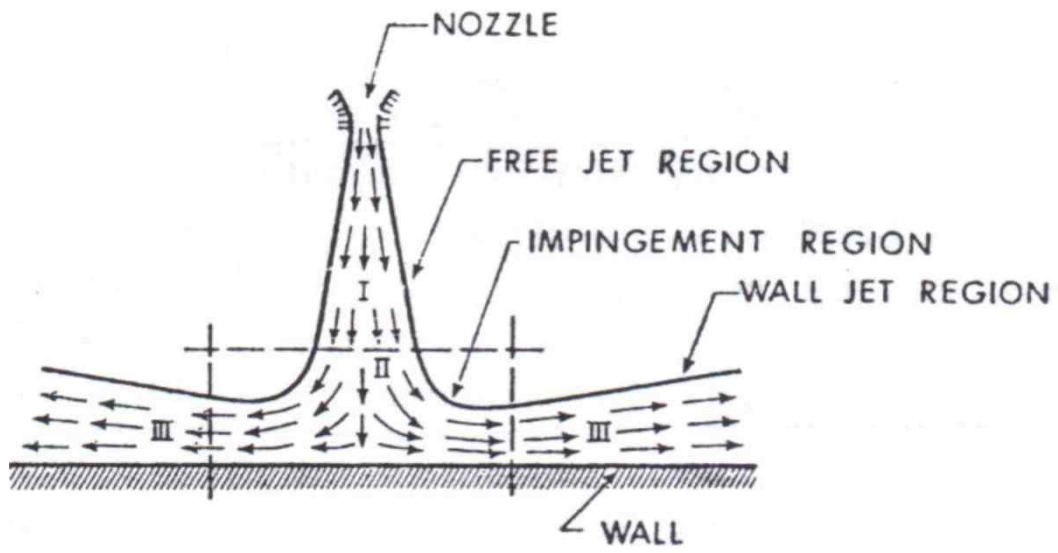


Figure 3.1 Geometry of the flow from a jet impinging normal to a wall (Beltaos & Rajaratnam, 1974)

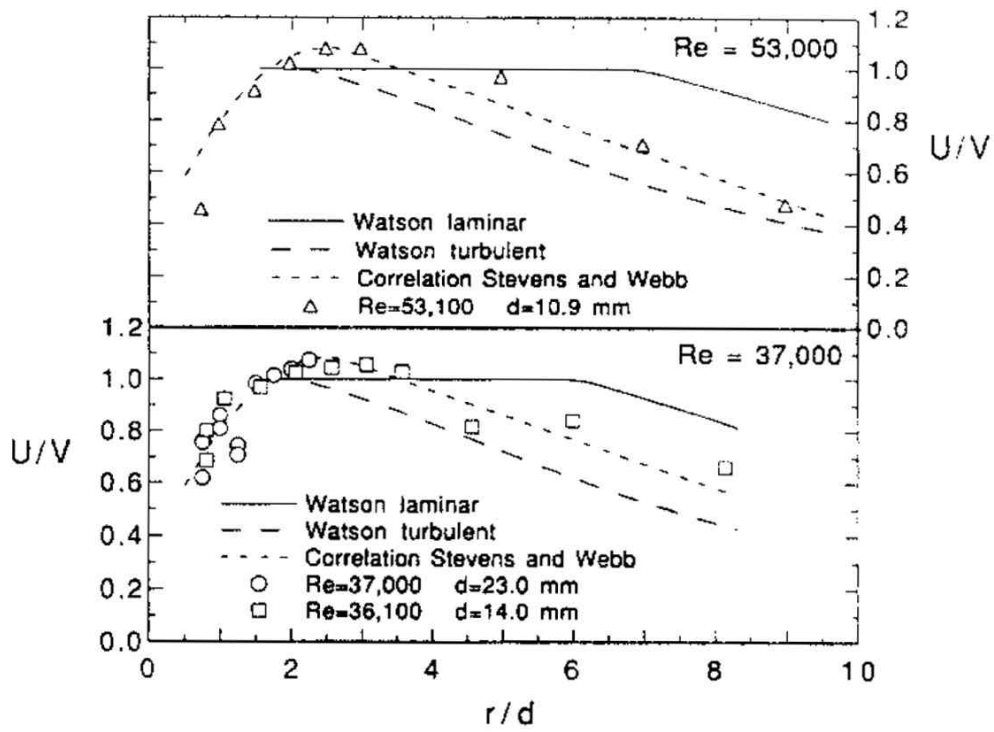
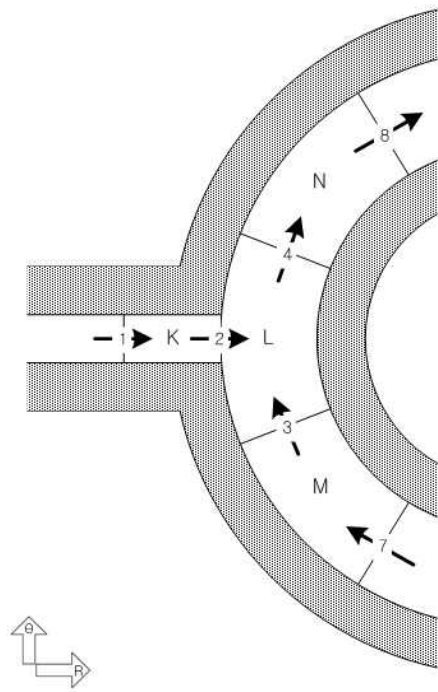
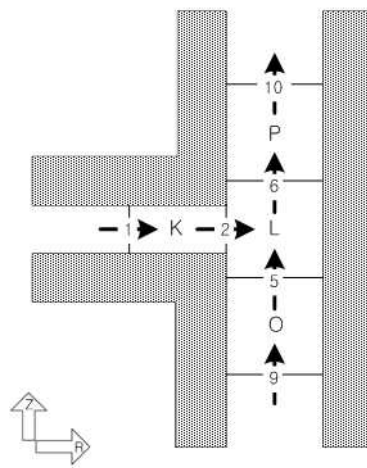


Figure 3.2 Comparison of analytical prediction for the free surface velocity with measurements (Stevens & Webb, 1992)



(a) plan view



(b) cross-sectional view

Figure 3.3 Example of the inlet nozzle and downcomer nodalization with the features of one-dimensional and three-dimensional

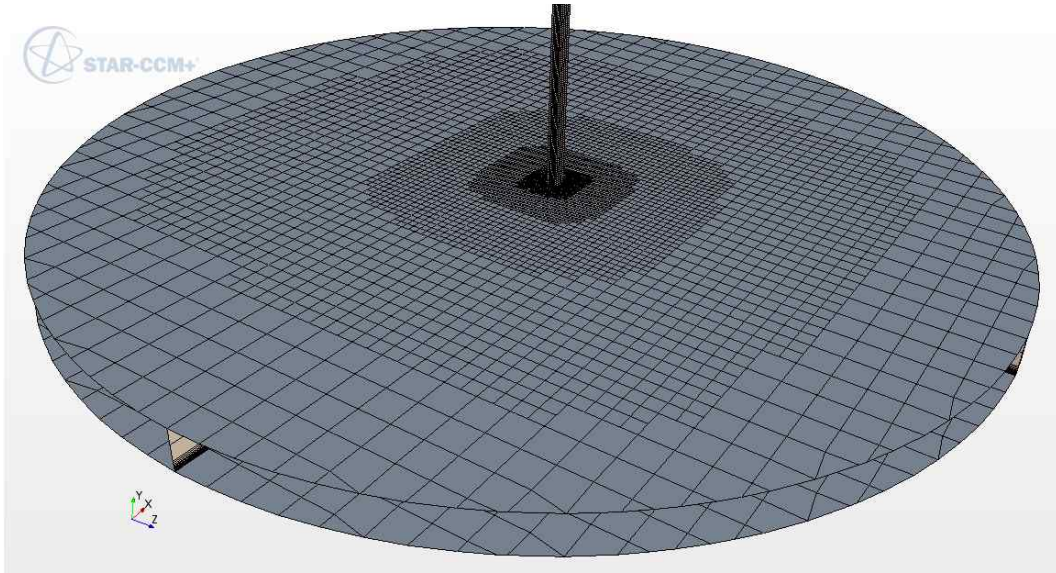


Figure 3.4 Structured hexagonal grids of the jet impingement phenomena validation model

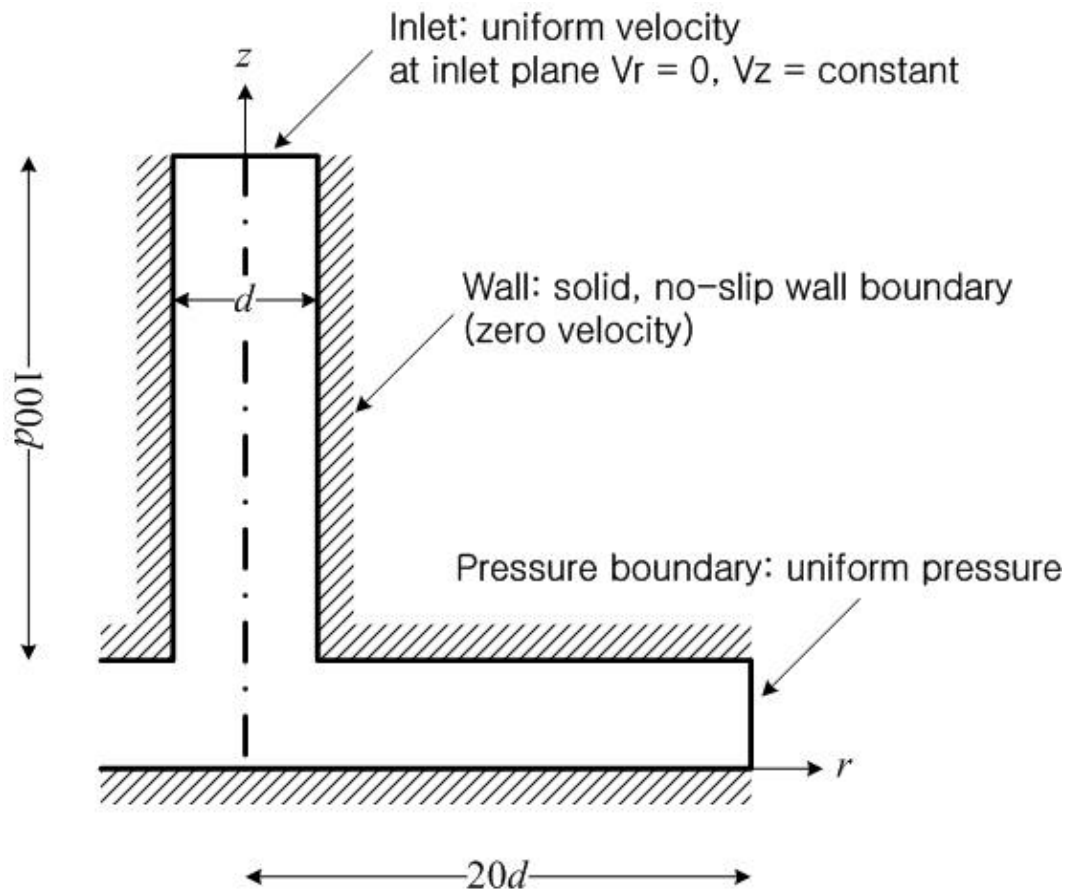


Figure 3.5 Flow domain boundaries for the jet impingement phenomena validation model

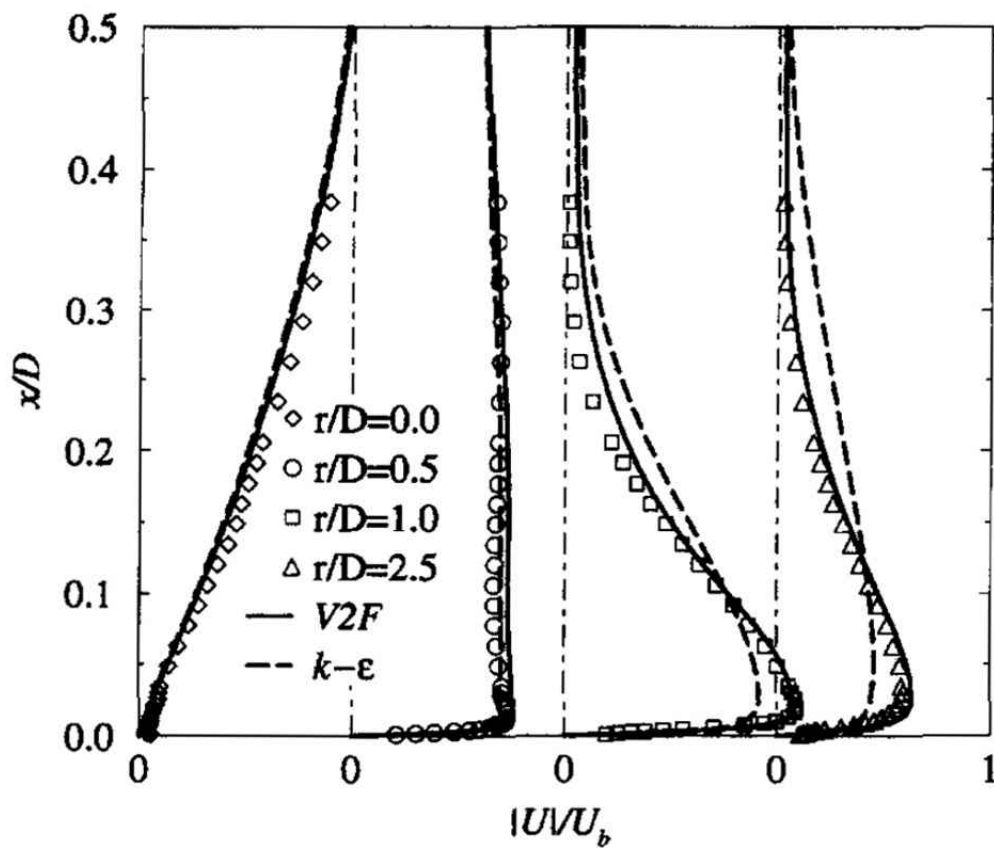


Figure 3.6 Profiles of the velocity magnitude normalized by the incoming velocity at a various radial location (Behnia et al., 1998; Cooper et al., 1993)

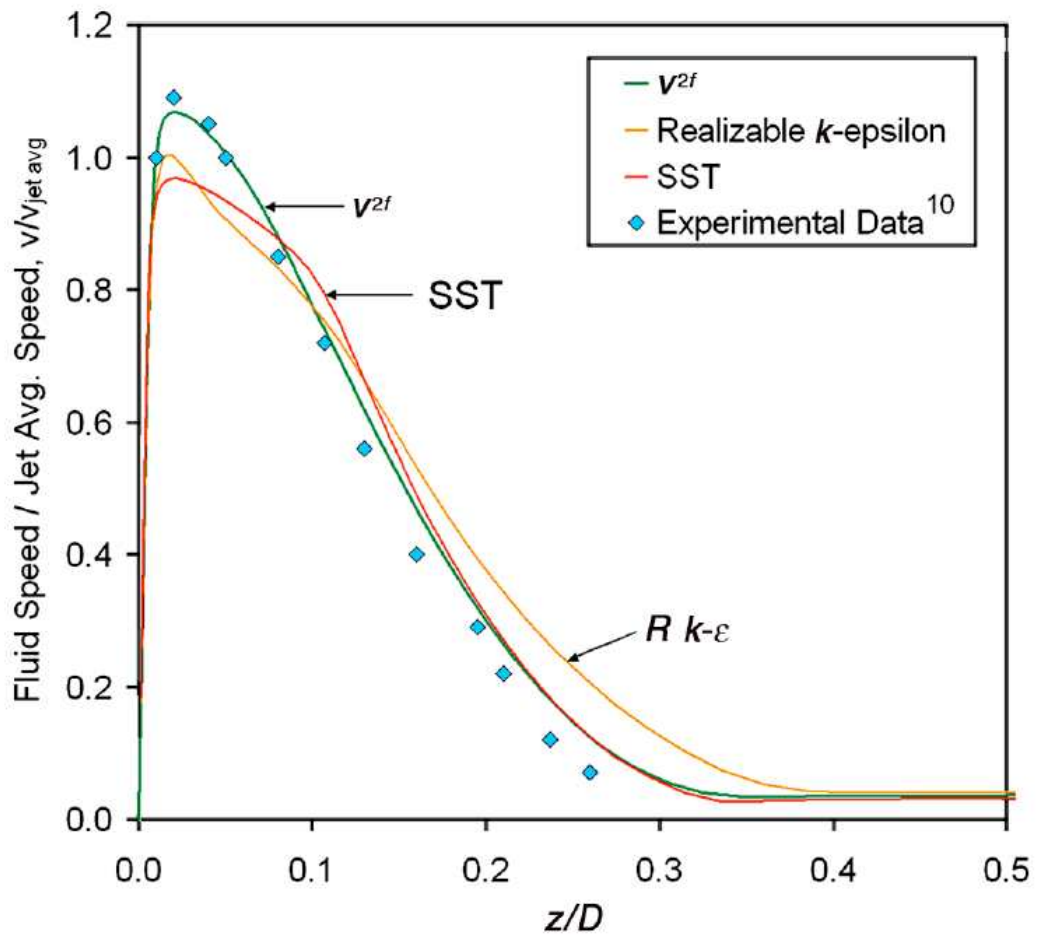


Figure 3.7 Profiles of the velocity magnitude normalized by the incoming velocity at  $r/d=1.0$  (Zuckerman & Lior, 2007; Cooper et al., 1993)

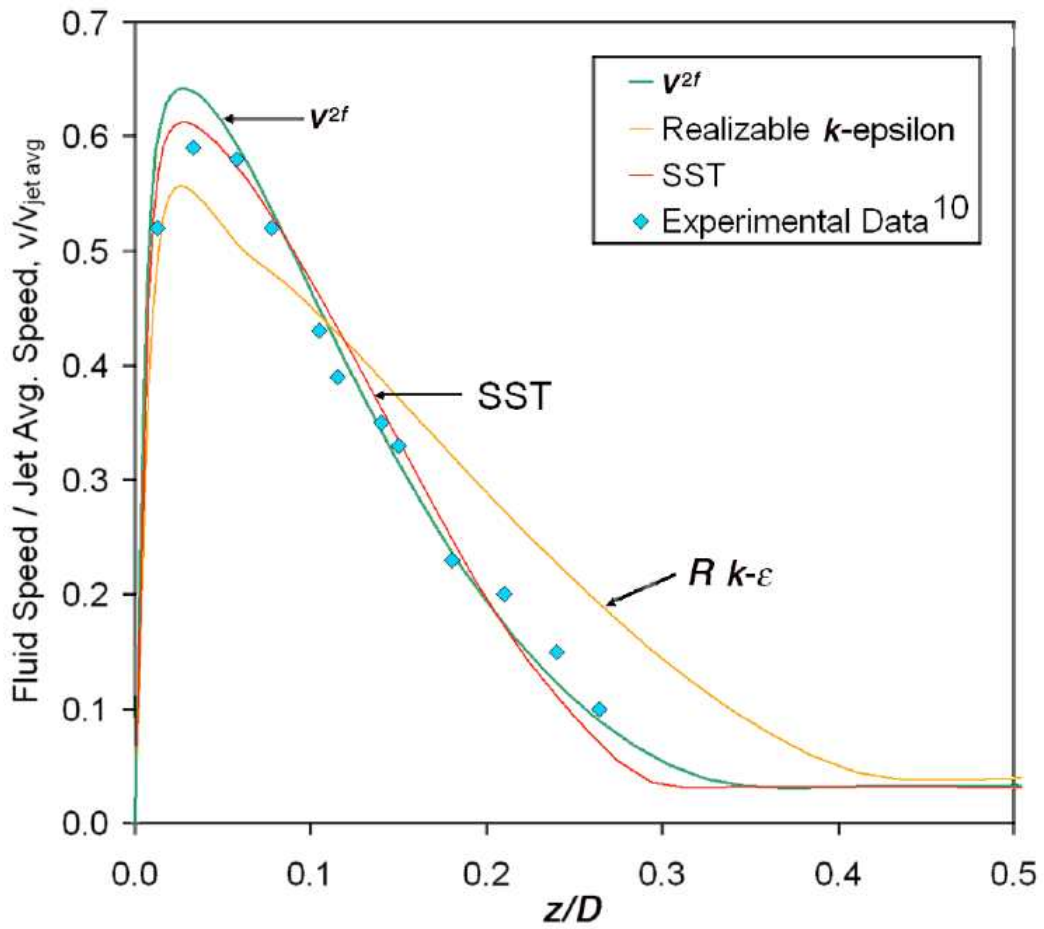


Figure 3.8 Profiles of the velocity magnitude normalized by the incoming velocity at  $r/d=2.5$  (Zuckerman & Lior, 2007; Cooper et al., 1993)

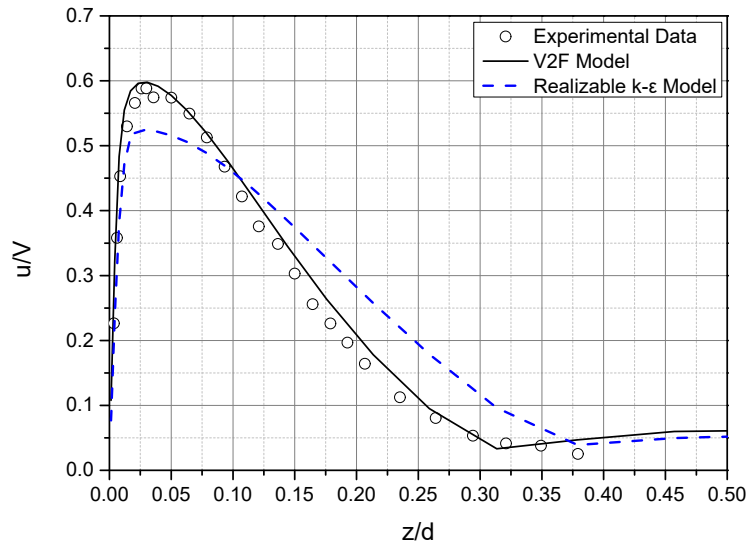


Figure 3.9 Profiles of the velocity magnitude normalized by the incoming velocity at  $r/d=2.5$  by using the jet impingement phenomena validation model (Cooper et al., 1993)

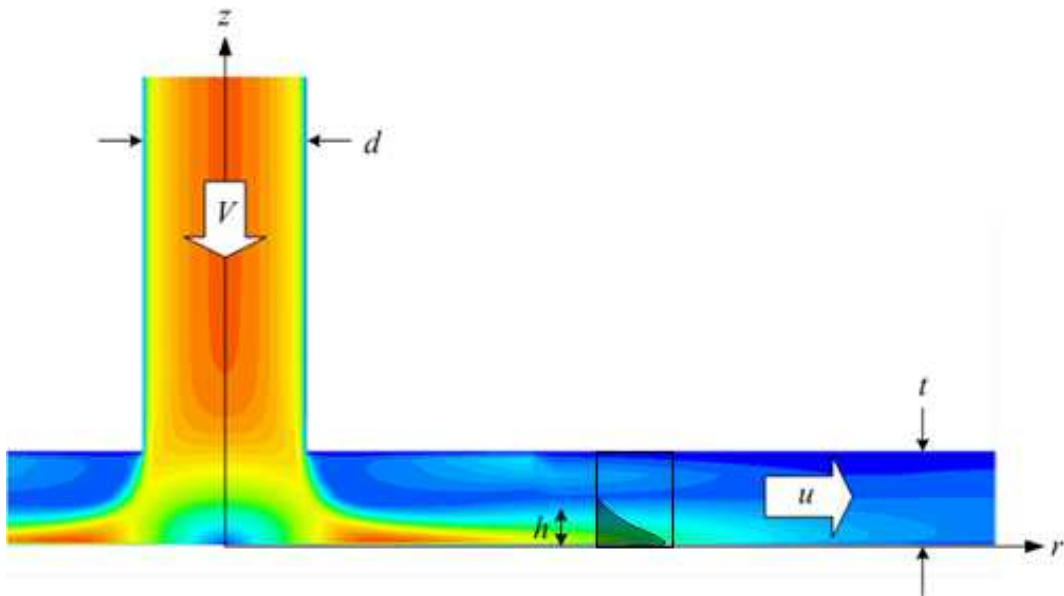


Figure 3.10 Schematic diagram of the parameters for the jet impingement model

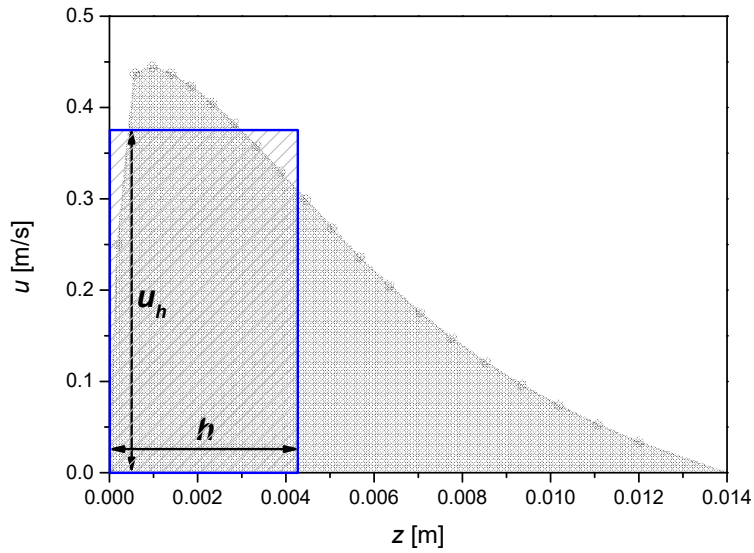


Figure 3.11 Example of the profile of the velocity magnitude ( $V=0.5$  m/s,  $d=0.05$  m,  $t = 0.025$  m,  $r = 0.01$  m)

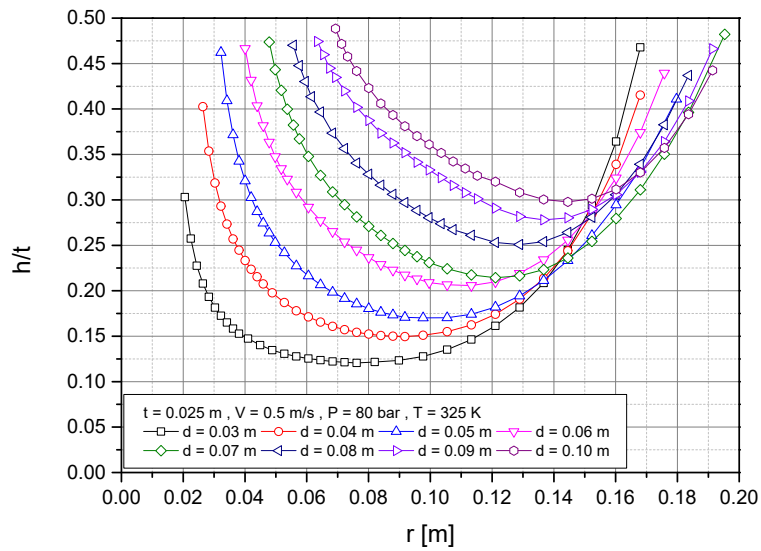


Figure 3.12 Results of the sensitivity calculation with various inlet nozzle diameters (non-dimensional thickness)

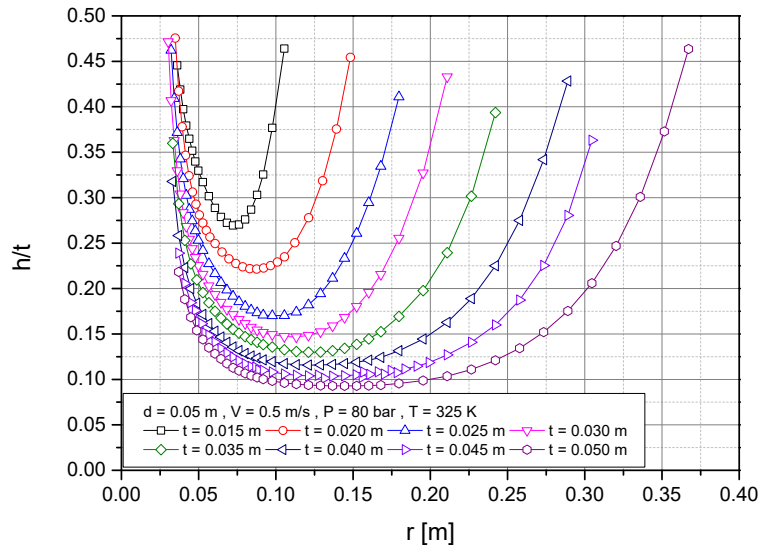


Figure 3.13 Results of the sensitivity calculation with various nozzle to wall spacing (non-dimensional thickness)

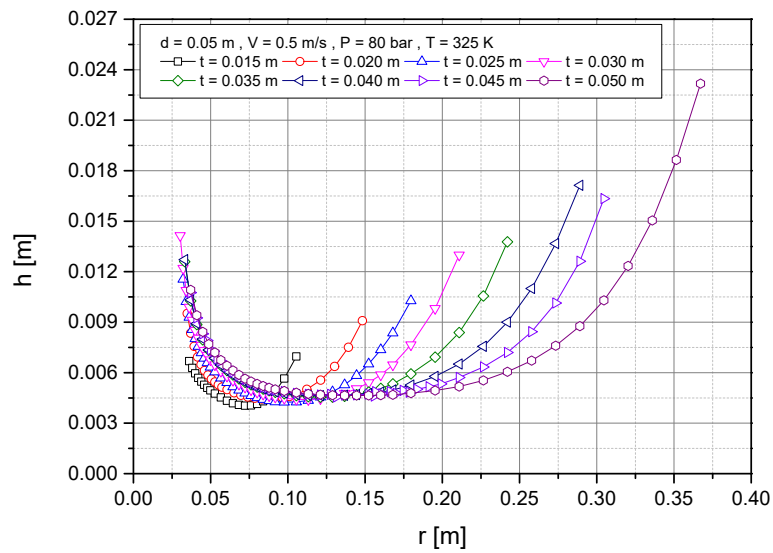


Figure 3.14 Results of the sensitivity calculation with various nozzle to wall spacing (momentum boundary layer thickness)

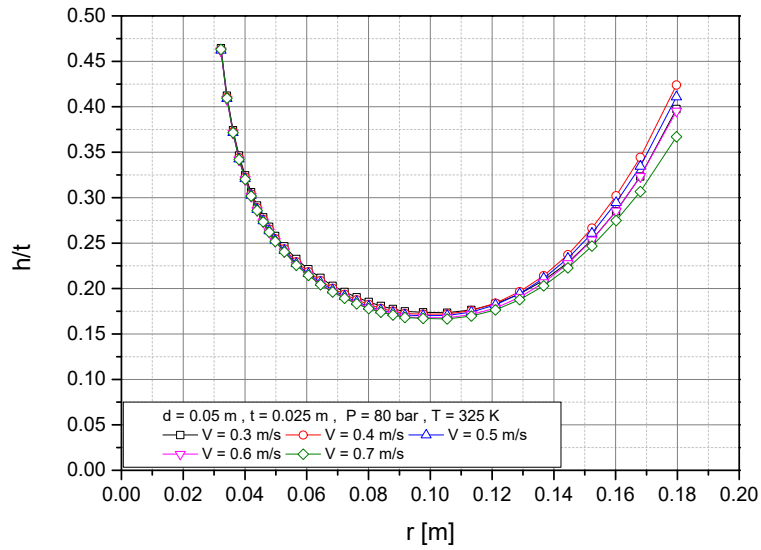


Figure 3.15 Results of the sensitivity calculation with various nozzle inlet velocity (non-dimensional thickness)

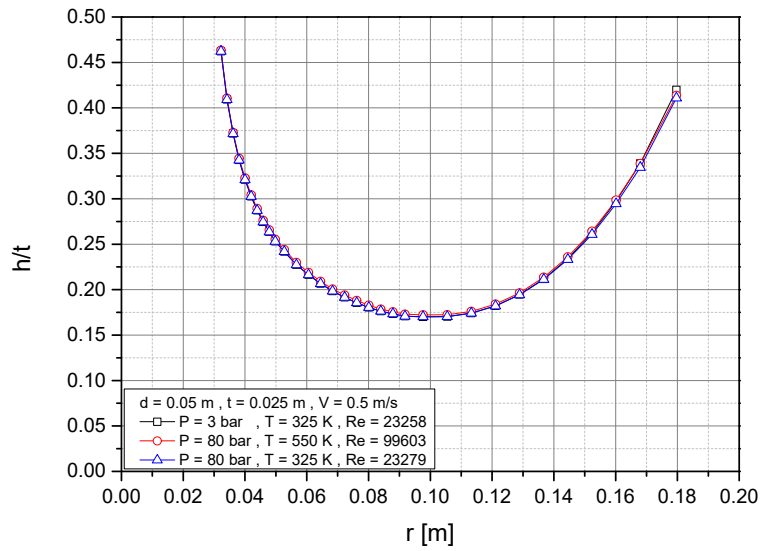


Figure 3.16 Results of the sensitivity calculation with various fluid properties (non-dimensional thickness)

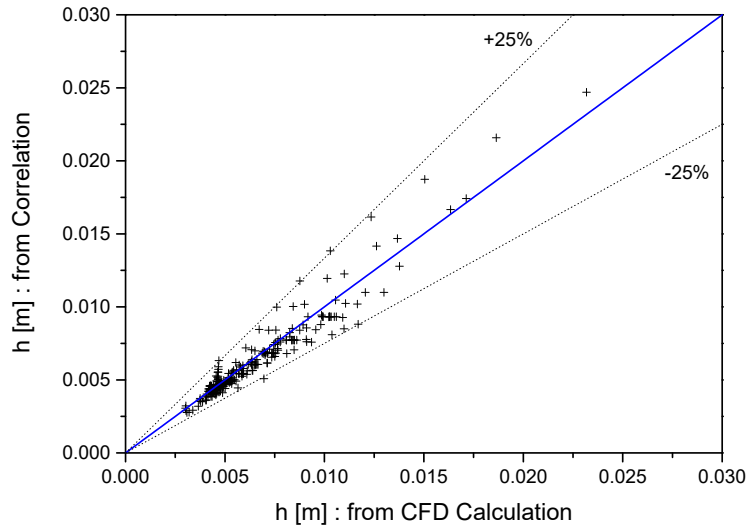


Figure 3.17 Comparison of the correlation with the computed results

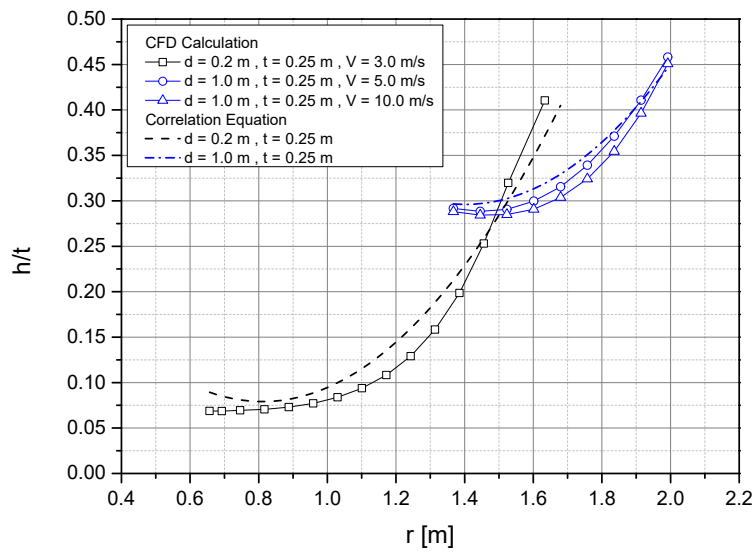


Figure 3.18 Results of the calculation to confirm the scale-up capability of the correlation equation

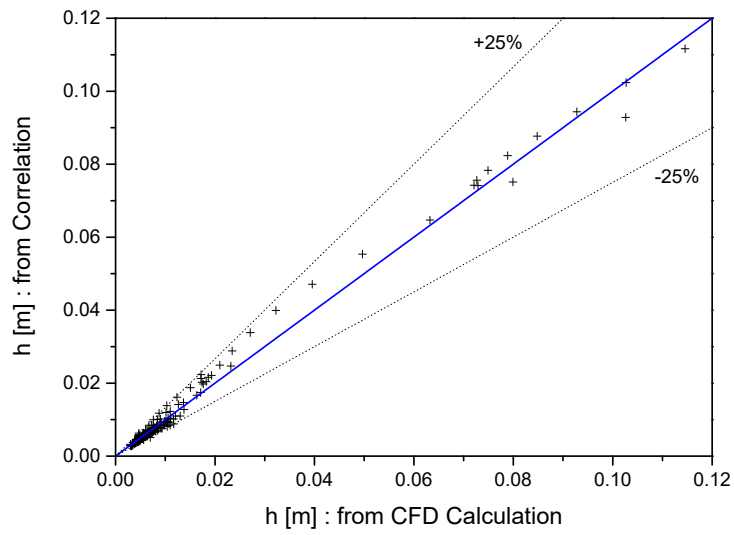


Figure 3.19 Comparison of the correlation with the computed results on the prototype scale

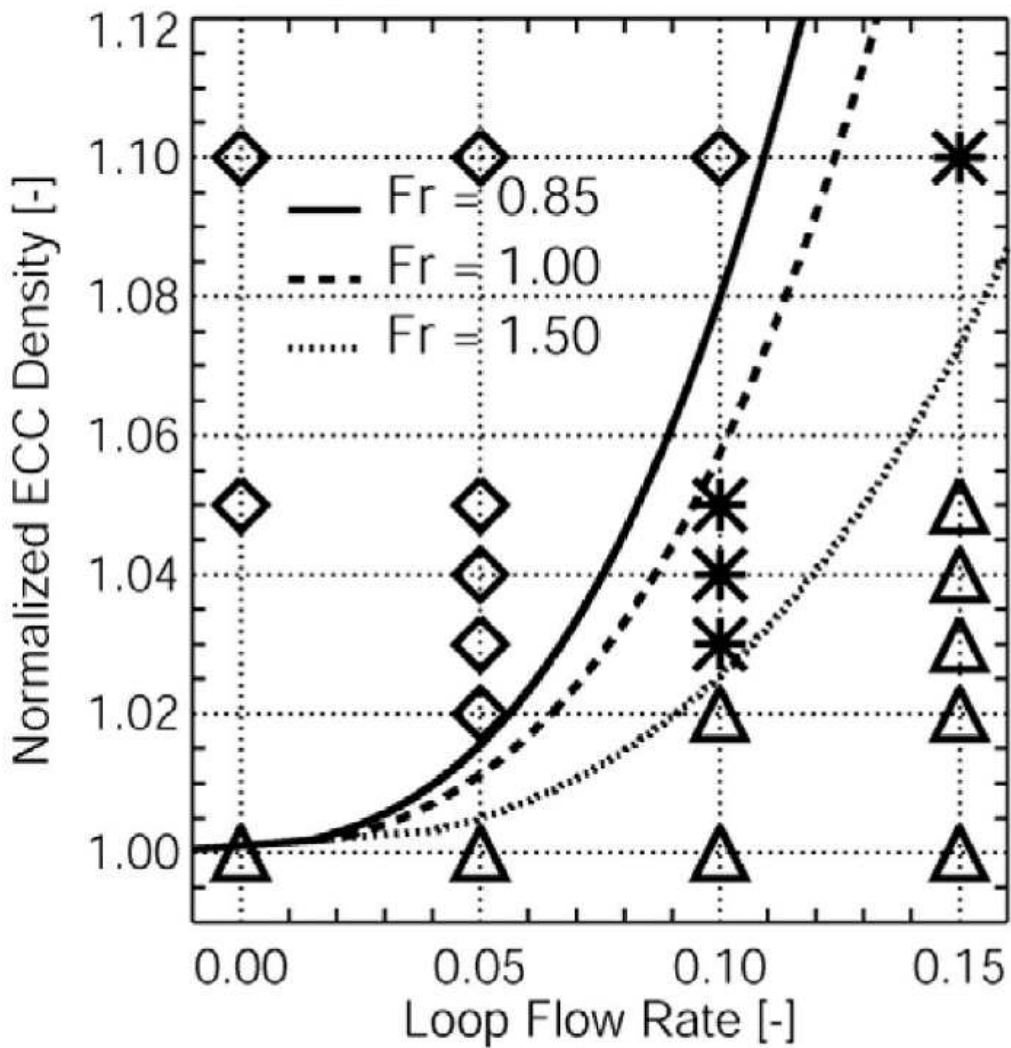


Figure 3.20 Test matrix of ECC injection experiments, classification of the ROCOM tests, isolines of Froude numbers (Höhne & Kliem, 2007)

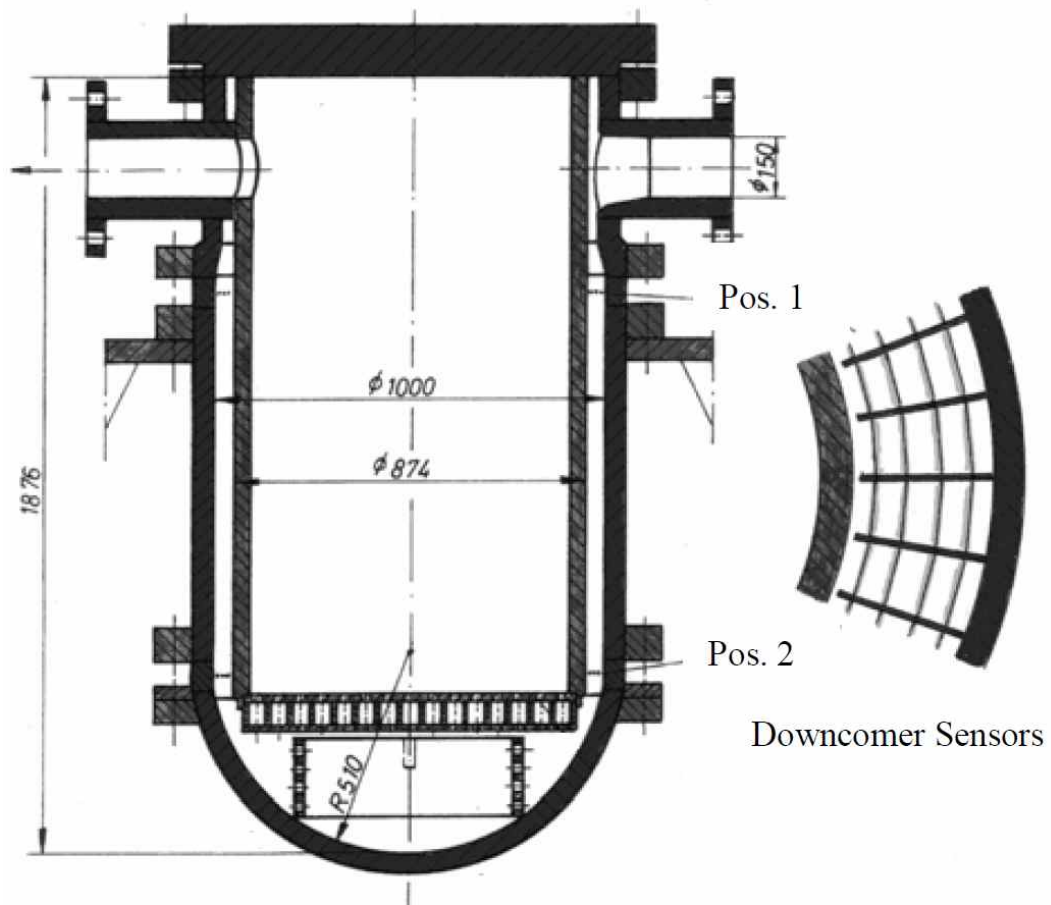


Figure 3.21 Positions of wire mesh downcomer sensors in the ROCOM (Rohde et al., 2005)

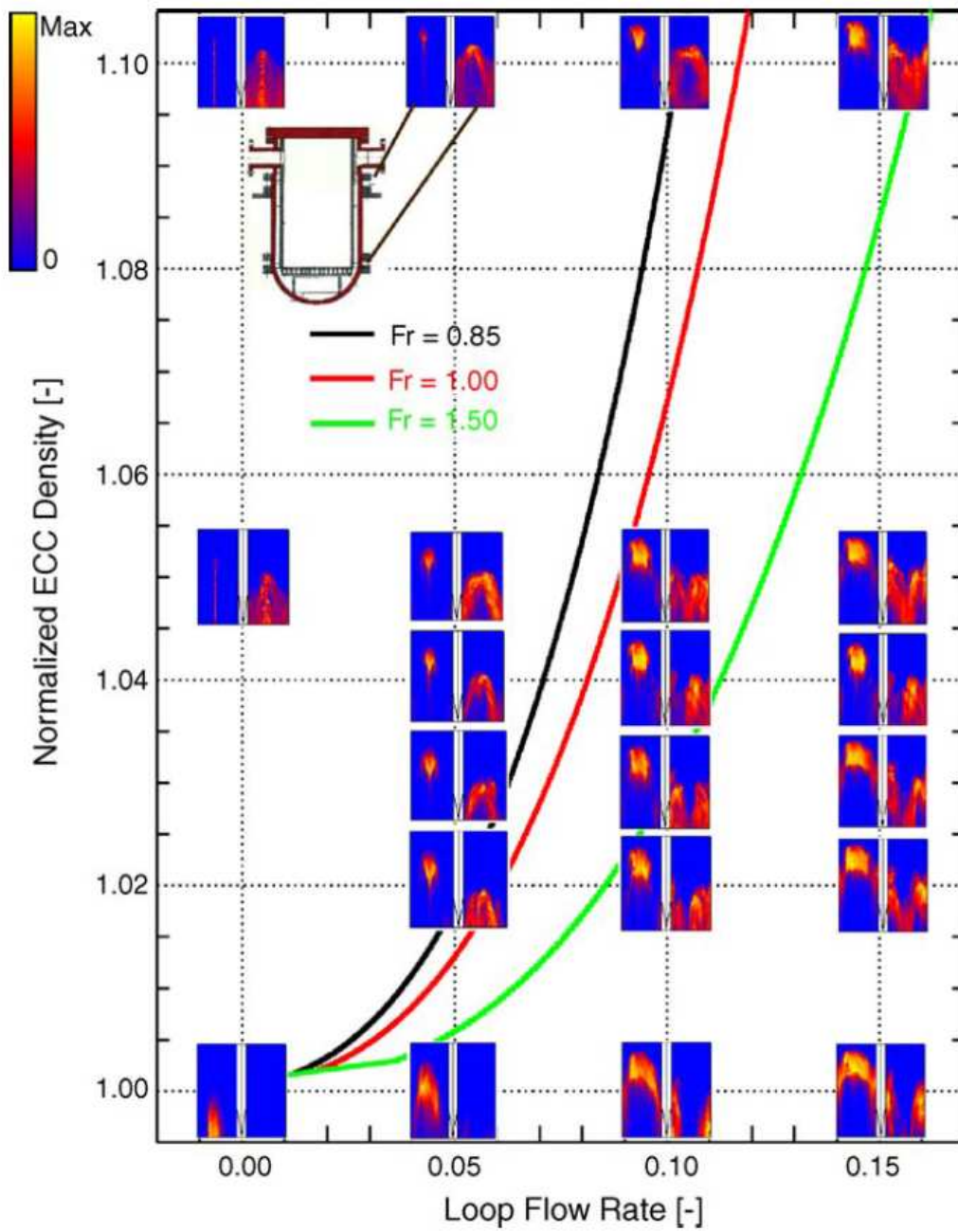
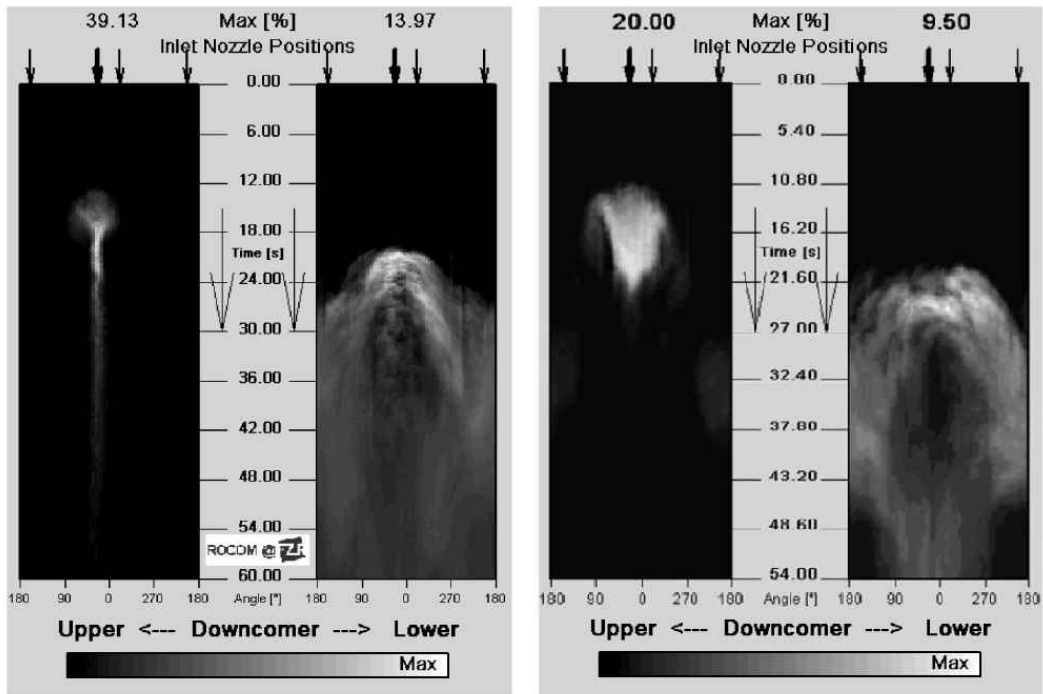


Figure 3.22 Test matrix of ECC injection experiments, visualization of the time-dependent tracer distribution at the sensors in the downcomer, isolines of Froude numbers (Höhne et al., 2006)



(a) 5% mass flow rate  
and 10% density difference

(b) 10% mass flow rate  
and 10% density difference

Figure 3.23 Mixing scalar evolution in the downcomer in ROCOM buoyance driven mixing tests (Höhne & Kliem, 2007; Rohde et al., 2005)

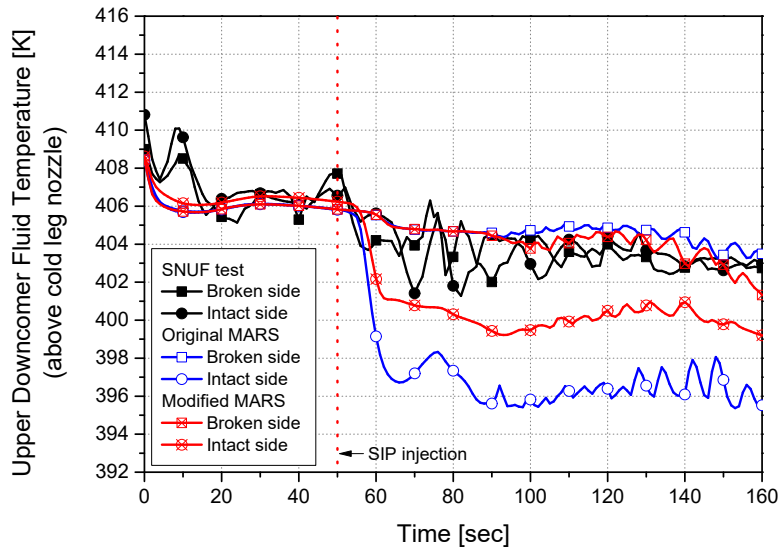


Figure 3.24 Comparison of the upper downcomer fluid temperature between the original and modified MARS analysis for SNUF

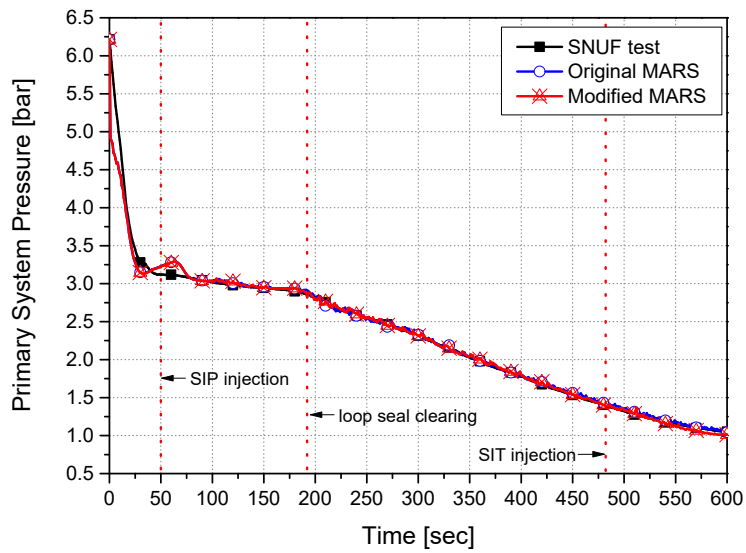


Figure 3.25 Comparison of the primary system pressure between the original and modified MARS analysis for SNUF

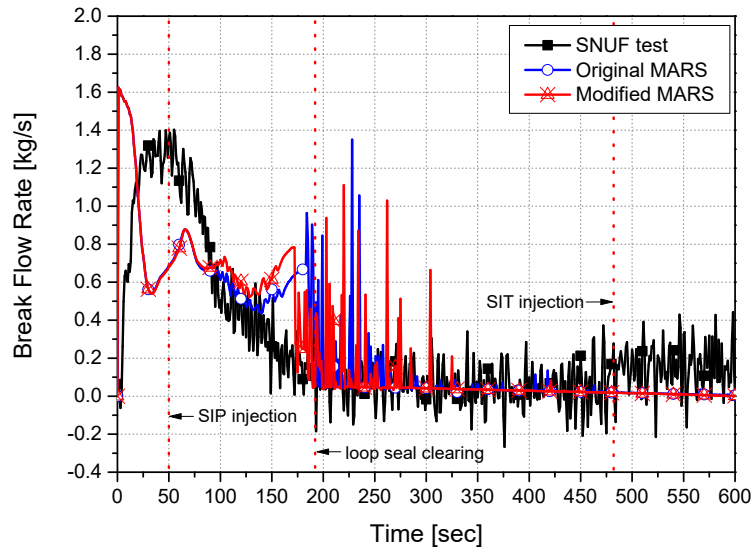


Figure 3.26 Comparison of the break flow rate between the original and modified MARS analysis for SNUF

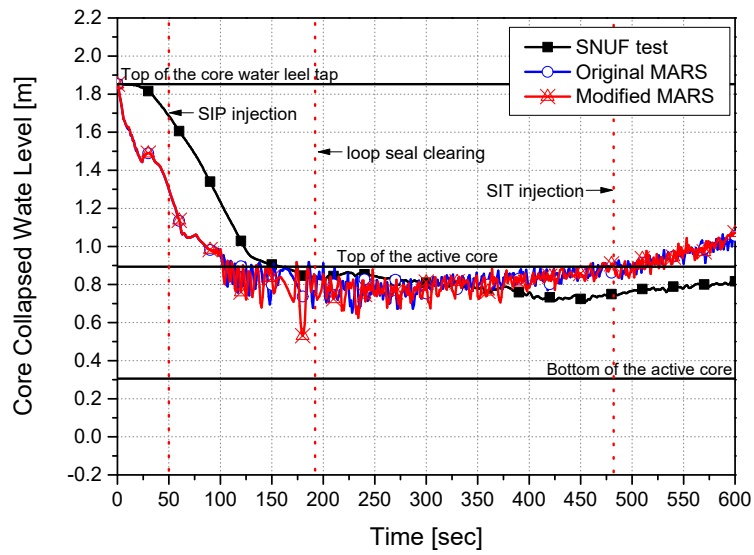


Figure 3.27 Comparison of the core collapsed water level between the original and modified MARS analysis for SNUF

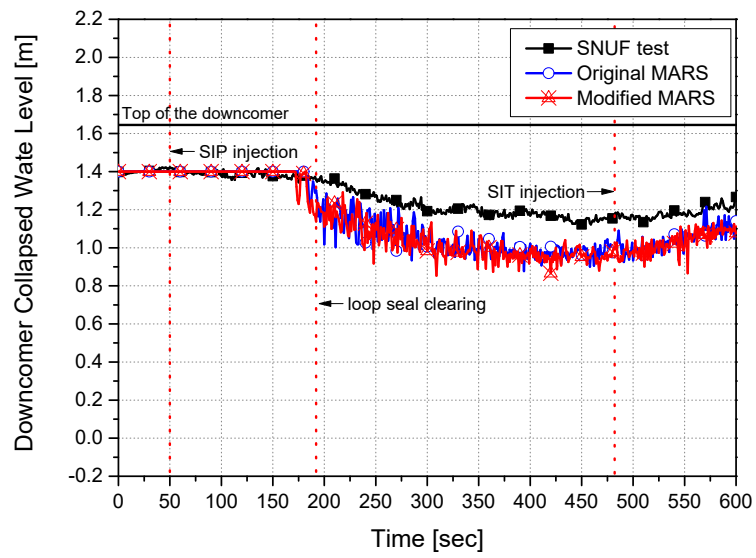


Figure 3.28 Comparison of the downcomer collapsed water level between the original and modified MARS analysis for SNUF

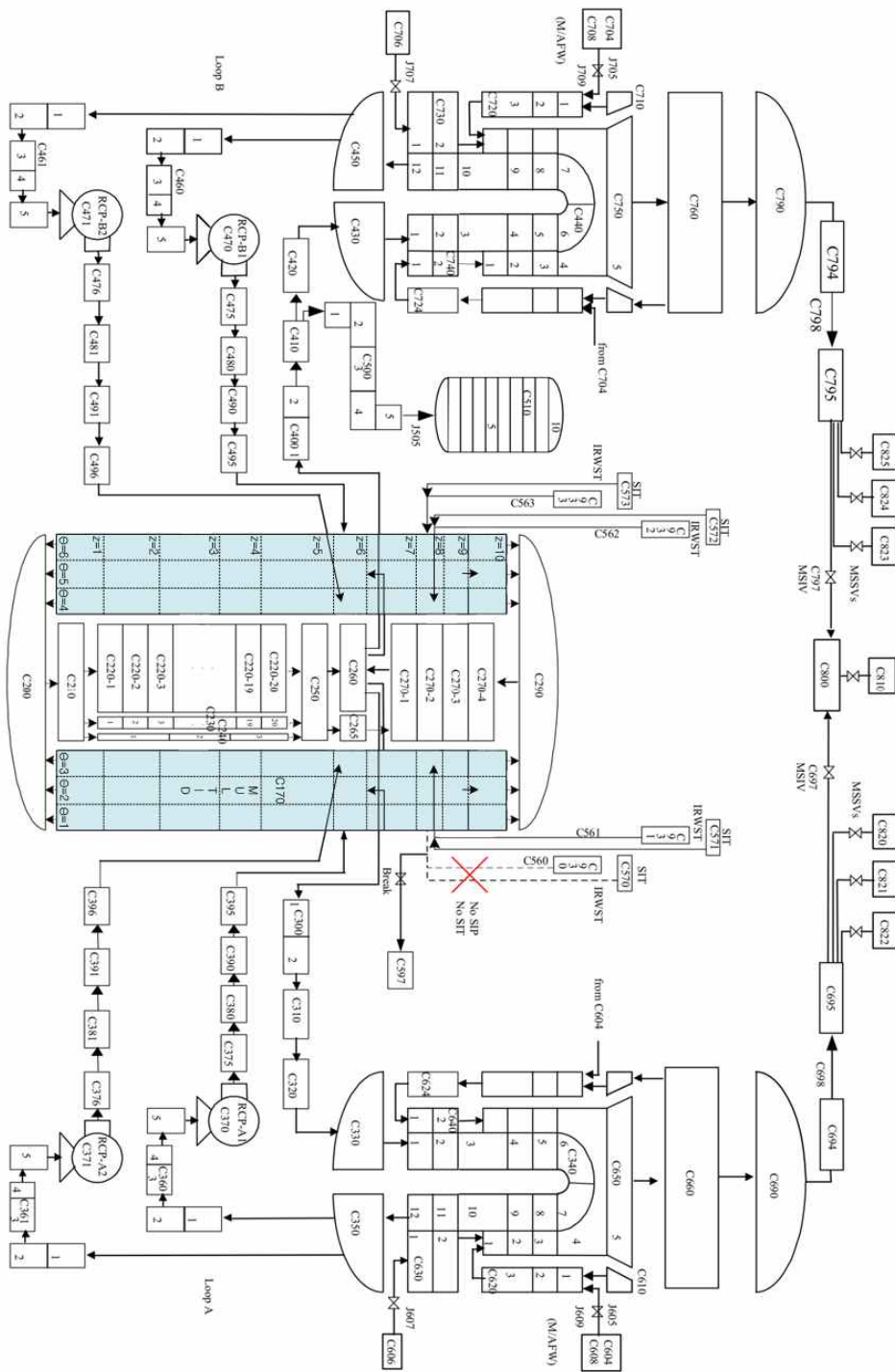


Figure 3.29 Schematic nodalization of the MARS model for the ATLAS

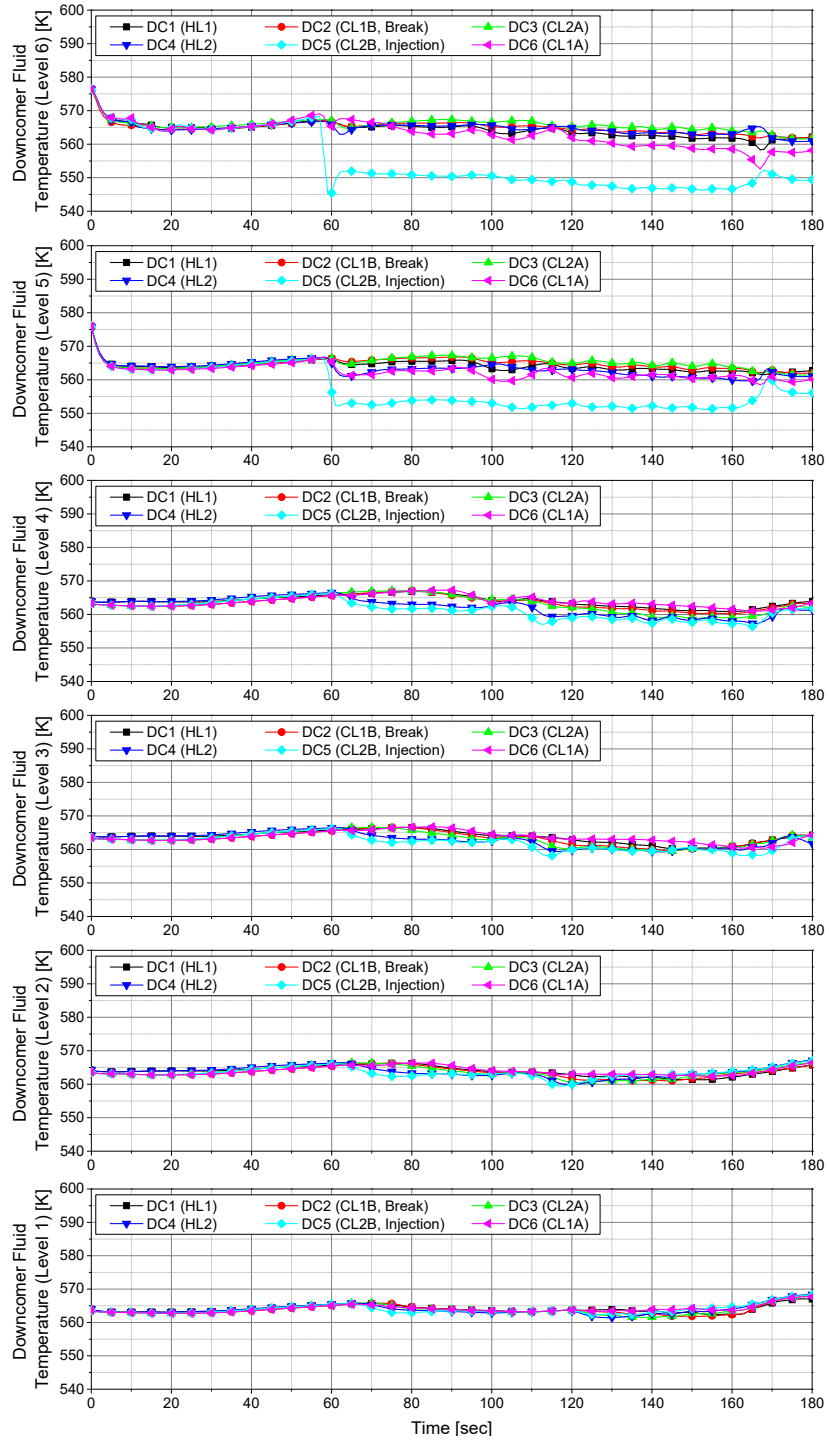


Figure 3.30 Downcomer fluid temperature of the original MARS analysis for the ATLAS

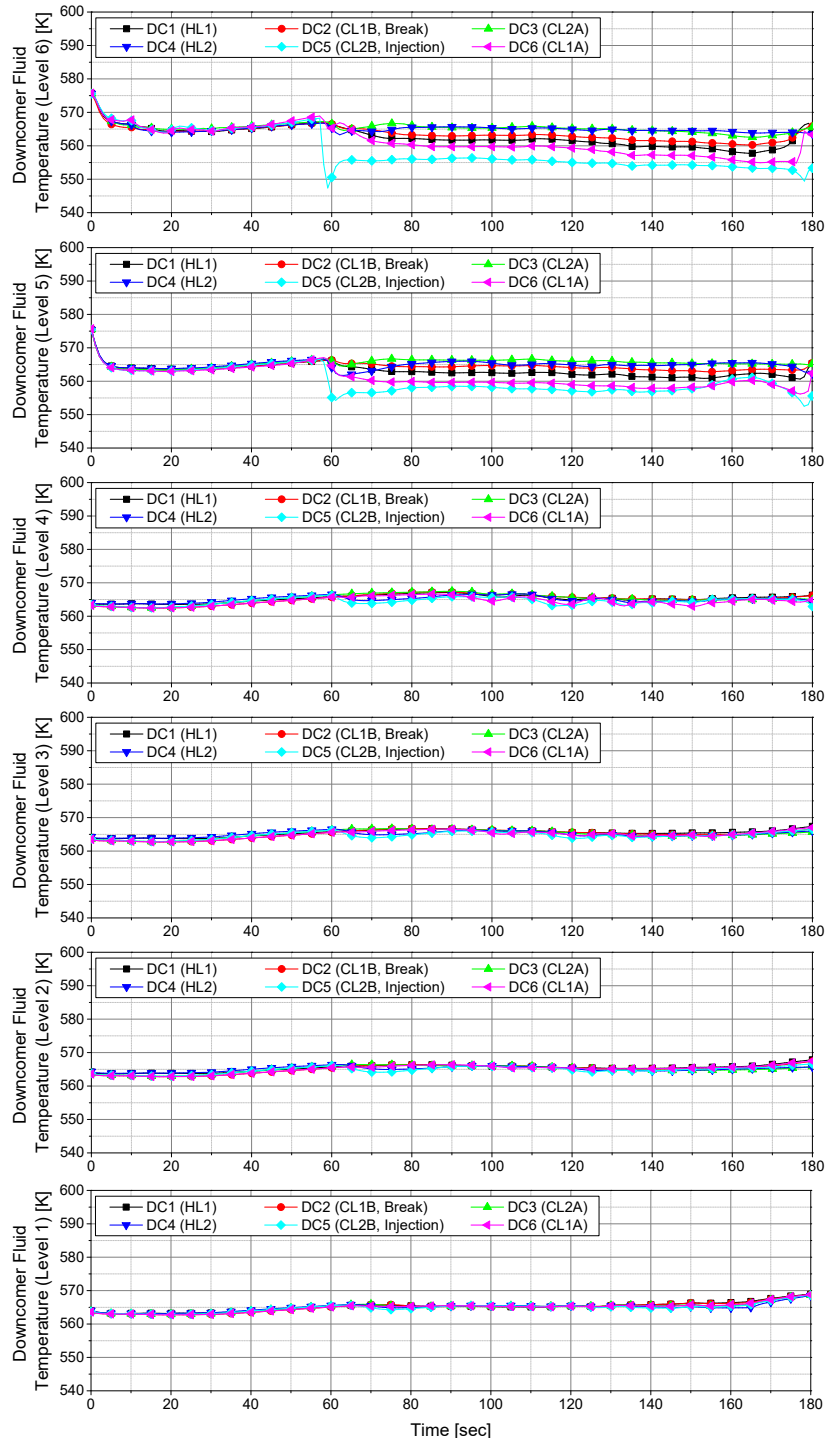


Figure 3.31 Downcomer fluid temperature of the modified MARS analysis for the ATLAS

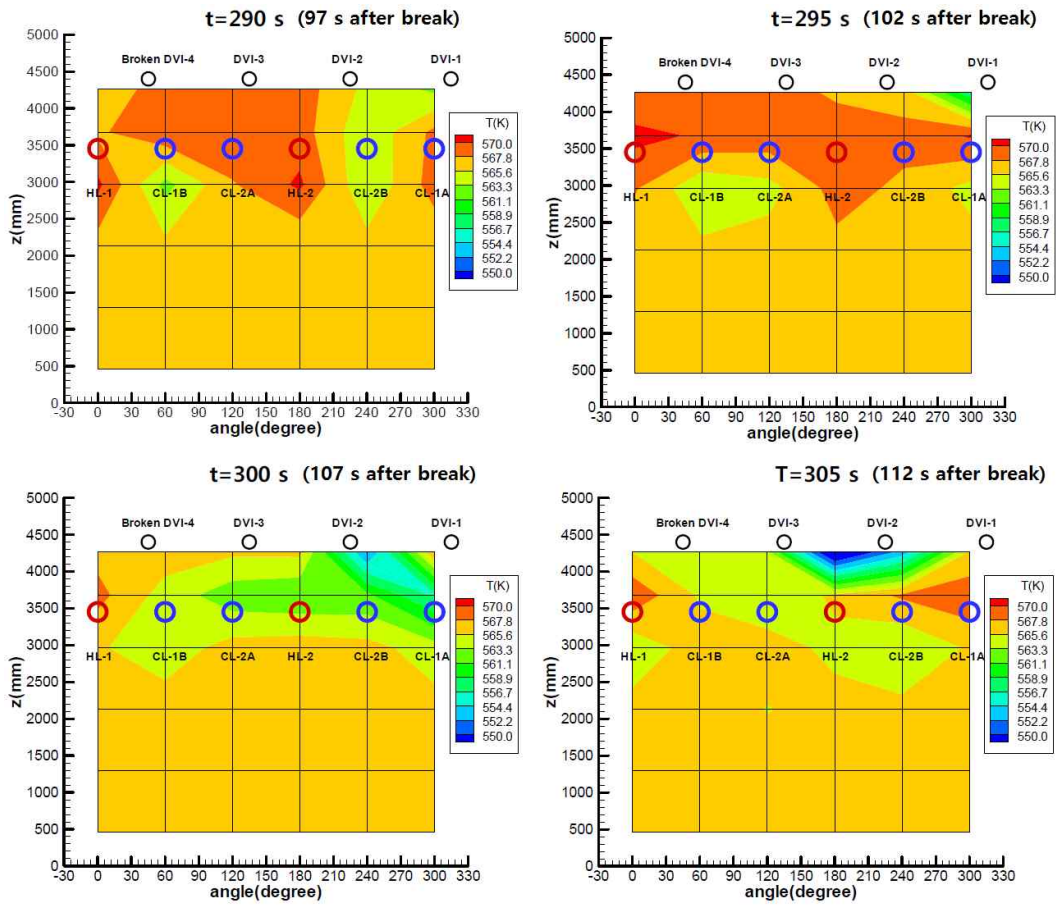


Figure 3.32 Contour map of the downcomer fluid temperature of the ATLAS test (OECD/NEA, 2012)

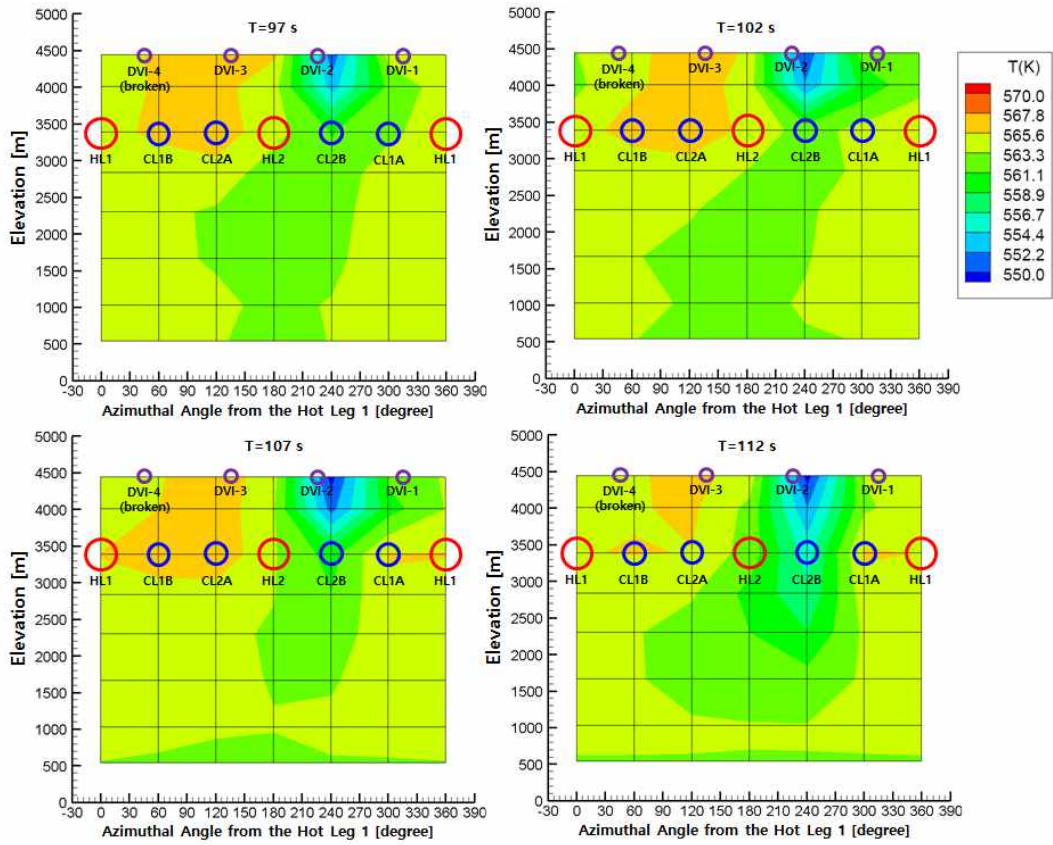


Figure 3.33 Contour map of the downcomer fluid temperature of the original MARS analysis for the ATLAS

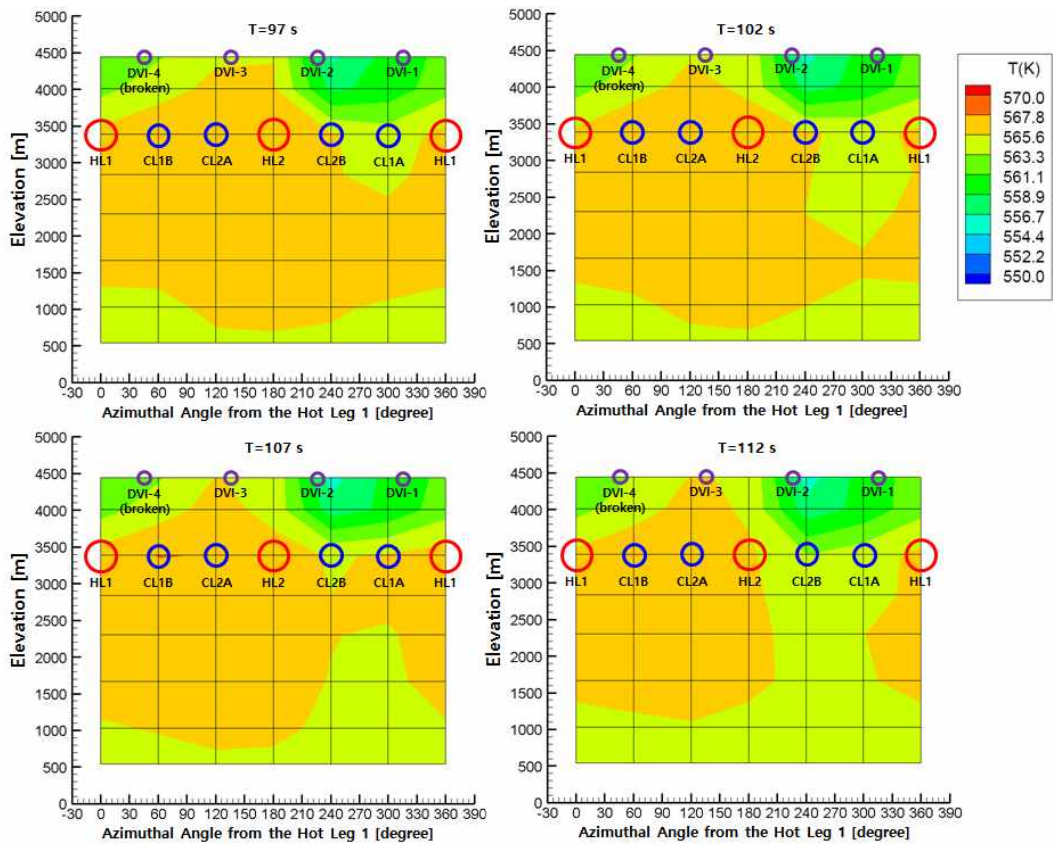


Figure 3.34 Contour map of the downcomer fluid temperature of the modified MARS analysis for the ATLAS

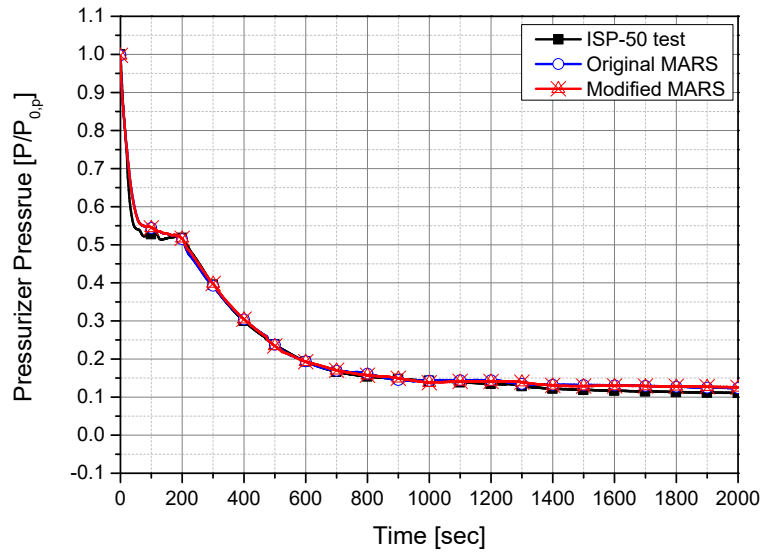


Figure 3.35 Comparison of the primary system pressure between the original and modified MARS analysis for the ATLAS in the normalized scale

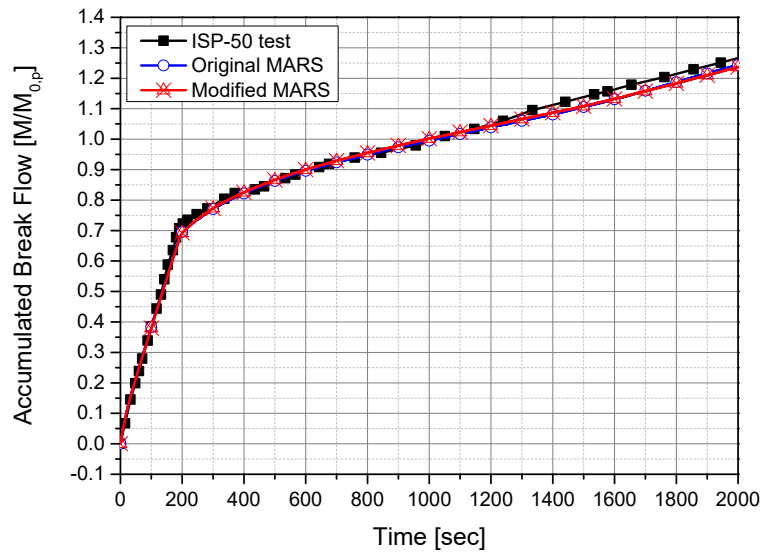


Figure 3.36 Comparison of the accumulated break flow between the original and modified MARS analysis for the ATLAS in the normalized scale

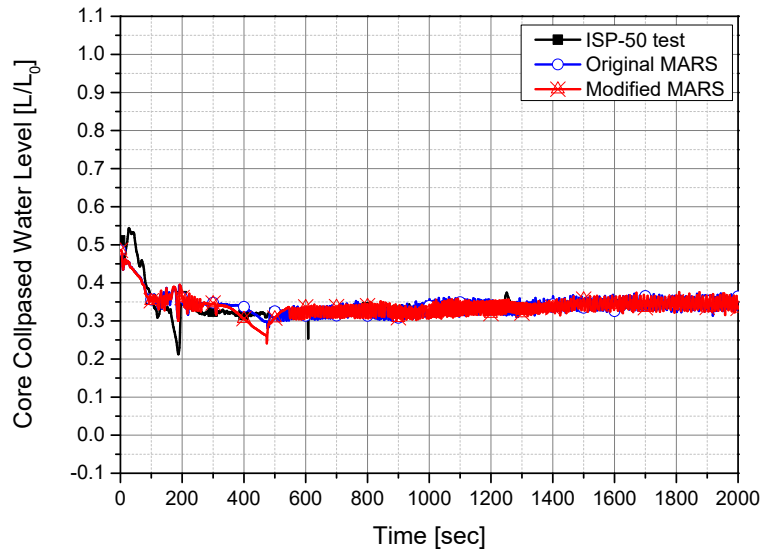


Figure 3.37 Comparison of the core collapsed water level between the original and modified MARS analysis for the ATLAS in the normalized scale

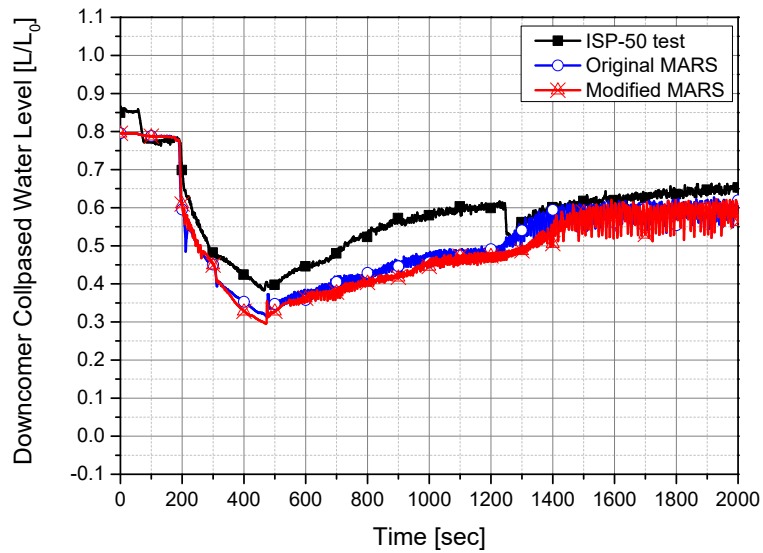


Figure 3.38 Comparison of the downcomer collapsed water level between the original and modified MARS analysis for the ATLAS in the normalized scale

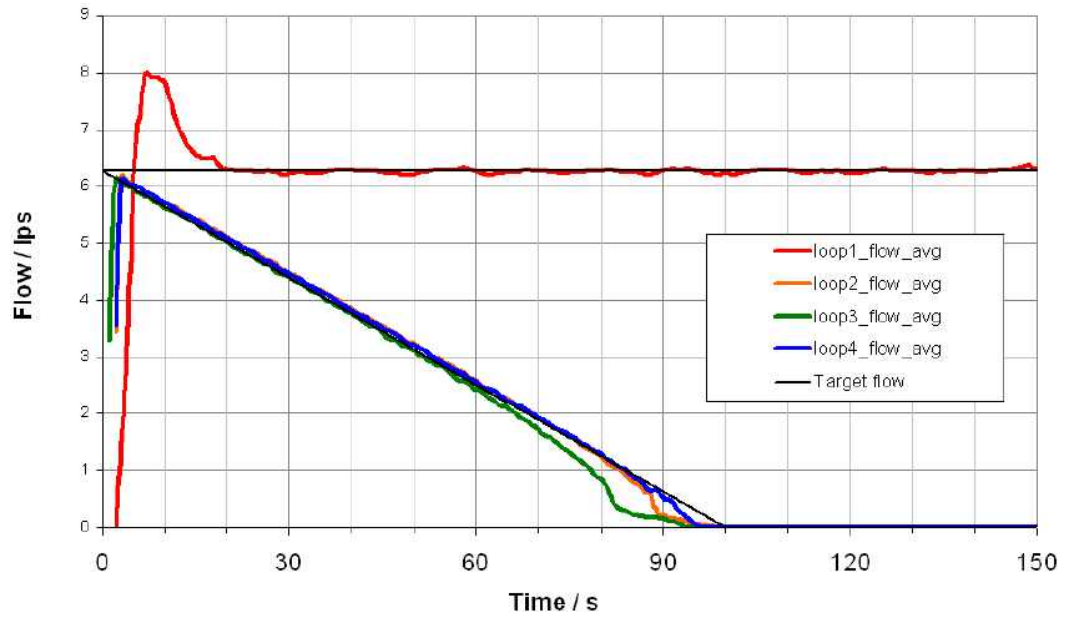


Figure 3.39 Measured loop flow rate in the ROCOM test 2.2 (Kurki, 2015)

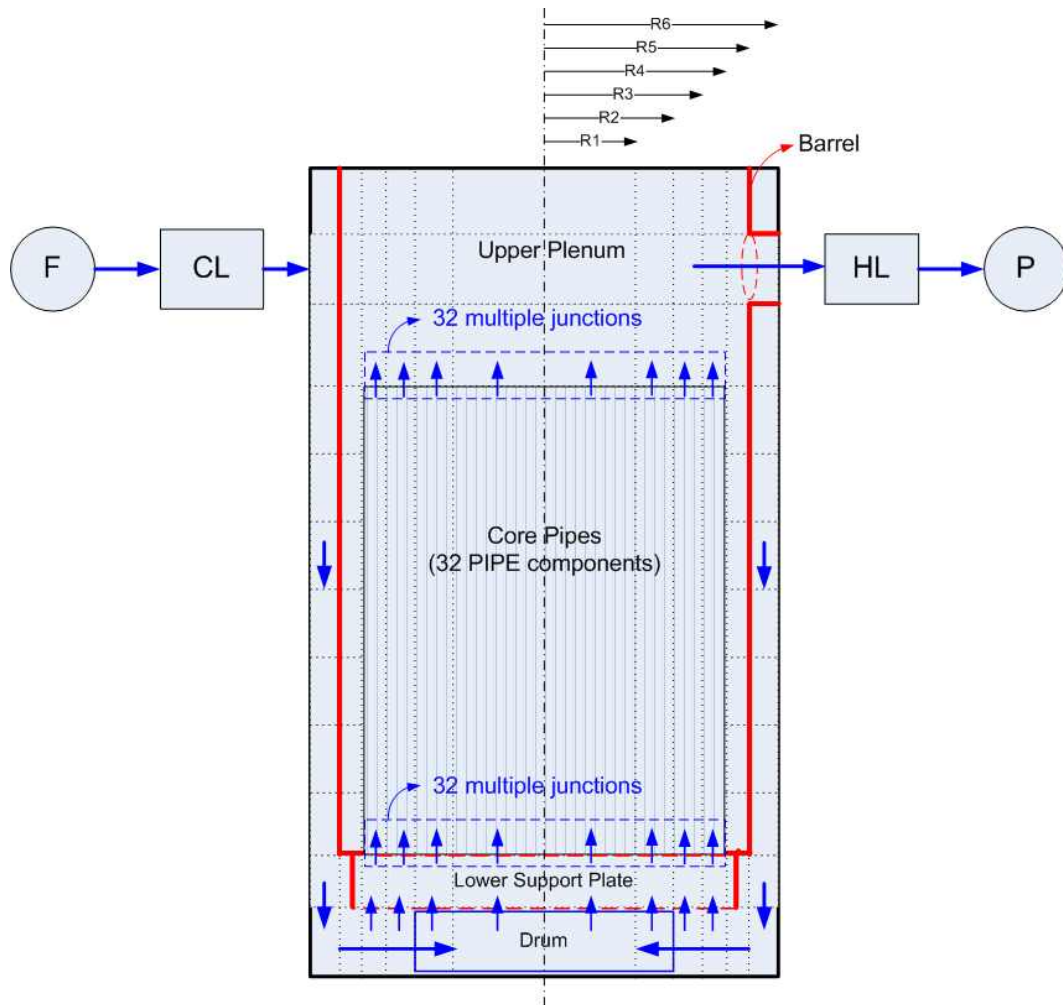


Figure 3.40 Schematic nodalization of the MARS model for the ROCOM (Lee & Chung, 2012)

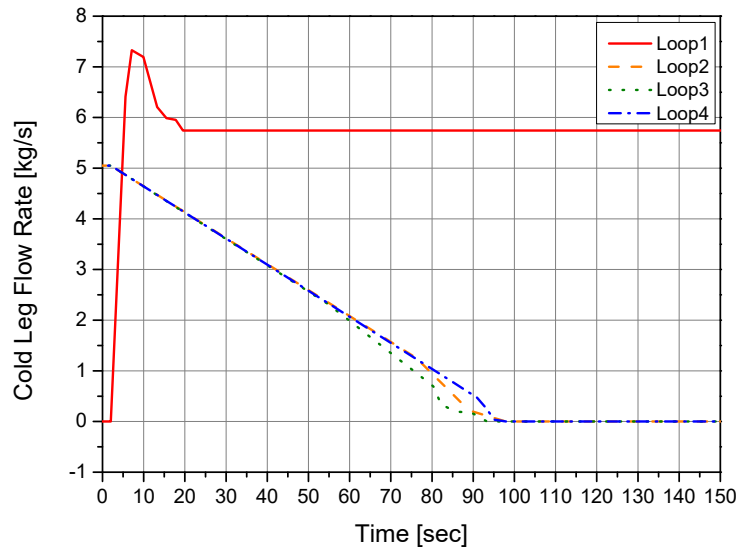
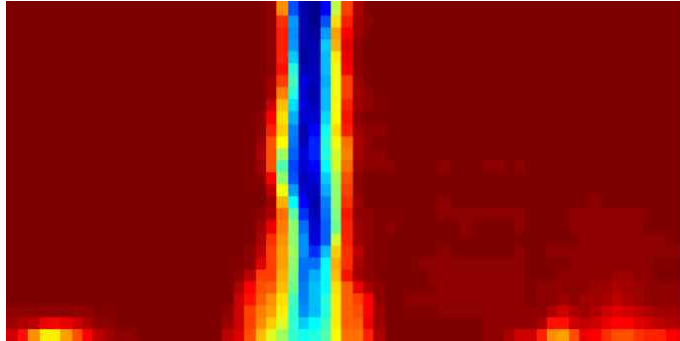
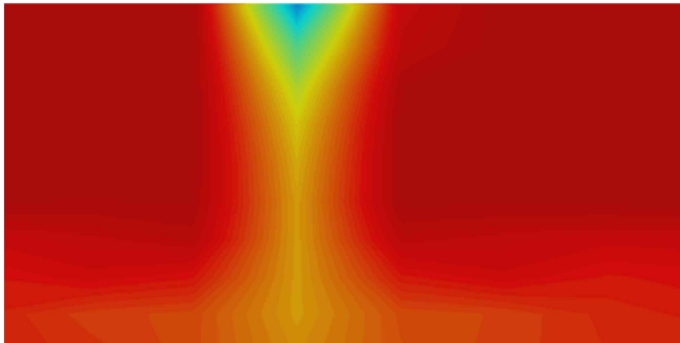


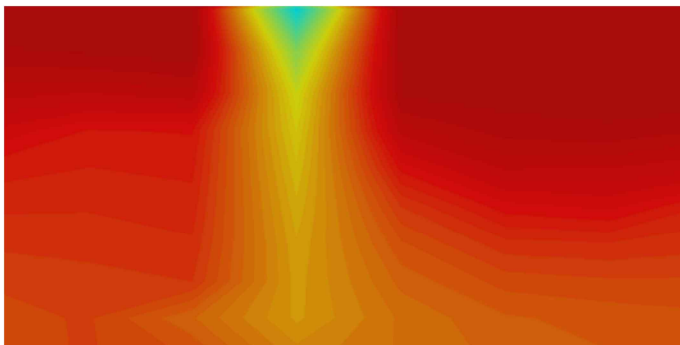
Figure 3.41 Cold leg flow rate as the input for the MARS analysis



(a) ROCOM test 2.2



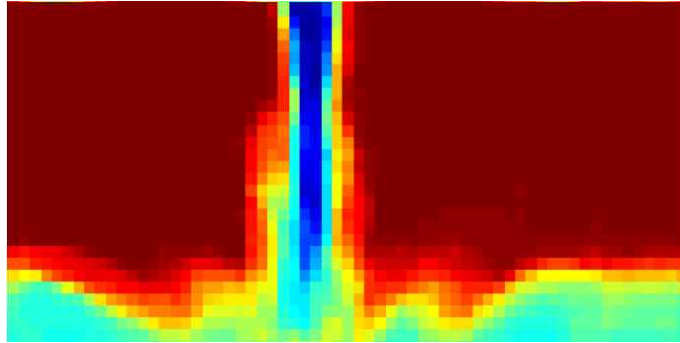
(b) original MARS analysis



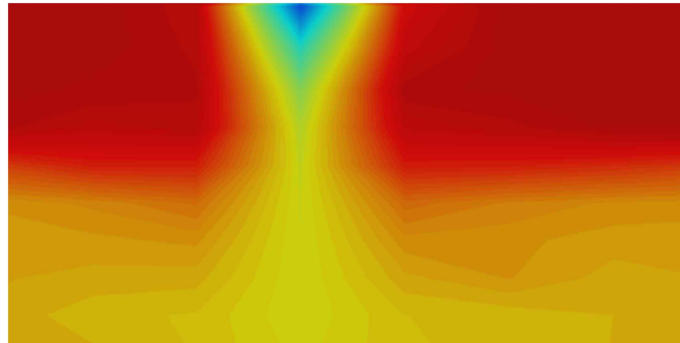
(c) modified MARS analysis

Figure 3.42 Comparison of the temperature distribution in the unwrapped downcomer at 30 seconds between the ROCOM test 2.2 and the MARS analysis (Kliem & Franz, 2012)

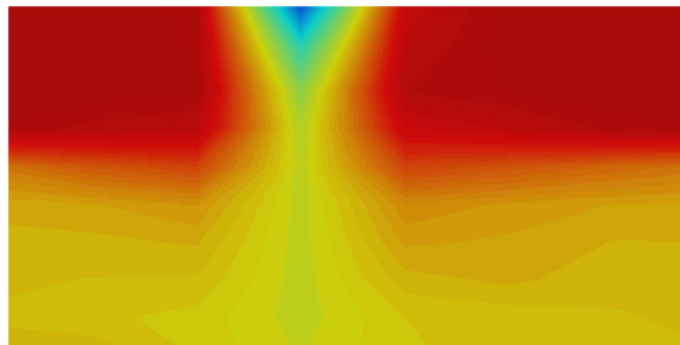
153.0 °C  236.1 °C



(a) ROCOM test 2.2



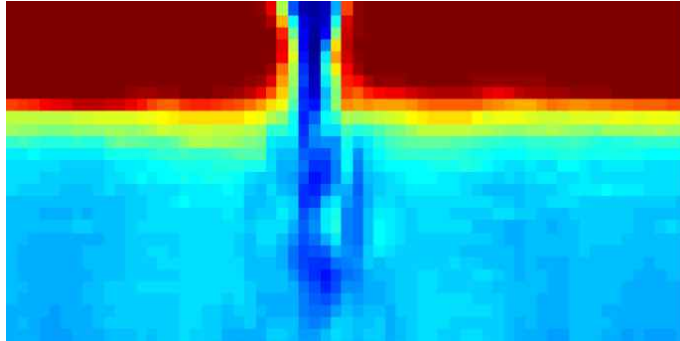
(b) original MARS analysis



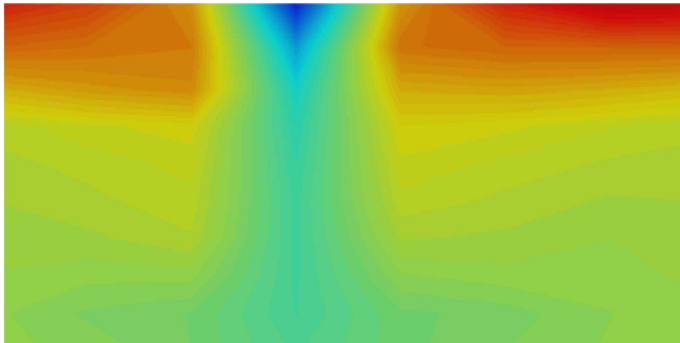
(c) modified MARS analysis

Figure 3.43 Comparison of the temperature distribution in the unwrapped downcomer at 60 seconds between the ROCOM test 2.2 and the MARS analysis (Kliem & Franz, 2012)

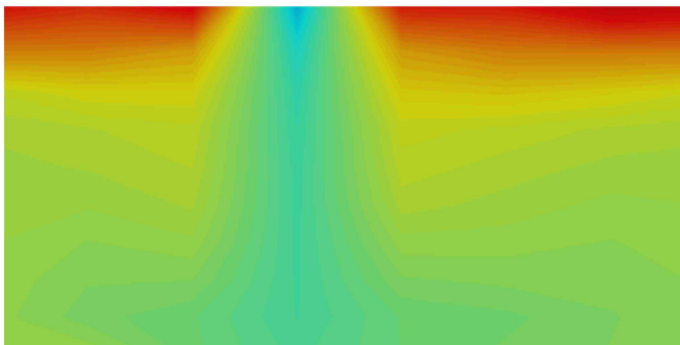
153.0 °C  236.1 °C



(a) ROCOM test 2.2

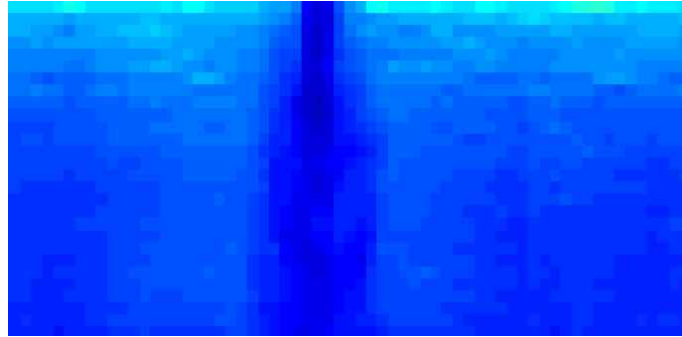


(b) original MARS analysis

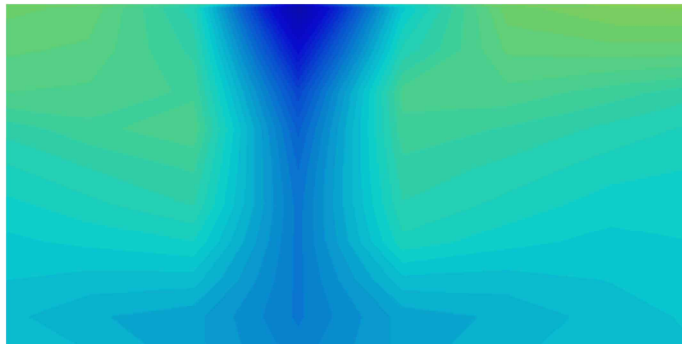


(c) modified MARS analysis

Figure 3.44 Comparison of the temperature distribution in the unwrapped downcomer at 90 seconds between the ROCOM test 2.2 and the MARS analysis (Kliem & Franz, 2012)



(a) ROCOM test 2.2

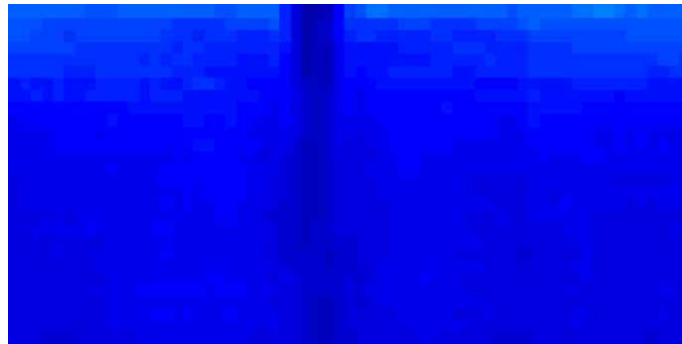


(b) original MARS analysis

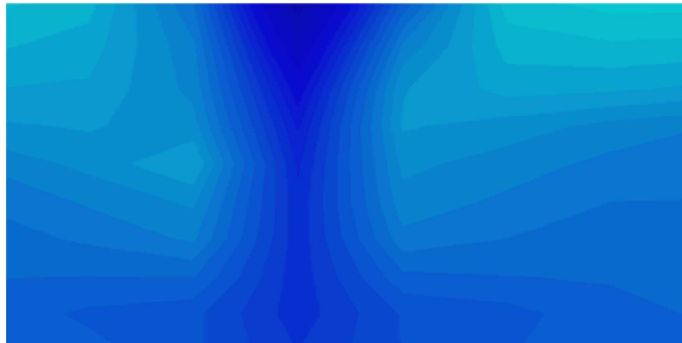


(c) modified MARS analysis

Figure 3.45 Comparison of the temperature distribution in the unwrapped downcomer at 120 seconds between the ROCOM test 2.2 and the MARS analysis (Kliem & Franz, 2012)



(a) ROCOM test 2.2



(b) original MARS analysis



(c) modified MARS analysis

Figure 3.46 Comparison of the temperature distribution in the unwrapped downcomer at 150 seconds between the ROCOM test 2.2 and the MARS analysis (Kliem & Franz, 2012)

## **Chapter 4**

# **Plant Applications of Jet Impingement Model**

The jet impingement model was developed to predict the multidimensional mixing behavior in the downcomer, and the modified MARS to apply the jet impingement model was validated with the test data produced by the SNUF, ATLAS, and ROCOM. Since these test facilities are scaled-down, it is required to confirm the influence of the jet impingement model at the prototype. Thus, additional analyses were carried out by simulating the DVI line break accident and the SLB accident in the APR1400.

### **4.1 APR1400 DVI Line Break Accident**

The ECC mixing behavior in the downcomer during the DVI line break accident in the APR1400 was estimated by utilizing MARS. The detailed simulation model and the analysis results are presented in following sub-sections.

#### **4.1.1 Simulation Model and Conditions**

The MARS modelling for the APR1400 was revised based on the one-

dimensional modeling which was prepared by KAERI (Euh et al., 2005) as shown in Fig. 4.1. The downcomer was modelled by MultiD component, and was divided into six (6) regions in the azimuthal direction. Along the vertical direction, the downcomer had ten (10) nodes. In this analysis, 50% DVI line break accident was simulated. The sequences and conditions of the trips in the prototype analysis are summarized in Table 4.1.

#### **4.1.2 Analysis Results and Insight**

The thermal power changed abruptly at approximately 30 seconds because of a low pressurizer pressure trip. Then it followed an exponential decay heat curve. In the pressure transient, as depicted in Fig. 4.2, the primary system pressure decreased until the secondary system pressure nearly equivalent to the primary system pressure at 40 seconds. It decreased negligibly from that time to approximately 200 seconds. During this period, the downcomer was filled with the liquid coolant before the loop seal clearing. After the loop seal clearing, the void of the upper downcomer increased, so that the break flow rate through the broken DVI nozzle attached in the upper downcomer decreased rapidly as illustrated in Fig. 4.3. And the core collapsed water level increased and the downcomer collapsed water level decreased as shown in Figs. 4.4 and 4.5, respectively.

The SI water was injected at around 70 seconds when the SIP was operated as presented in Fig. 4.6. In the analysis, the downcomer annulus was full of hot water, almost saturation temperature, at the time of SIP injection. After the cold water was injected into the upper downcomer, the azimuthal temperature stratification

was predicted by the original MARS as illustrated in Fig. 4.7 (a). However, when calculating the downcomer fluid temperature with the modified MARS code, the difference of the fluid temperature between the broken DVI side and injection DVI side decreased by applying the jet impingement model. The influence of the jet impingement model could be identified clearly by comparing the contour map of the downcomer fluid temperature. As shown in Fig. 4.8 (a), when analyzing with the original MARS, the ECC water fell down in the direction of gravity in an almost straight stream-line and reached the lower downcomer. However, degree of this tendency predicted by the original MARS decreased by applying the jet impingement model as illustrated in Fig. 4.8 (b). And the overall downcomer fluid temperature analyzed by the modified MARS was hotter than that analyzed by the original MARS.

The difference of the fluid temperature distribution in the downcomer was caused by the difference of the ECC water bypass ratio through the broken DVI nozzle. In the analysis, the ECC water bypass ratio could be estimated by tracking the boron injected into the downcomer. To track the boron, it was assumed that the initial boron concentration in Reactor Coolant System (RCS) was zero and the boron concentration of the SI water source was 3,000 ppm. And the ECC water bypass ratio was calculated by comparing the amount of the boron injected through the intact DVI nozzle and discharged from the broken DVI nozzle. The comparison of the boron bypass ratio between the results of the original MARS and the modified MARS is presented in Fig. 4.9.

In the modified MARS analysis, the ECC water injected into the DVI nozzle was well mixed in the upper downcomer region, so that the boron bypass ratio to the broken DVI nozzle was relatively high. However, in the analysis with the

original MARS code, the main flow direction of the injected ECC water was downward. Thus, the boron bypass ratio to the broken DVI nozzle was small compared to that analyzed by the original MARS as shown in Fig. 4.9. This difference of the boron bypass ratio influenced to the boron concentration in the core as illustrated in Fig. 4.10.

As described above, the mixing behavior in the downcomer during the DVI line break accident could influence to the boron concentration in the core as well as the temperature distribution in the downcomer. It means that the prediction capability of the mixing behavior in the downcomer is important for the nuclear safety. In terms of describing the boron concentration in the core and the fluid temperature distribution in the downcomer during the DVI line break accident, conservative analysis results was expected by adopting the jet impingement model.

## **4.2 APR1400 Steam Line Break Accident**

The SLB accident that assumed a break at the upstream of MSIV in the APR1400 was analyzed with the original and modified MARS code. The description of this accident, the detailed simulation model, and the analysis results are presented in following sub-sections.

### **4.2.1 Description of the Steam Line Break Accident**

The SLB accident causes an increase in steam flow from the secondary system. The increased heat removal induces the pressure and temperature drop in the

primary system for broken side loop. Due to the negative MTC, the reactivity is inserted into the core. Thus, the core power hits the Variable Over-Power Trip (VOPT) signal. In addition to the reactor trip, the turbine control and stop valves are closed. However, the steam flow through the broken steam line pipe continues to dry out the steam generator.

Because of the uncontrolled blowdown of the steam through the break, the steam generator pressure rapidly drops below the set point of the Main Steam Isolation Signal (MSIS). With the MSIS signal, the steam release from the intact steam generator loop is terminated. But the steam flow from the broken side is not terminated. In order to compensate the steam generator level, the feedwater are supplied from the Auxiliary Feedwater System (AFWS). The continued cooldown causes excessive energy removal from the steam generator and the RCS. This results in a decrease in reactor coolant temperatures in RCS, and causes an increase in core reactivity due to the negative MTC. If the core reactivity has a positive value, then it is possible to return to power and there is a potential for the degradation in fuel performance. Because of this characteristic of the SLB accident, it is important to predict the fluid temperature in the core appropriately. The temperature distribution in the core is influenced by the mixing behavior of the inlet coolant with the asymmetric temperature in the downcomer.

#### **4.2.2 Simulation Model and Conditions**

Since the coolant temperature distributions of the downcomer region and also the core region were important in this assessment, a multidimensional core, downcomer, and lower plenum modeling which was applied to the MARS

assessment for non-LOCA analysis (KAERI, 2009) was utilized. Figure 4.11 shows the schematic nodalization of the MARS modelling for the SLB accident simulation in the APR1400. The core and downcomer regions were modelled with separate MultiD components. One (1) radial and six (6) azimuthal grid numbers were used for downcomer. And three (3) radial and six (6) azimuthal grids were used for core part. The lower plenum provided the mixing of the coolants coming from broken and intact side loops, which was simulated with a MultiD component. Thus, when the coolant flowed up to the core region, the coolant temperature distribution could be investigated. The steam pipe line was splitted into two (2) different MSIV trains per steam generator. The SLB initiated by the rupture located at the upstream of the MSIV in steam generator A loop. The break area was set to  $0.238 \text{ m}^2$ . The low limit of the pressure for the main steam isolation signal was set as 855 psia.

### **4.2.3 Analysis Results and Insight**

The continued cooldown and associated shrinkage of the reactor coolant caused the pressurizer pressure to drop below the setpoint of the SI. The SI coolant contaminated with the high concentration of boron. Consequently, the addition of boron to the core would tend to reduce the reactivity in the core. In this analysis the SI water was injected at around 80 seconds, and the minimum temperature of the cold leg occurred at around 90 seconds after SLB as shown in Fig. 4.12. Therefore, the possibility of returning to power due to the negative MTC was high at around 90 seconds in this analysis.

As shown in Fig. 4.12, the maximum temperature difference (at around 90

seconds) of the cold legs between the broken side and the intact side was around 40 K in the original MARS analysis. This temperature difference decreased to around 25 K when analyzing with the modified MARS. It means that the inlet coolant with the asymmetric temperature mixed well in the downcomer by adopting the jet impingement model.

The influence of the jet impingement model could be also found by comparing the contour map of the downcomer and core fluid temperature as presented in Figs. 4.13 and 4.14, respectively. In particular, Fig. 4.14 shows the coolant temperature distributions in the core, obtained at the hot leg elevation, at the active core middle elevation, and at the active core bottom elevation. It was well described that the difference of the temperature between the broken and intact side was reduced by applying the jet impingement model.

Figure 4.15 presents the moderator reactivity as a function of the moderator temperature which was used for the SLB analyses in the APR1400 Standard Safety Analysis Report (KHNP, 2002). When performing the safety analysis regarding the SLB accident, the reactivity due to the negative MTC is calculated based on the average temperature of the broken side (half core) conservatively. In the same manner, the reactivity due to the negative MTC was calculated based on the average fluid temperature in the broken side at the middle elevation of the core analyzed by the original and modified MARS. The calculation results are illustrated in Fig. 4.16 and listed in Table 4.2. In the original MARS analysis, the average reactivity of the broken side due to the negative MTC was  $6.307\% \Delta\rho$ . Since the fluid temperature of the broken side core increased by applying the jet impingement model, the average reactivity due to the negative MTC was reduced to  $6.078\% \Delta\rho$  in the modified MARS analysis. In addition, the maximum local reactivity due to the negative MTC decreased from  $6.939\% \Delta\rho$  to  $6.537\% \Delta\rho$  when analyzing with the modified MARS. It means that the safety margin because of

the reactivity increased by adopting the jet impingement model.

As described above, the mixing behavior in the downcomer during the SLB accident could influence to the reactivity in the core as well as the temperature distribution. According to the analysis results, the reactivity difference was around  $0.2 \sim 0.4\% \Delta\rho$  between the original and modified MARS. When considering the safety margin of the APR1400 for the SLB accident is around  $0.2\% \Delta\rho$ , it can be concluded that MARS adopting incorporation of the jet impingement model strongly influences the safety analysis outcome.

Table 4.1 The sequences of trips in the APR1400 during the DVI line break accident

<b>Parameter</b>	<b>Time</b>	<b>Description</b>
Reactor trip	29.4	low pressurizer pressure ( $P < 10.72$ MPa)
Turbine trip	29.5	0.145 second after the reactor trip
RCP trip	29.9	0.50 second after the reactor trip
SI injection	68.3	40.0 seconds after the reactor trip
SIT injection	523.9	low pressure of the SIT inlet ( $P < 4.03$ MPa)

Table 4.2 The comparison of the reactivity due to the negative MTC during the SLB accident between the original and modified MARS analysis

<b>Reactivity due to the negative MTC</b>	<b>Original MARS</b>	<b>Modified MARS</b>	<b>Difference</b>
Average value of broken side, % $\Delta\rho$	6.307	6.078	-0.229
Maximum local value, % $\Delta\rho$	6.939	6.537	-0.402
<b>Difference</b>	+0.632	+0.459	+0.230



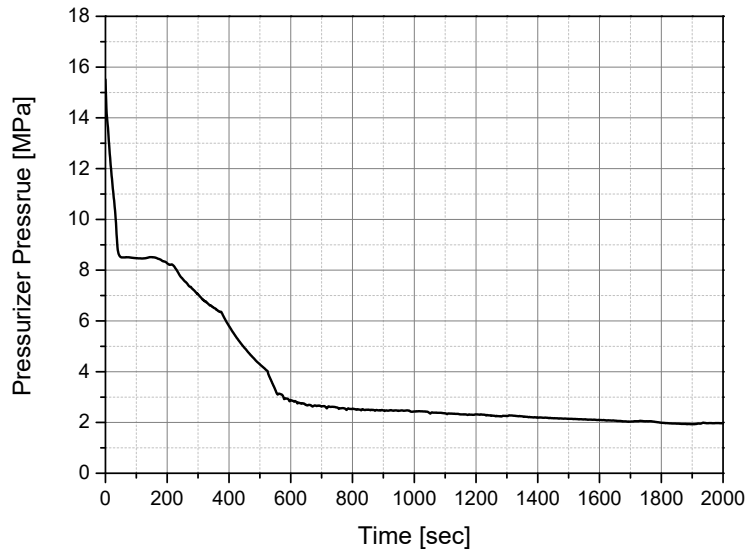


Figure 4.2 Pressurizer pressure during the DVI line break accident for the APR1400 (MARS analysis)

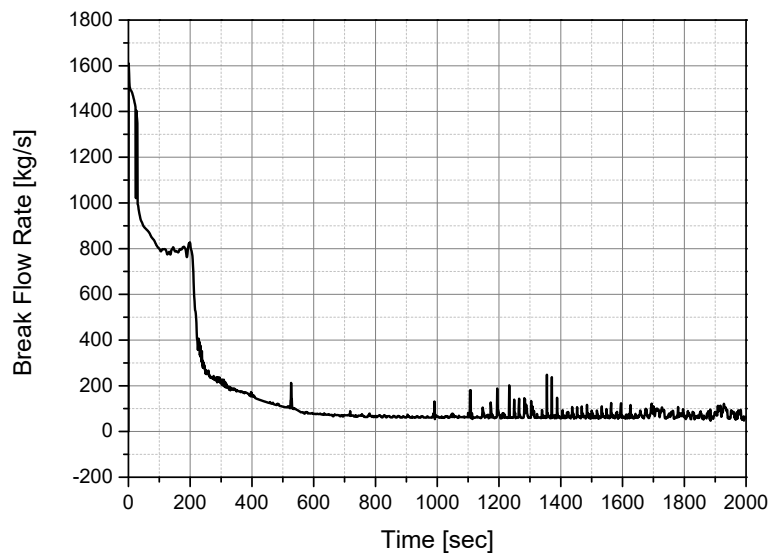


Figure 4.3 Break flow rate during the DVI line break accident for the APR1400 (MARS analysis)

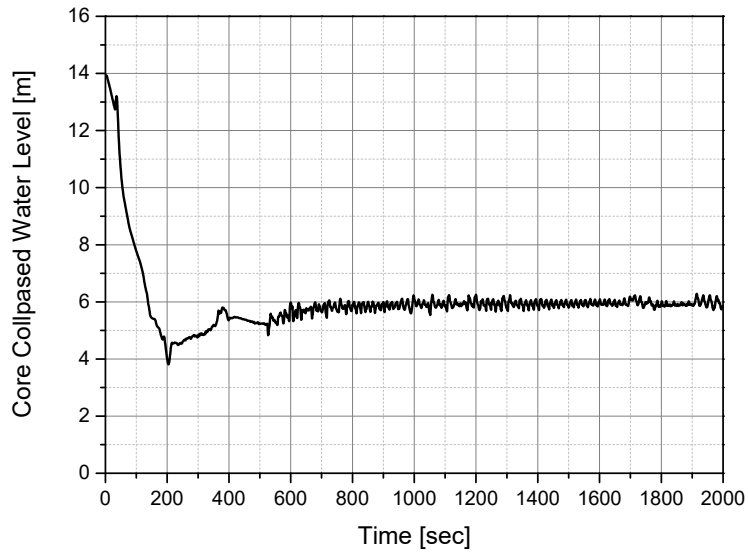


Figure 4.4 Core collapsed water level during the DVI line break accident for the APR1400 (MARS analysis)

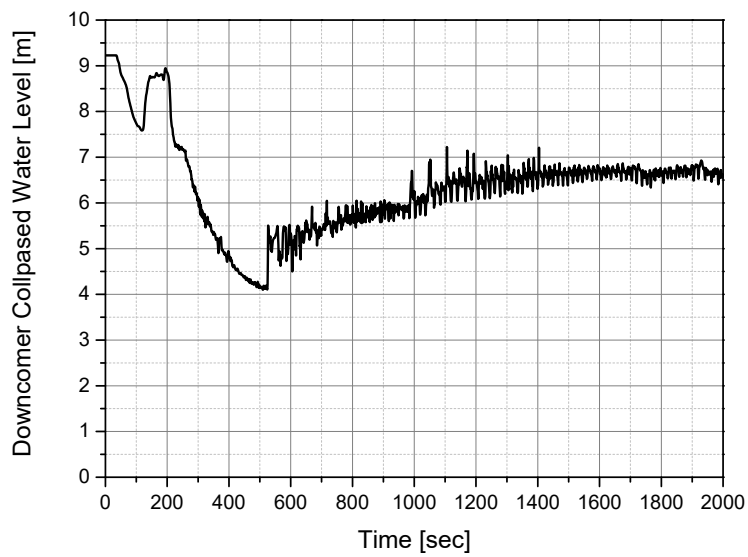


Figure 4.5 Downcomer collapsed water level during the DVI line break accident for the APR1400 (MARS analysis)

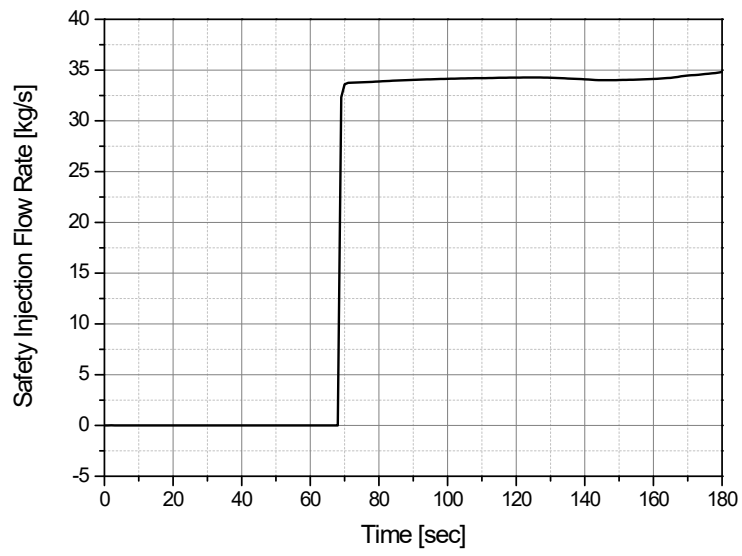
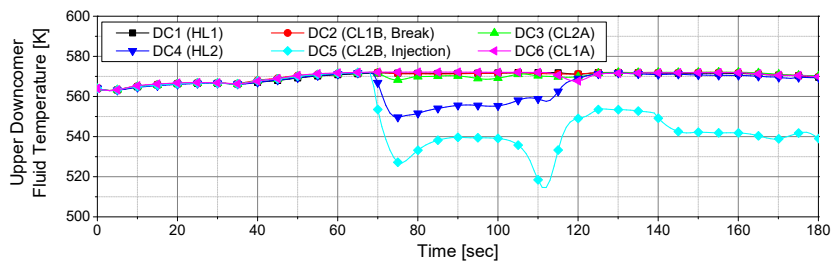
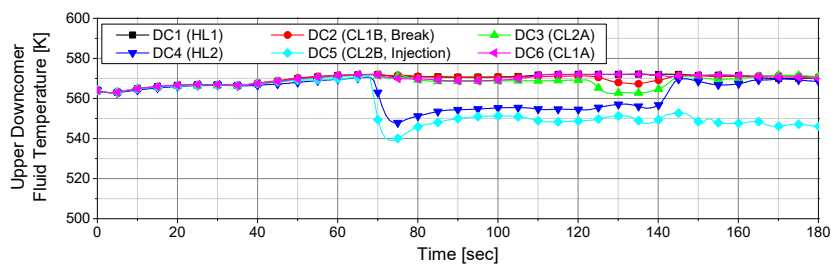


Figure 4.6 SI flow rate from the SIP during the DVI line break accident for the APR1400 (MARS analysis)

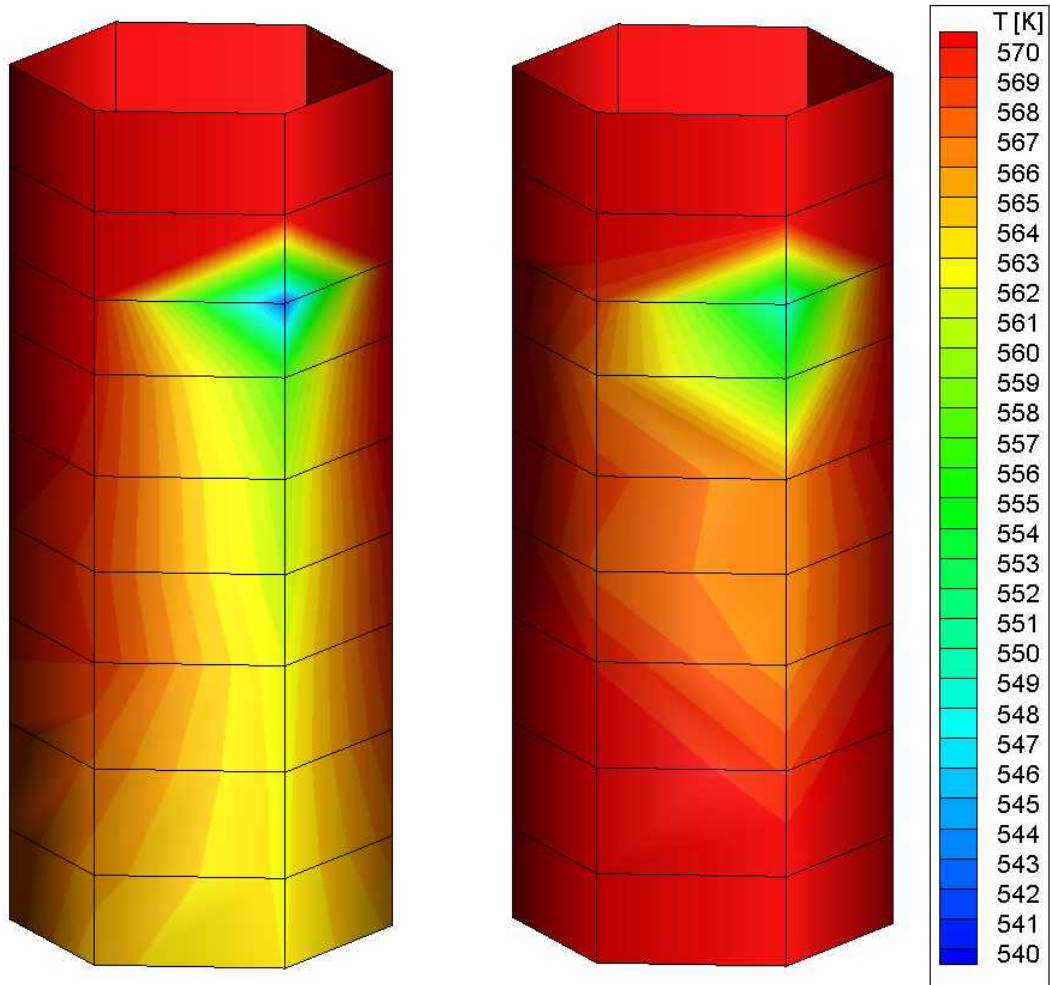


(a) original MARS analysis



(b) modified MARS analysis

Figure 4.7 Comparison of the upper downcomer fluid temperature during the DVI line break accident between the original and modified MARS analysis



(a) original MARS analysis

(b) modified MARS analysis

Figure 4.8 Comparison of the temperature distribution in the downcomer during the DVI line break accident at 150 seconds between the original and modified MARS analysis

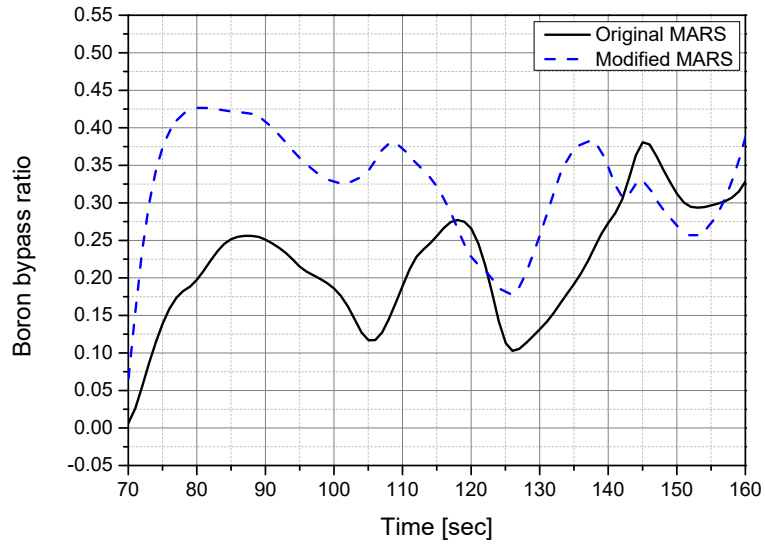


Figure 4.9 Comparison of the boron bypass ratio during the DVI line break accident between the original and modified MARS analysis

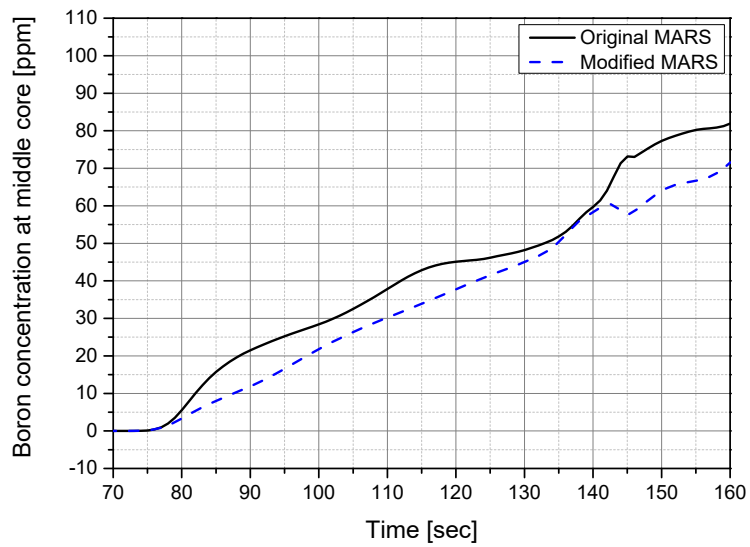


Figure 4.10 Comparison of the boron concentration in the core during the DVI line break accident between the original and modified MARS analysis

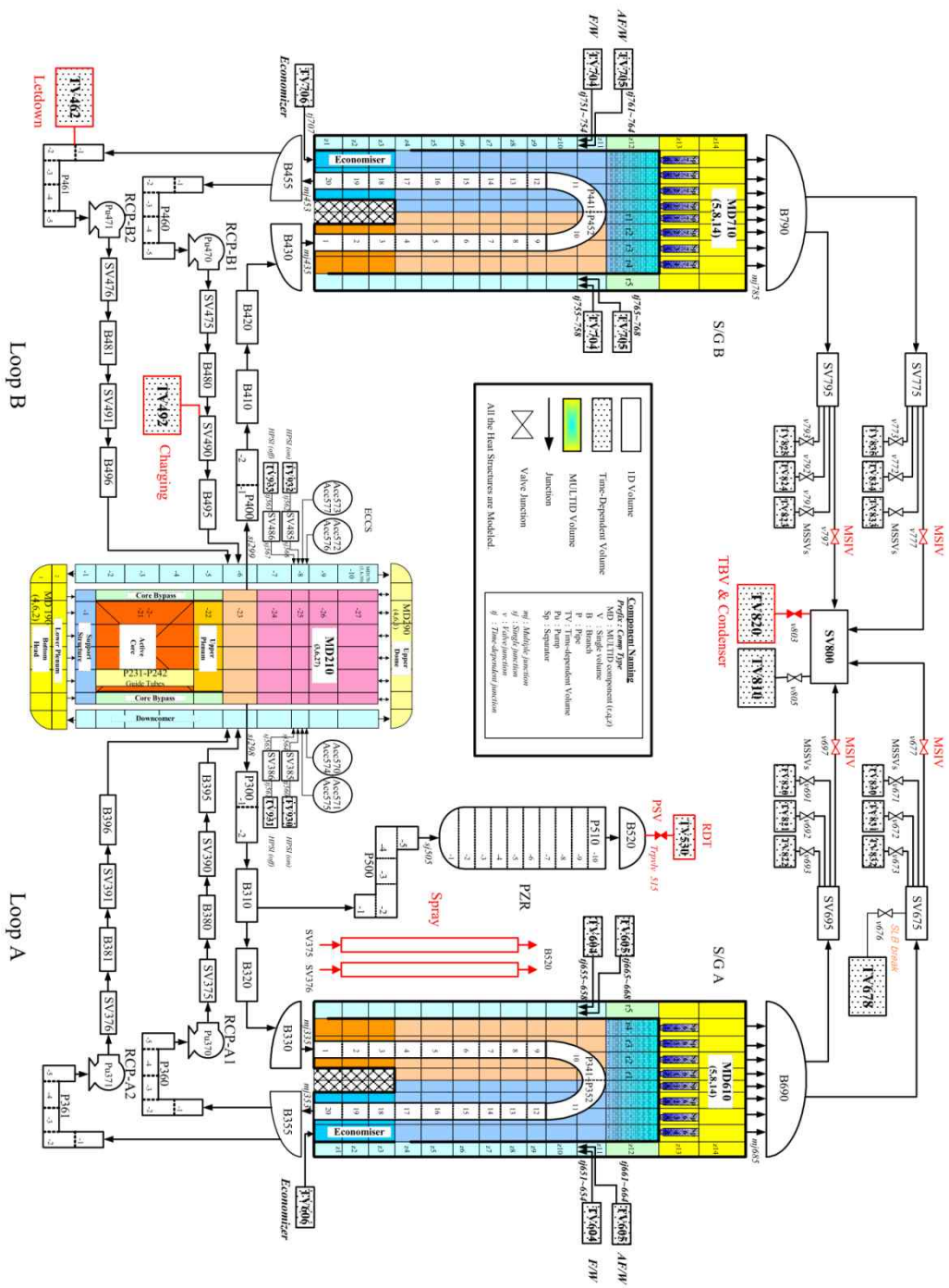


Figure 4.11 Schematic nodalization of the MARS model for the APR1400 (multidimensional core, downcomer, and steam generator model) (KAERI, 2009)

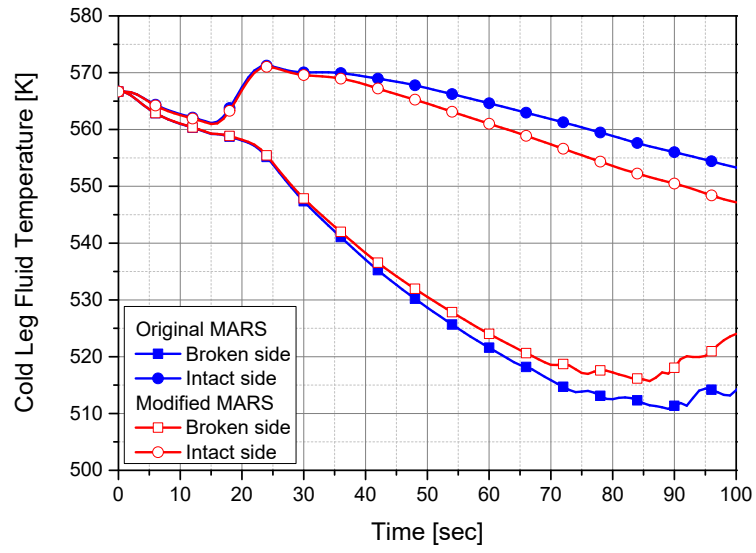
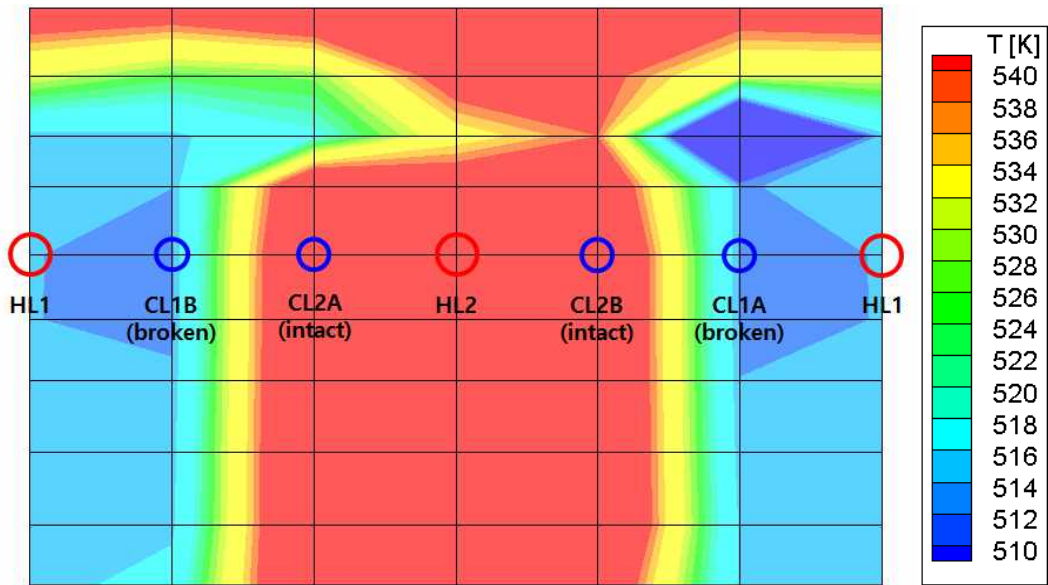
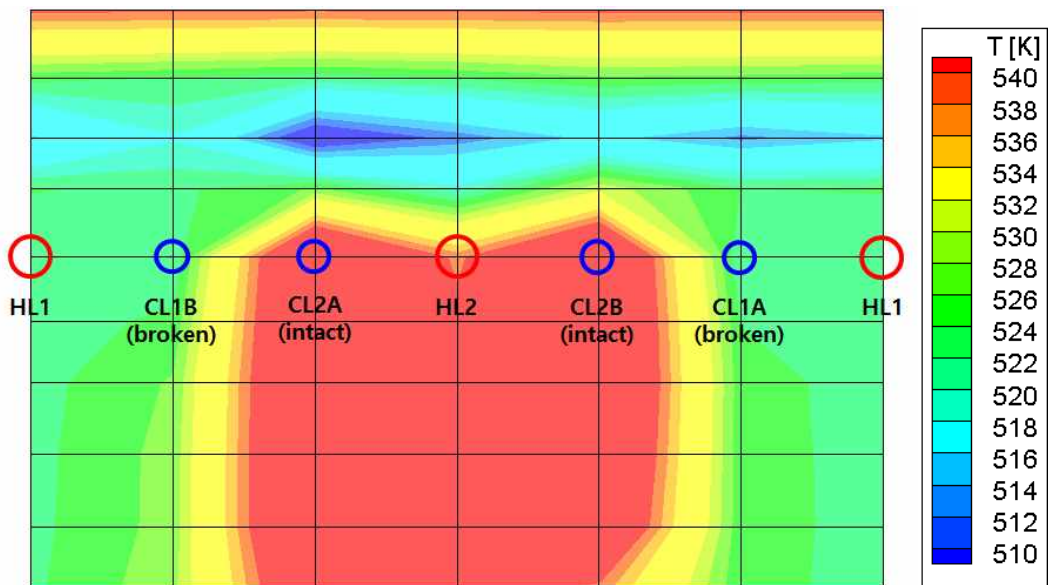


Figure 4.12 Comparison of the cold leg fluid temperature during the SLB accident between the original and modified MARS analysis



(a) original MARS analysis



(b) modified MARS analysis

Figure 4.13 Comparison of the temperature distribution in the downcomer during the SLB accident at 90 seconds between the original and modified MARS analysis

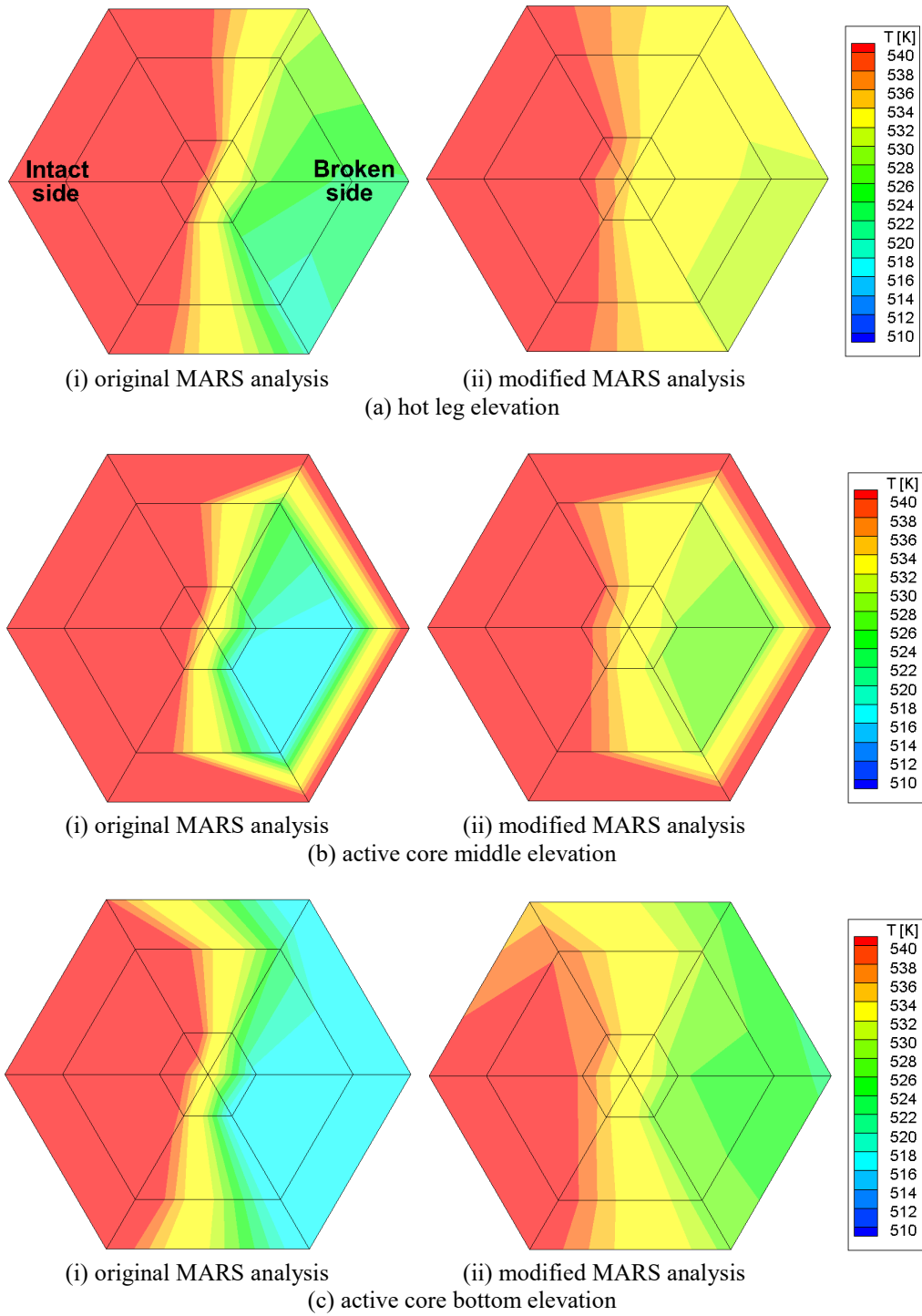


Figure 4.14 Comparison of the temperature distribution in the core during the SLB accident at 90 seconds between the original and modified MARS analysis

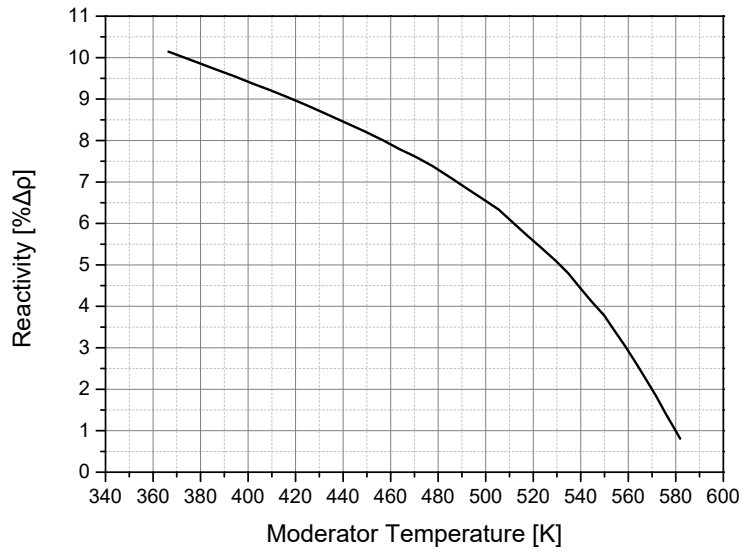
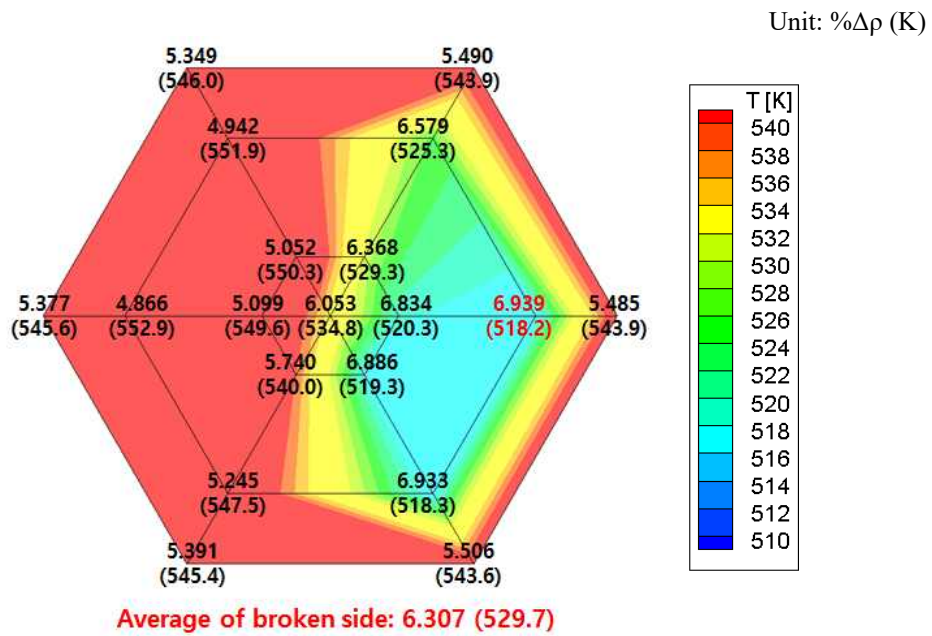
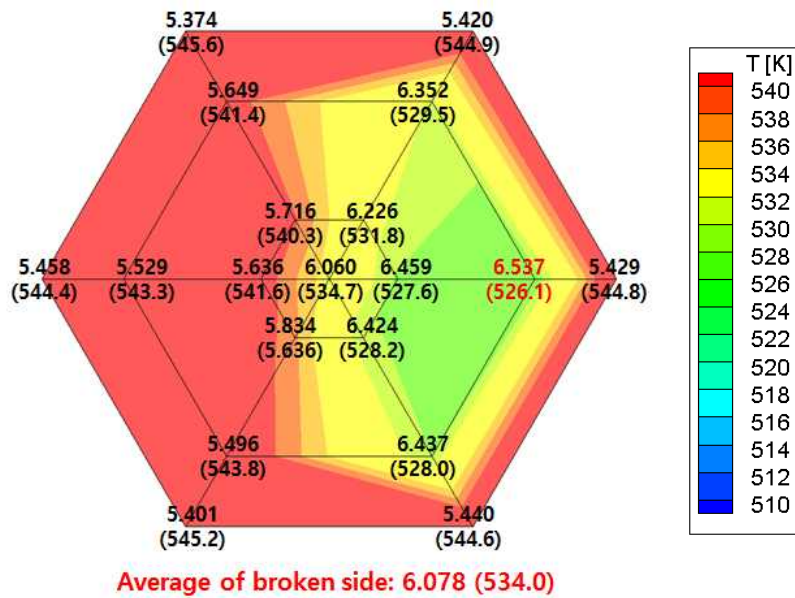


Figure 4.15 The moderator temperature reactivity vs. the temperature at post trip (KHNP, 2002)



(a) original MARS analysis



(b) modified MARS analysis

Figure 4.16 Comparison of the reactivity and fluid temperature distribution at the middle elevation of the core during the SLB accident at 90 seconds between the original and modified MARS analysis

# Chapter 5

## Conclusions

### 5.1 Summary

The APR1400 adopts a DVI system that injects SI water directly into the reactor vessel downcomer during accidents. Since the DVI nozzles are directly attached to the reactor vessel downcomer, complex thermal-hydraulic phenomena such as mixing are expected to occur in the downcomer region. To access the mixing phenomena, an experimental study was performed with an integral effect test facility, SNUF, which has a similar aspect ratio with the prototype, to observe the mixing behavior in the downcomer. According to the results of SNUF test, the ECC water mixed well in the downcomer annulus. However, the azimuthal temperature stratification in the downcomer was predicted by a best-estimate system code, MARS.

The cause of the limitation to predict the mixing behavior was figured out by investigating the jet impingement of the incoming flow and the momentum flux terms for one-dimensional connection. In MARS, the momentum flux terms are set to zero for the junction between the one-dimensional volume and three-dimensional cell of MultiD component because the axial and radial velocities are

small in the large three-dimensional region. However, if the nozzles are attached to the downcomer, which has a thin gap size, the axial and radial velocities are not small when the incoming orthogonal flow through the nozzles impinges against the downcomer wall. Therefore, it was required to consider the momentum flux terms induced by the impinging flow; for that, an appropriate jet impingement model to apply to the system code, MARS, was developed.

To develop the jet impingement model, CFD calculations were carried out. And the V2F turbulence model which had been widely known for well-accepted prediction of the jet impingement behavior was applied. The jet impingement model was formulated based on the CFD calculations with various conditions. The momentum flux term by the jet impingement phenomena was correlated with the diameter of the nozzle, the gap size of the downcomer, and the velocity of the incoming flow. This model was applied to MARS by considering the momentum flux term for the junctions connected in three-dimension. The modified MARS with the jet impingement model was validated with the results from SNUF and ATLAS tests and showed good agreements with the test data. Additionally, the test data of ROCOM was also used to validate the prediction capability of the modified MARS for the inlet coolant with the asymmetric temperature during a transient such as the SLB accident.

For plant application, the ECC mixing behavior in the downcomer during a postulated DVI line break accident in the APR1400 was estimated by utilizing the MARS. And it was found that more vigorous mixing in the downcomer was predicted by the modified MARS code, and the boron bypass ratio through the broken DVI nozzle estimated by the modified MARS code was larger than that estimated by the original unmodified MARS code. And the SLB accident that

assumed a break at the upstream of the MSIV in APR1400 was analyzed with MARS. Since the coolant temperature distributions of not only the downcomer region but also the core region are important in this assessment, a multidimensional core, downcomer, and lower plenum modeling was utilized. And the reactivity due to the negative MTC was estimated according to the local fluid temperature in the core to identify the mixing effect of the jet impingement model during the SLB accident. According to the analysis results, the reactivity difference was around  $0.2 \sim 0.4\% \Delta\rho$  between the original MARS and modified MARS. When considering the safety margin of the APR1400 for the SLB accident is around  $0.2\% \Delta\rho$ , the adoption of the jet impingement model in MARS can significantly influence the safety analysis outcome.

The jet impingement model applied to MARS can provide improved prediction of the mixing behavior in downcomer annulus. This study provides the approach to the prediction of the multidimensional liquid phase mixing phenomenon occurring in the downcomer using the system code. And it is expected that the results of this study will influence the safety analysis regarding an asymmetric coolant temperature such as the SLB accident.

## **5.2 Recommendations**

Through the present study the following further studies are suggested:

### **Turbulence Model for System Code**

In MARS, a simple Prandtl's mixing length model is applied for the

implementation of turbulent viscosity in the momentum diffusion term and the thermal mixing term. However, when modelling the downcomer three-dimensionally, the mixing behaviors can be influenced by which turbulence model is applied. Therefore, efforts to apply the additional turbulence model into MARS can be a method to extend the prediction capability of the mixing phenomenon. For example, the Prandtl's mixing length model and the k- $\epsilon$  model can be chosen as an option in GOTHIC (EPRI, 2006).

### **Benchmarking of Other System Codes**

In MARS, the momentum flux terms are set to zero for the junction between the one-dimensional volume and three-dimensional cell of MultiD component. However, there are some approaches to transfer the momentum from one-dimensional volume to three-dimensional cell according to the other system codes. For TRACE 5.0 code (U.S. NRC, 2012), it is assumed that the interface flow area and velocity are defined on the opposite side of the three-dimensional cell from the interface where the one-dimensional component junction source convection is made. On the other hand, in the GOTHIC code (EPRI, 2006), the user can specify a momentum transport option for each junction to include the momentum flux terms. These approaches of other system codes cannot be applied to MARS in the same manners. However, efforts to consider the momentum flux terms between the one-dimensional volume and three-dimensional cell of MultiD component in MARS are required.

### **Multidimensional Phenomena in Downcomer**

This study focused on the multidimensional liquid phase mixing behavior in a

downcomer annulus before the loop seal clearing. Thus, the prediction capability of MARS was improved by applying the jet impingement model. However, various multidimensional phenomena in the downcomer were not predicted perfectly with the system codes until now. For example, the downcomer collapsed water level after the loop seal clearing during the small break LOCA including the DVI line break accident has been not predicted appropriately with the system codes. Therefore, additional studies are required to understand the multidimensional phenomenon exactly.

# Nomenclature

$A$	Area [ $\text{m}^2$ ]
$d$	Diameter [m]
$Fr$	Froude number
$f$	Function
$G$	Mass Flux [ $\text{kg m}^{-2}\text{s}^{-1}$ ]
$g$	Gravitational acceleration [ $\text{m s}^{-2}$ ]
$h$	Enthalpy [ $\text{J kg}^{-1}$ ], local momentum boundary layer thickness [m]
$\bar{h}$	Mean enthalpy in system [ $\text{J kg}^{-1}$ ]
$l$	Length [m]
$M$	Mass [kg]
$\dot{m}$	Flow rate [ $\text{kg s}^{-1}$ ]
$P$	Pressure [Pa]
$Q$	Thermal power [W]
$r$	Radial coordinate measured from stagnation point [m]
$Re$	Reynolds number
$s$	Height of downcomer [m]
$T$	Temperature [K]
$t$	Time [s], Downcomer gap size [m]
$u$	x-direction velocity [ $\text{m s}^{-1}$ ], local mean velocity in radial direction [ $\text{m s}^{-1}$ ]
$\bar{u}$	x-direction average velocity [ $\text{m s}^{-1}$ ]
$V$	Velocity of incoming flow [ $\text{m s}^{-1}$ ], Volume [ $\text{m}^3$ ]
$v$	y-direction velocity [ $\text{m s}^{-1}$ ]

$\bar{v}$	y-direction average velocity [ $\text{m s}^{-1}$ ]
$w$	z-direction velocity [ $\text{m s}^{-1}$ ]
$\bar{w}$	z-direction average velocity [ $\text{m s}^{-1}$ ]
$x$	x-direction
$y$	y-direction
$z$	z-direction, Axial coordinate measured from the impingement wall [m]

### *Greek Letters*

$\alpha$	Void fraction
$\Delta$	Difference
$\eta$	Dimensionless axial coordinate measured from wall
$\Theta$	Mixing scalar
$\rho$	Density [ $\text{kg m}^{-3}$ ]
$\sigma$	Conductivity [ $\text{S m}^{-1}$ ]
$\tau$	Time scale [s]

### *Subscripts*

$0$	Initial value
$a$	Ambient water in downcomer
$avg$	Average value
$C$	Core

<i>c</i>	Critical
<i>CL</i>	Cold leg
<i>D</i>	Discharged flow
<i>f</i>	Liquid
<i>g</i>	Gas
<i>HL</i>	Hot leg
<i>in</i>	Incoming flow
<i>K</i>	Upward volume
<i>L</i>	Downward volume
<i>m</i>	Mean value
<i>n</i>	Normalized value
<i>out</i>	Discharged flow
<i>p</i>	Primary system
<i>R</i>	Scaling ratio
<i>s</i>	Secondary system
<i>sat</i>	Saturation
<i>SI</i>	Safety injection

*Superscripts*

\* Non-dimensional value

## References

American Nuclear Society (1979), "Decay Heat Power in Light Water Reactor," ANSI/ANS 5.1 (1979).

Azuma, T., and Hoshino, T., "LDV Measurement in Radial Flow of Thin Liquid Film," In *Proceedings of the Osaka Symposium on Flow Measuring Techniques: The Application of LDV*, Association for the Study of Flow Measurements, Osaka, Japan, pp. 1-15 (1983).

Bae, B. U. et al., "Scaling Methodology for a Reduced-Height Reduced-Pressure Integral Test Facility to Investigate Direct Vessel Injection Line Break SBLOCA," *Nuclear Engineering and Design*, **238**, pp. 2197-2205 (2008).

Baek, W. P. et al., "KAERI Integral Effect Test Program and the ATLAS Design," *Nuclear Technology*, **152**, pp. 193-195 (2005).

Behnia, M. et al., "Prediction of Heat Transfer in an Axisymmetric Turbulent Jet Impinging on a Flat Plate," *Int. J. Heat Mass Transfer*, **41(12)**, pp. 1845-1855 (1998).

Beltaos, S., and Rajaratnam, N., "Impinging Circular Turbulent Jets," *Journal Hydraulic Division*, ASCE **100**, pp. 1313-1328 (1974).

Baughn, J., and Shimizu, S., "Heat Transfer Measurements from a Surface with Uniform Heat Flux and an Impinging Jet," *Journal of Heat Transfer*, **111**, pp.

1096-1098 (1989).

Baughn, J. et al., "An Experimental Study of Entrainment Effects on the Heat Transfer from a Flat Surface to a Heated Circular Impinging Jet," *Journal of Heat Transfer*, **113**, pp. 1023-1025 (1991).

Choi, K. Y. et al., "Simulation Capability of the ATLAS Facility for Major Design-Basis Accidents," *Nuclear Technology*, **156**, pp. 256-269 (2006).

Choi, K. Y. et al., "Experimental Simulation of a Direct Vessel Injection Line Break of the APR1400 with the ATLAS," *Nuclear Engineering and Technology*, **41**, pp. 655-676 (2010).

Choi, K. Y. et al., "Effects of Break Size on DVI Line Break Accidents of the ATLAS," *Nuclear Technology*, **175**, pp. 604-618 (2011).

Cooper, D. et al., "Impinging Jet Studies for Turbulence Model Assessment - I. Flow-Field Experiments," *Int. J. Heat Mass Transfer*, **36(10)**, pp. 2675-2684 (1993).

Craft, T. J. et al., "Impinging Jet Studies for Turbulence Model Assessment – II. An Examination of the Performance of Four Turbulence Models," *Int. J. Heat Mass Transfer*, **36(10)**, pp. 2685-2697 (1993)

Durbin, P., "Separated Flow Computations with the  $k-\epsilon-v^2$  Model," *AIAA Journal*, **33(4)**, pp. 659-664 (1995).

Electric Power Research Institute (EPRI), "EPRI Utility Requirement Documents

for the Advanced Light Water Reactor (Chapter 15)" (1995).

Electric Power Research Institute (EPRI), "GOTHIC Containment Analysis Package Technical Manual, Version 7.2a (QA)" (2006).

Esch, T. et al., "Heat Transfer Predictions Based on Two-Equation Turbulence Models," TED Paper AJ03-542 (2003).

Euh et al., "DVI-line break LOCA Analysis of the ATLAS-An Integral Effect Test Loop for Pressurized Water Reactors," In *Proceedings of the 11th International Topical Meeting on Nuclear Reactor Thermal Hydraulics (NURETH-11)*, Avignon, France, October 2-6 (2005).

Henry, R. E., and Fauske, H. K., "The Two-Phase Critical Flow of One-Component Mixtures in Nozzles, Orifices, and Short Tubes," *Journal of Heat Transfer*, pp. 179 (1971).

Höhne, T. et al., "Modeling of a Buoyancy-Driven Flow Experiment at the ROCOM Test Facility Using the CFD Codes CFX-5 and Trio\_U," *Nuclear Engineering and Design*, **236**, pp. 1309-1325 (2006).

Höhne, T., and Kliem, S., "Modeling of a Buoyancy-Driven Flow Experiment in Pressurized Water Reactors Using CFD-Methods," *Nuclear Engineering and Technology*, **39(4)**, pp. 327-336 (2007).

Kim, Y. S. et al., "Experiments and MAAP4 Assessment for Core Mixture Level Depletion after Safety Injection Failure during Long-Term Cooling of a Cold Leg LBLOCA," *Nuclear Engineering and Technology*, **235(2)**, pp. 91-107 (2003).

Kim, Y. S. et al., "RELAP5/MOD3.3 Analysis of Coolant Depletion Tests after Safety Injection Failure during a Large-Break Loss-of-Coolant Accident," *Nuclear Engineering and Design*, **235**, pp. 2375-2390 (2005).

Kim, Y. S. et al., "First ATLAS Domestic Standard Problem (DSP-01) for the Code Assessment," *Nuclear Engineering and Technology*, **43**, pp. 25-44 (2011).

Kliem, S. et al., "Experiments at the Mixing Test Facility ROCOM for Benchmarking of CFD Codes," *Nuclear Engineering and Design*, **238**, pp. 566 – 576 (2008).

Kliem, S., and Franz, R., "Quick-look Report of the ROCOM Test 1.3, 2.1 and 2.2 Conducted within the OECD PKL2 Project," Institute Report HZDR\FWO\2012\02, Helmholtz Zentrum Dresden Rossendorf (2012).

Korea Atomic Energy Research Institute (KAERI), "MARS Code Manual, Volume IV: Developmental Assessment Report," KAERI/TR-3042/2005 (2009).

Korea Atomic Energy Research Institute (KAERI), "MARS Code Manual, Volume I: Code Structure, System Models, and Solution Methods," KAERI/TR-2812/2004 (2009).

Korea Hydro & Nuclear Power (KHNP), "Standard Safety Analysis Report for APR1400," (2002).

Korea Institute of Nuclear Safety (KINS), "MARS-KS Code Manual, Volume II: Input Requirements," KINS/RR-1282, Rev. 1 (2016).

Kucukboyaci, V. et al., "COBRA-TF Parallelization and Application to PWR Reactor Core Subchannel DNB Analysis," In *Joint International Conference on Mathematics and Computation (M&C), Supercomputing in Nuclear Application (SNA) and the Monte Carlo (MC) Method*, Nashville, TN, USA, April 19-23 (2015).

Kurki, J., "Modeling of ROCOM Mixing Test 2.2 with TRACE v5.0 Patch 3," U.S. NRC, NUREG/IA-0454 (2015).

Lee, K. H. et al., "An Integral Loop Test and MARS Code Analysis for a DVI Line Break LOCA in the APR1400," *Nuclear Engineering and Design*, **238**, pp. 3336-3347 (2008).

Lee, K. H., "An Experimental and Analytical Study for a DVI Line Break LOCA in the Advanced Power Reactor 1400 MWe," M.A. Thesis, Seoul National University (2008).

Lee, S. W., and Chung, B. D., "Preliminary Assessment of MARS-KS for ROCOM Test-1," In *Korean Nuclear Society Spring Meeting*, Jeju, Korea, May 17-18 (2012).

Liu, X., and Lienhard, J. H., "Liquid Jet Impingement Heat Transfer on a Uniform Flux Surface," In *Proceedings of the 1989 National Heat Transfer Conference*, HTD, **106**, pp. 523-530 (1989).

Lytle, D., and Webb, B., "Air Jet Impingement Heat Transfer at Low Nozzle-plate Spacings," *Int. J. Heat Mass Transfer*, **37(2)**, pp. 1687-1697 (1994).

Martin, H., "Heat and Mass Transfer between Impinging Gas Jets and Solid Surfaces," *Advances in Heat Transfer*, **13**, pp. 1-60 (1977).

Montgomery, R., "VERA Tools and Workflows," CASL Technical Report: CASL-U-2014-0054-001 (2014).

Nakoyakov, V. E. et al., "Impingement of an Axisymmetric Liquid Jet on a Barrier," *Int. J. Heat Mass Transfer*, **21**, pp. 1175-1184 (1978).

Organization for Economic Cooperation and Development / Nuclear Energy Agency (OECD/NEA), "International Standard Problem No. 50, ATLAS Test, SB-DVI-09: 50% (6-inch) Break of DVI line of the APR1400, Final Integration Report," NEA/CSNI/R (2012).

Olsson, R. G., and Turkdogan, E. T., "Radial Spread of a Liquid Stream on a Horizontal Plate," *Nature*, **211**, pp. 813-816 (1966).

Rohde, U. et al., "Fluid Mixing and Flow Distribution in the Reactor Circuit, Measurement Data Base," *Nuclear Engineering and Design*, **235**, pp. 421-443 (2005).

Stevens, J., and Webb, B. W., "Measurements of the Free-Surface Flow Structure under an Impinging Free Liquid Jet," *ASME J. Heat Transfer*, **114**, pp. 79-84 (1992).

Stevens, J., and Webb, B. W., "Measurements of Flow Structure in the Radial Layer of Impinging Free-Surface Liquid Jets," *Int. J. Heat Mass Transfer*, **36(15)**, pp. 3751-3758 (1993).

Thurgood, M. J., et al., "COBRA-TF: A Thermal-hydraulics Code for Transient Analysis of Nuclear Reactor Vessel and Primary Coolant Systems," U.S. NRC, NUREG/CR-3046 (1983).

Thomas, S. et al., "The Flow of a Thin Liquid Film on a Stationary and Rotating Disk - Part I: Experimental Analysis and Flow Visualization," In *Heat Transfer in Space Systems*, HTD, **135**, pp. 125-133 (1990).

U.S. Nuclear Regulatory Commission (NRC), "TRACE V5.0 User's Manual" (2012).

U.S. Nuclear Regulatory Commission (NRC), "RELAP5 Code Manual" (1999).

Watson, E. J., "The Radial Spread of a Liquid Jet over a Horizontal Plane," *J. Fluid Mech.*, **20**, pp. 481-499 (1964).

Yan, X. et al., "The Effect of Reynolds Number on the Heat Transfer Distribution from a Flat Plate to an Impinging Jet," *ASME HTD*, **226**, pp. 1-7 (1992).

Yan, X., "A Preheated-wall Transient Method Using Liquid Crystals for the Measurement of Heat Transfer on External Surfaces and in Ducts," Ph.D. Thesis, University of California (1993).

Zuckerman, N., and Lior, N., "Impingement Heat Transfer Correlation and Numerical Modeling," *Journal of Heat Transfer*, **127(5)**, pp. 544-552 (2005).

Zuckerman, N., and Lior, N., "Radial Slot Jet Impingement Flow and Heat Transfer on a Cylindrical Target," *Journal of Thermophysics and Heat Transfer*,

**21(3)**, pp. 548-560 (2007).

## Appendix A.

### Modification of MARS Code

The jet impingement model developed in this study was applied into the MARS-KS 1.3 version. The modular structures of MARS are shown in Fig. A.1. Among the modules presented in Fig. A.1, HydroSolve module includes VelocityExplicit subroutine. This subroutine computes the explicit liquid and vapor velocities, the pressure gradient coefficients needed for the implicit pressure solution, and the old-time source terms for the mass and energy equations. And the liquid momentum flux (*convfs* term) are considered with following formula in this subroutine:

$$psl = pum\ ph - convfs - convgs - delpza \quad (A.1)$$

where, *pumph* term is the pump head, *convgs* term is vapor momentum flux, and *delpza* term is the gravity. The momentum flux calculated by the jet impingement model based on Eq. (3.11) and the application criterion described in Table 3.1 was applied into the *convfs* term. The overall calculation process to apply the jet impingement model is like Fig. A.2. And the source of MARS for the jet impingement model is presented in Table A.1.

Table A.1 The source code to apply the jet impingement model

<b>Main body</b>
<pre> INTEGER fj0,ddf0,sdf0,fmt0,fvf0 REAL(8) impmf1,impmf2,impmr,impmh,impmd,impms,impmhmin,impmrho,impbm,impbv psld(ih1)=pmpph(ix)-convfs(ih1)-convgs(ih1)-delpza impmf2=convfs(ih1) DO fj0=1_da(issys)%iJunLoop(2),l_da(issys)%iJunLoop(2)+1_da(issys)%nJunLoop(2)-1   IF(j_da(fj0)%isOned) then     IF((j_da(fj0)%idxFrom(2).eq.k.and.j_da(fj0)%Vfj&lt;0.0.and. &amp;       (mod(j_da(fj0)%volFrom(2),10).eq.4.or.mod(j_da(fj0)%volFrom(2),10).eq.3)).or. &amp;       (j_da(fj0)%idxTo(2).eq.k.and.j_da(fj0)%Vfj&gt;0.0.and. &amp;       (mod(j_da(fj0)%volTo(2),10).eq.4.or.mod(j_da(fj0)%volTo(2),10).eq.3))) then       <b>Calculate momentum flux term</b>     ENDIF     IF((j_da(fj0)%idxFrom(2).eq.l.and.j_da(fj0)%Vfj&lt;0.0.and. &amp;       (mod(j_da(fj0)%volFrom(2),10).eq.4.or.mod(j_da(fj0)%volFrom(2),10).eq.3)).or. &amp;       (j_da(fj0)%idxTo(2).eq.l.and.j_da(fj0)%Vfj&gt;0.0.and. &amp;       (mod(j_da(fj0)%volTo(2),10).eq.4.or.mod(j_da(fj0)%volTo(2),10).eq.3))) then       <b>Calculate momentum flux term</b>     ENDIF   ENDIF ENDDO </pre>
<b>Calculation of Froude number</b>
<pre> impmd=sqrt(j_da(fj0)%AJUN/pi)*2.0 impmhmin=impmd**0.82*(v_da(k)%AREA(3)/v_da(k)%LENGTH(1))**0.18 IF(v_da(k)%jface(6)&gt;0.and.v_da(k)%jface(5)&gt;0) then   fmt0=j_da(v_da(k)%jface(6))%idxto(2)   fvf0=j_da(v_da(k)%jface(5))%idxfrom(2) ELSE   fmt0=-1   fvf0=-1 ENDIF IF(fmt0&gt;0.and.fvf0&gt;0) then   impbm=(v_da(fmt0)%rho*f*v_da(fvf0)%voidf+v_da(fvf0)%rho*g*v_da(fmt0)%voidg)*v_da(fmt0)%V+ &amp;     (v_da(fvf0)%rho*f*v_da(fvf0)%voidf+v_da(fvf0)%rho*g*v_da(fvf0)%voidg)*v_da(fvf0)%V+ &amp;     (v_da(k)%rho*f*v_da(k)%voidf+v_da(k)%rho*g*v_da(k)%voidg)*v_da(k)%V   impbv=v_da(fmt0)%V+v_da(fvf0)%V+v_da(k)%V   impmrho=(j_da(fj0)%rho*fj-impbm/impbv)/j_da(fj0)%rho*fj ELSE   impmrho=-1.0 ENDIF </pre>
<b>Calculation of momentum flux term</b>
<pre> IF(impmrho&gt;0.0.and.ABS(j_da(fj0)%Vfj)/SQRT(9.81*impmhmin*MAX(impmrho,0.000001))&gt;1.3) then   impmf1=MIN((ABS(j_da(fj0)%Vfj)/SQRT(9.81*impmhmin*MAX(impmrho,0.000001))-1.3)/1.2,1.0)   IF(v_da(k)%jface(6).eq.i) then     impms=0.0     sdf0=0     Do ddf0=1,100       impmr=sqrt((v_da(k)%Length(1)*0.5-v_da(k)%Length(1)*ddf0/100.0)**2 &amp;         +(v_da(k)%Length(3)*0.5)**2)       impmh=0.027/(v_da(k)%AREA(3)/v_da(k)%LENGTH(1))*(impmr-3.5*impmd**0.34* &amp;         (v_da(k)%AREA(3)/v_da(k)%LENGTH(1))**0.66)**2+0.095*impmhmin       IF(impmh&gt;v_da(k)%AREA(3)/v_da(k)%LENGTH(1)) then         impmh=v_da(k)%AREA(3)/v_da(k)%LENGTH(1)         sdf0=sdf0+1       ENDIF       impms=impms+(impmd**2*v_da(k)%Length(3)/16.0/impmr**2/impmh)**2 &amp;         *impmh/(v_da(k)%AREA(3)/v_da(k)%LENGTH(1))/100.0     END DO     IF(sdf0&lt;100.and.j_da(fj0)%voidfj&gt;0.9) then       psld(ih1)=psld(ih1)+impmf2+0.5*j_da(fj0)%voidfj*j_da(fj0)%rho*fj*j_da(fj0)%Vfj**2*impms*impmf1       impmf2=0.0     ENDIF   ENDIF   <b>Calculate axial direction momentum flux term</b> ENDIF </pre>

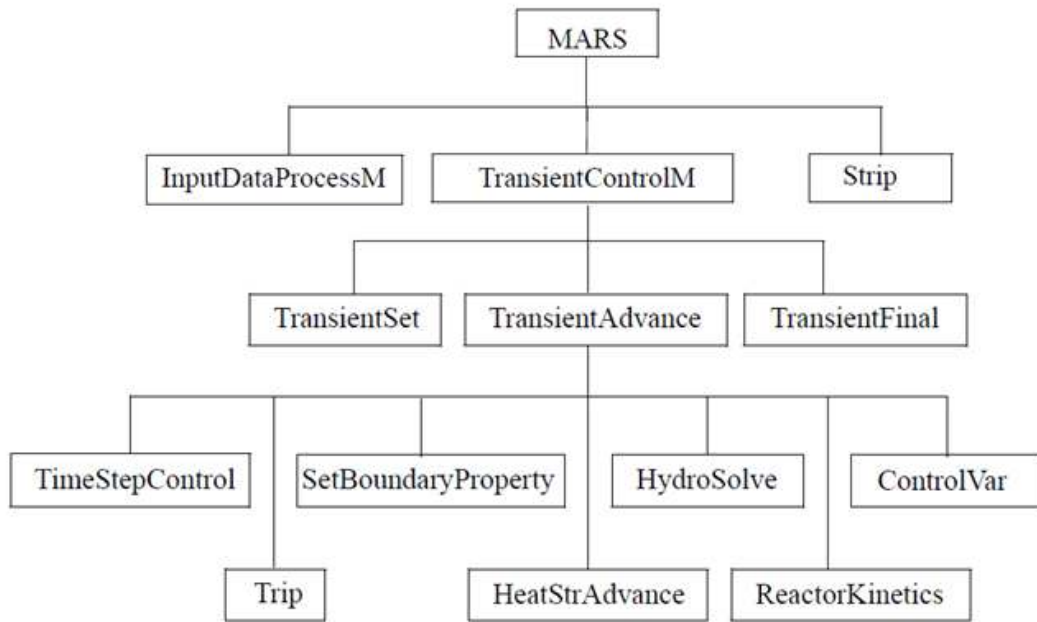


Figure A.1 Modular structures of transient calculation in MARS (KAERI, 2009)

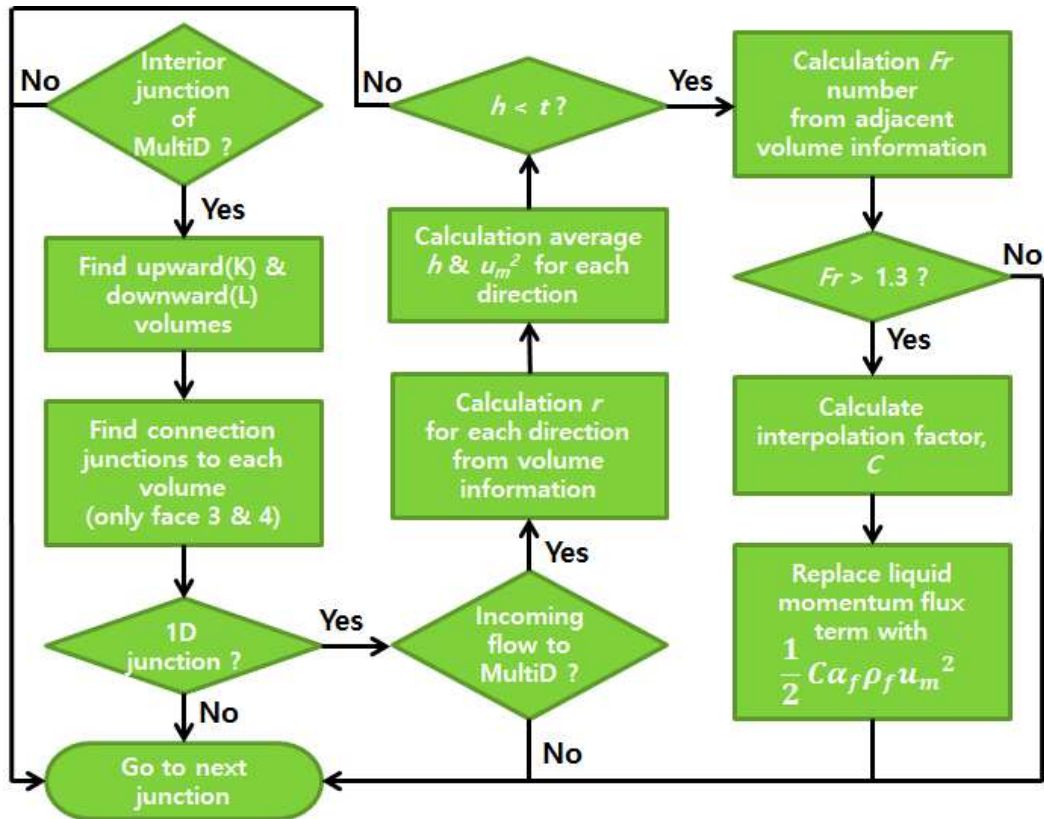


Figure A.2 Calculation process of the momentum flux with the jet impingement model in MARS

## 국문 초록

가압경수로인 APR1400형 원전은 사고 시 원자로용기 강수부에 안전주입수를 직접 주입하는 방식(DVI)을 채택하고 있다. DVI 노즐은 원자로용기 강수부에 직접 연결되어 있기 때문에, 복잡한 열수력적 거동이 강수부 영역 내에서 발생할 것으로 예상된다. 한국원자력연구원은 종합효과실험장치인 ATLAS를 활용하여 APR1400형 원전을 대상으로 한 실험을 수행하였다. 수행된 실험 중 50% DVI관 파단 사고 모의 결과를 국제공동연구인 ISP-50을 위한 실험으로 채택하였으며, 실험에서 관측된 상부 강수부에서 비상노심냉각수의 혼합과 같은 다차원적인 현상들에 대한 계통코드의 예측 능력이 현안으로 제기되었다. 실험 결과에 따르면 저온의 비상노심냉각수는 고온의 강수부 내의 냉각수와 활발하게 혼합되는 것으로 나타났다. 하지만, 이러한 혼합 현상은 계통코드에서 적절하게 예측되지 않았다. 대부분의 계산 결과들은 비상노심냉각수가 주입되는 건전부의 온도를 파단부의 온도보다 상당히 낮게 예측하여 강수부 영역에서 횡방향 온도 성층화 현상을 보였다.

원형인 APR1400과 실험 장치와의 형상비 차이는 강수부에서의 혼합 거동에 영향을 줄 수 있으므로, 본 연구에서는 APR1400형 원전과 유사한 형상비를 갖는 종합효과실험장치인 SNUF를 이용하여 실험을 수행하였다. ATLAS의 경우 길이 대비 직경의 척도비가 6.0인 반면, SNUF의 경우에는 약 2.0으로써, 원형과 상대적으로 유사한 형상비를 보인다. SNUF를 이용한 실험 결과에 따르면, 환형 강수부 내에서 비상노심냉각수의 혼합이 원활하게 이루어지는 것으로 나타났다. 하지만, 최적계통분석코드인 MARS를 활용한

분석 결과에 따르면, 강수부에서의 온도 성층화 현상이 예측되었다. 이는 원형인 APR1400형 원전에 대한 분석 결과에서도 강수부에서 혼합 현상은 적절하게 예측되지 않을 수 있음을 의미한다.

혼합 현상에 대한 계통코드의 예측 능력 한계점에 대한 원인을 다음과 같이 규명하였다. MARS에서는 1차원 체적과 3차원의 MultiD 국소체적이 유로에 의해 연결되어 있는 경우, 비교적 크기가 큰 3차원 영역에서는 해당 유로에 의해 형성되는 축방향 및 횡방향 속도가 작다는 이유로 해당 유로에 의해 전달되는 운동량속 항을 무시한다. 하지만, 간극이 얇은 강수부에 노즐이 연결되어 있고 동 노즐을 통해 수직 방향으로 유체가 유입되는 경우에는, 강수부 내벽에서의 충돌에 의해 무시할 수 없는 축방향 및 횡방향 속도 분포가 형성될 수 있다. 즉, 충돌에 의해 형성되는 유동의 운동량속 항의 고려가 필요하다. 따라서, 계통코드인 MARS에 적용하기 위한 적절한 분출 충돌 모델(Jet Impingement Model)을 개발하였다.

분출 충돌 모델을 개발하기 위해 전산유체역학(CFD) 프로그램을 활용한 계산이 수행되었다. 다양한 조건 하에서의 전산유체역학 계산 결과를 바탕으로 분출 충돌 모델을 수식화하였다. 분출 충돌 현상에 의한 운동량속 항(Momentum Flux Term)은 노즐의 직경, 환형 강수부의 간극 크기 및 유입 유동의 속도를 변수로서 개발되었다. 동 모델은 3차원 국소체적과 연결된 유로의 운동량속 항으로서 MARS 코드에 적용되었다. 분출 충돌 모델이 적용된 수정된 MARS는 SNUF, ATLAS 및 ROCOM 실험 결과를 통해 검증되었으며, 동 검증 결과에 따르면 수정된 MARS는 실험 결과에 대해 상대적으로 높은 예측도를 보였다.

분출 충돌 모델의 발전소 적용성을 평가하기 위해 APR1400형 원전에서의 DVI관 파단 사고 시 강수부에서의 비상노심냉각수 혼합 거동을

MARS를 통해 평가하였으며, 수정된 MARS는 기존 MARS에 비해 강수부에서 상대적으로 활발한 혼합을 예측하였으며, 파단부로 방출되는 붕소의 우회 비율을 높게 평가하였다. 추가적으로 APR1400형 원전에서의 증기관파단사고에 대한 분석을 MARS 코드를 활용하여 수행하였다. 증기관파단사고 시 분출 충돌 모델에 따른 혼합 효과를 평가하기 위해 감속재온도계수에 의한 양의 반응도를 노심에서의 국부적인 유체 온도를 바탕으로 평가하였다. 동 분석 결과에 따르면, 기존 MARS와 수정된 MARS에 의한 반응도 차이는 약  $0.2 \sim 0.4\% \Delta \rho$ 로 평가되었다. APR1400형 원전의 경우 증기관파단사고 시 약  $0.2\% \Delta \rho$ 의 안전 여유도가 갖는다는 점을 고려할 때, 분출 충돌 모델을 적용한 MARS는 안전 해석 결과에 의미 있는 영향을 주는 것으로 판단할 수 있다.

#### 주요어

다차원 혼합, 환형 강부수, 분출 충돌 모델, MultiD, 원자로용기 직접주입관 파단, 증기관파단, SNUF, ATLAS, ROCOM, MARS, 운동량속 항

학번: 2010-30259